

Micro-bioreactor Design for Chinese Hamster Ovary Cells

ARCHIVES

by

Shireen Goh

B.S. Applied & Engineering Physics, Cornell University (2005)

Submitted to the Department of Materials Science and Engineering
in partial fulfillment of the requirements for the degree of
Doctor of Philosophy in Materials Science and Engineering

at the

MASSACHUSETTS INSTITUTE OF TECHNOLOGY

June 2013

© Massachusetts Institute of Technology 2013. All rights reserved.

Author
Department of Materials Science and Engineering
23rd May 2013

Certified by
Rajeev J. Ram
Professor of Electrical Engineering and Computer Science
Thesis Supervisor

Accepted by
Gerbrand Ceder
Chair, Departmental Committee on Graduate Students

Micro-bioreactor Design for Chinese Hamster Ovary Cells

by

Shireen Goh

Submitted to the Department of Materials Science and Engineering
on 23rd May 2013, in partial fulfillment of the
requirements for the degree of
Doctor of Philosophy in Materials Science and Engineering

Abstract

The research objective is to design a micro-bioreactor for the culture of Chinese Hamster Ovary (CHO) cells. There is an increasing demand for upstream development in high-throughput micro-bioreactors specifically for the recombinant CHO cell line, an important cell line for producing recombinant protein therapeutics. In order to translate a micro-bioreactor originally designed by our group for bacteria to CHO cells, there would need to be significant modifications in the design of the micro-bioreactor due to the extreme sensitivity of CHO cells to physical and chemical stresses. Shear stresses inside the growth chamber will have to be reduced by three orders of magnitude. Moreover, the long doubling time of CHO cells requires a 2 weeks long culture. In a high surface to volume ratio micro-bioreactor, evaporation becomes a major problem. Contamination control is also vital for CHO cultures. In addition, the offline sampling volume required for validation necessitates a doubling of the working volume to 2mL. The newly designed Resistive Evaporation Compensated Actuated (RECA) micro-bioreactor is fully characterized in this thesis to ensure that the design meets the physical specifications of the required CHO cell culture conditions. The RECA micro-bioreactor will be tested with industrial recombinant CHO cell lines. This work is done in collaboration with Genzyme, USA and Sanofi-Aventis, Frankfurt. In this thesis, we also propose the use of dielectric spectroscopy electrodes for online cell viability sensing of CHO cells in micro-bioreactors. The electrodes are fabricated on polycarbonate, a biocompatible and optically clear thermoplastic that will be one of the future base material for microfluidic devices which can be rapidly prototyped. To demonstrate the viability of dielectric spectroscopy as an online viability sensor for CHO cells in a micro-bioreactor, the electrodes are used to characterize samples taken daily from a CHO shake flask batch culture without any sample modifications. Two different electrode geometries and correction methods will be compared to find the optimal system for viability measurements in a micro-bioreactor.

Thesis Supervisor: Rajeev J. Ram

Title: Professor of Electrical Engineering and Computer Science

Acknowledgments

This PhD is obtained through curiosity, tenacity, a good sense of humor, and more importantly, the support of others through wise guidance, idea-provoking conversations, common thirst for knowledge and fun camaraderie. First, I would like to thank my supervisor, Prof. Rajeev Ram, who has always challenged me to follow an idea to completion, think unconventionally and counter check all my claims. My collaborators at Sanofi, Germany, namely Michelangelo Canzoneri, who's dedication and belief in this project have brought the best out of this industrial collaboration with MIT. The mutual sharing of information and constructive decisions made throughout this project gave rise to a project that can potentially transform an early phase experimental platform in the upstream process development for biopharmaceutical companies. Along with Michelangelo is Horst Blum, Vicki Lade and the rest of the upstream process development team in Sanofi at Frankfurt, Germany, who have made my visit to the Frankfurt site very educational and enjoyable. To my committee members, Prof. Darrell Irvine, Prof. Michael Rubner and Prof. Anthony Sinskey, their valuable advices and kind dispositions have been very encouraging during our committee meetings.

This research project is built upon the previous work of others in the group, particularly, Kevin Lee, Paolo Boccazz and Harry Lee. Kevin, who has a positive attitude to everything and is ever willing to train and help out, has been instrumental in my progress in the initial stages of this project. Paolo, who has patiently taught me biological experimental skills, smoothly converting engineering suggestions to methods that are more biologically acceptable. And Harry, who's ability to build anything has always amazed me and who's contraptions are still being used in the lab to facilitate this project. Jason Orcutt, who has always been very helpful with suggestions, Reja Amatya, who is very kind and always making sure that I am doing fine in the lab, Katey Lo, who is always very accommodating when we had to split time on the microscope, Joe Summers, who was always organizing the lab parties together with Harry, Evelyn Kapusta, who has been a great office mate and friend, Parthiban

Santhanam, who always promptly help out with program licensing issues that I am facing and for the random fun discussions we had being neighbors, William Loh, who helped me out even at his own discomfort when I accidentally made a deep cut on my finger, Karan Mehta, who is a caring friend and a great violinist, Charles Meng, who always have a smile on his face and a great person to share officer experiences with, Prof. Tianxin Yang, who is a great travelling companion during our group trip and very motherly to me, Prof. Maria Del Carmen Varquez Garcia, who is such a great mentor, ever willing to give me advice and suggestions that have been very helpful in my moments of need, Johanna Chong, whom I got to know over the group trip who is a strong person that I know will go far and Gajendra Singh, who has always been a good friend and always kindly offering to help me out with the cell culture whenever I need help.

I would also like to thank all my friends and families for keeping me sane throughout my PhD. To my dear friends at MIT, all the fun, laughter, delicious food and caring support have made this experience more enjoyable. Thanks for bringing me out of my work and reminding me to smell the flowers and in return, being there to smell the flowers with me whenever I don't want to think about work. To my precious friends back home, thanks for showing your care for me in very many different ways and for keeping me up to date with your lives even when I am halfway around the world. Thanks for always being there for me and always willing to meet up with me no matter how busy you are during my short visits back home. To my wonderful family, thanks for all your support and always believing in me. I am very grateful for all the love and pampering whenever I go home for a visit. I would like to especially thank my parents, Goh Ing Bing and Choo Gaik Hioh, who have patiently given me detailed answers and explanations to all my "Why, how and what" questions growing up, who broadened my horizon by constantly reminding me to look beyond my immediate vicinity to aim for a larger goal.

Last but not least, I would like to dedicate this thesis to my husband, Henry Koh, the one who understands me the most and is always by my side during my best and worst moments.

Contents

1	Introduction	25
1.1	Biopharmaceutical Development	26
1.2	Motivation for Micro-bioreactors	28
1.3	Physiology of CHO	29
1.4	Design Specifications	32
1.4.1	Micro-bioreactors	32
1.4.2	Viability Measurements in Micro-bioreactors	37
1.5	Review of State-of-the-Art	38
1.5.1	Micro-bioreactors	38
1.5.2	Viability Sensors	41
1.6	Predecessor Micro-bioreactors	42
1.6.1	PIBA Micro-bioreactor	42
1.6.2	Chemostat Micro-bioreactor	48
1.7	Thesis Outline	52
2	Micro-bioreactor Design	55
2.1	Introduction	55
2.2	Micro-bioreactor Modifications	56
2.2.1	Low Aeration Rate	56
2.2.2	Variable Culture Volume	61
2.2.3	Sterile Accurate Sampling	63
2.2.4	Shear Sensitive Cells	65
2.3	Micro-bioreactor Design	73

2.3.1	RECA Micro-bioreactor	73
2.3.2	RECA Manifold	76
2.3.3	RECA Infrastructure	77
2.4	Fabrication of Micro-bioreactor	81
2.5	Conclusions	85
3	Testing and Validation of Micro-bioreactor	87
3.1	Introduction	87
3.2	Resistance Line Characterization	88
3.2.1	Deflection Time	90
3.2.2	Mixing Time	95
3.3	Carbon Dioxide Sensor Calibration	96
3.3.1	Carbon Dioxide Sensor	96
3.3.2	Optimal Modulation Frequency	100
3.3.3	Bicarbonate Calibration	102
3.4	Gas Transfer Rate (k_{La})	102
3.4.1	Theoretical Estimates	104
3.4.2	Oxygen	106
3.4.3	Carbon Dioxide	108
3.5	Optical Density	110
3.6	Evaporation Rate	115
3.7	Conclusions	116
4	Dielectric Spectroscopy	119
4.1	Introduction	119
4.2	Theory of Dielectric Spectroscopy	120
4.3	Electrode Polarization	122
4.4	Physical Methods	125
4.4.1	Conductivity Reduction	125
4.4.2	Electrode Material Selection	126
4.4.3	Rough Electrodes	127

4.5	Analytical Methods	127
4.5.1	Subtraction Method	128
4.5.2	Constant Phase Element (CPE) Correction	128
4.6	Design of Electrodes	130
4.6.1	Interdigitated Electrodes Structure (IDES)	131
4.6.2	Four Electrodes Structure (4ES)	133
4.6.3	Comparison between IDES and 4ES	135
4.7	Large IDES Electrode Experiments	137
4.7.1	Calibration	138
4.7.2	Shake Flask Validation	146
4.7.3	Subtraction Method	146
4.7.4	Results	147
4.8	Small IDES Electrode Experiments	150
4.8.1	Calibration	152
4.8.2	Data Analysis	155
4.8.3	Results	157
4.9	Fabrication of Platinum Electrodes on Polycarbonate	164
4.10	Conclusions	169
5	Conclusions and Future Work	171
A	Shear FDTD Matlab Code	177
B	The Debye Equations	183
C	CHO Shake Flask Culture Protocols	187
C.1	Seed Train Protocol for Invitrogen CHO-S Freestyle Cells	187
C.2	Growth Profiles of CHO Shake Flask Cultures	194

List of Figures

2-1	Evaporation rate of Chemostat for different humidification configurations. Water Ring refers to a water channel around the chip as shown by the purple line in the chemostat image. 45C Local is a local humidifier at temperature 45°C placed between the gas manifold and the chip. 80C remote refers to a remote humidifier at temperature 80°C placed at the gas input before the gas manifold, 80C+45C is the combination of both the local and remote humidifiers, 80C+45C+Ring is a combination of both humidifiers and the water ring, 80C+45C+Ring (No Solenoid) is the combination of all above but with the solenoid removed to observe the effects of condensation on the cold metal part of the solenoid. Experiment performed by Kevin Lee on his chemostat for <i>E. Coli</i> growth.	57
2-2	Schematic showing the previous humidifier strategy for the PIBA micro-bioreactor and the new humidifier strategy for RECA micro-bioreactor.	60
2-3	Table with expected day to day working volumes of the RECA micro-bioreactor for batch culture, fed-batch culture and fed-batch culture with oversampling to prevent over-filling of the growth chamber. The sampling protocol is the one defined by Sanofi-Aventis, Germany. The fed-batch protocol is assumed to be a feed of 10% increase by volume for days 1,3,5,7 and 9.	62
2-4	If volume exceeds 2mL, there will be incomplete mixing and a dead zone will develop. The solution is to oversample for fed-batch cultures to ensure that volume is always less than 2mL	62
2-5	Schematic showing the sampling ports (A and B) of the PIBA micro-bioreactor with the unmixed volume of each sampling port.	63
2-6	Schematic showing the sampling process of the RECA micro-bioreactor with ejecting of sample using air and cleaning of the 10µL sample reservoir with sterile water and then air drying it.	64
2-7	Schematic showing the effects on productivity of recombinant CHO cells due to different shear rates.[33]	66

2-8 (a)The region of maximum shear in our mixer design for our micro-bioreactor for CHO cells, highlighted in a dashed rectangular outline, and (b) the Poiseuille flow profile in a channel with the shear stress on the cells given by the slope of the velocity profile multiplied by the dynamic viscosity.	67
2-9 Schematic showing the parameters used in the modeling of the shear stress along the channel in between the mixers.	68
2-10 Schematic showing the air resistance lines used and their dimensions. There are 6 resistance lines, 2 for each mixer (input and output).	71
2-11 FDTD Modeling of the maximum shear stress inside the channel between the mixers for resistance line 1 and resistance line 2.	72
2-12 Top view of the RECA micro-bioreactor showing the positions of the input lines, feed reservoirs, peristaltic pumps, growth chamber, sensors and sampling port	74
2-13 Top view of the RECA micro-bioreactor showing gas connections to the gas manifold	75
2-14 Top view of the RECA gas manifold showing gas routings for the valves, mixer, and gas mixing. The manifold consist of 3 layers, the top layer with the solenoid valves and holes drilled directly to the second layer which has the green routes, connecting the output of the valves to the gas connectors in the middle of the manifold, and the bottom layer which connects all the gas lines to the inputs of the solenoid valves, with blue routes.	78
2-15 Table showing the RECA gas manifold connections for the valves according to the valve number. The valve numbers are shown in Figure 2-14. NO stands for Normally Open and NC stands for Normally Closed in the table. The selection of what is NO or NC is based on energy considerations.	79
2-16 A photograph of the RECA setup with the control boards, gas lines, humidifier and micro-bioreactor	80

- 2-17 This is a photograph showing the spin coater to spin thin ($70\mu\text{m}$) PDMS membranes. The thickness of the PDMS membrane is monitored using an interferometer which measures the distance (time traveled) between peaks from the reflections of light off the interfaces. 82
- 2-18 Illustration of the bonding process between PDMS and Polycarbonate. An amine functional silane is used as the bonding molecule, forming a glass-like bond (Si-O-Si) with between PDMS and the silane end of the molecule and a hydrogen bond between the carboxyl groups in polycarbonate and the amine group of the molecule. Since the silane end of the molecule has 3 reactive groups attached to it, a cross-linked silane network is formed. This crosslinked network forms a barrier to prevent hydrolytic cleavate by water molecules. 83
- 2-19 An illustration of the fabrication process for the RECA Micro-bioreactor. The details of the fabrication are described in the paragraphs of this section. 84
- 3-1 Sequence of image showing a complete deflection of the membrane in a single chamber for Resistance Line 2, with the time stated at the bottom of the figure. The yellow box shows the region of pixels in which the image analysis is performed to determine the time taken for the complete deflection of the membrane. The results are shown in Figure 3-2 91
- 3-2 Graph showing the intensities of the Red, Green and Blue color as detected by an Opteon CCD camera. The intensity value is a mean value of intensities calculated over a square pixel as depicted in the series of images in 3-1. 92
- 3-3 Mixing time characterization for Resistance Line 1 for different cycle times. Resistance Line 1 have a total deflection time of 7.5 seconds. 93

3-4 Sequence of image showing the mixing of green dye injected in from one of the reservoirs into the mixing chamber. This is the sequence of images for the mixing time measurement with Resistance Line 1 for a cycle time of 12 seconds. The time constant of the mixing time is measured to be 8.5 seconds, measured in Figure 3-3.	94
3-5 Theoretical plot of the estimated optimal modulation frequency . . .	99
3-6 Experimentally measured phase difference between 1M NaHCO ₃ and 1mM NaHCO ₃ solutions for a range of modulation frequency. The data is fitted to Equation 3.4 and the lifetime of the two dyes are obtained through the fit, with the reference dye having a lifetime of 2.5 μ s and the indicator dye having a lifetime of 312 ns.	101
3-7 The calibration of the CO ₂ sensor with Bicarbonate(NaHCO ₃) solution of varying concentration. The dissolved CO ₂ gas is calculated after measuring the pH immediately after mixing. The resultant dissolved CO ₂ concentration is shown in Table 3.3. The data is fitted to Equation 3.9	103
3-8 A model for the gas transfer of bench top bioreactors is shown in (a). The image shows the diffusion of gas from sparged bubbles into the bulk of the liquid through a liquid film of thickness δ . For the RECA aeration system shown in (b), the gas chamber is separated from the bulk liquid by a thin PDMS membrane, before reaching the oxygen sensor at the bottom of the chamber. There are two phenomena that dictates the kLa of gas in this geometry. One is the diffusion of gas through the 70 μ m PDMS membrane. The other is the diffusion of gas in the liquid coupled with the mixing mechanism. The resultant k _{La} will be a parallel combination of both phenomena.	104

3-12 (a) The Optical Density (OD) sensor is a turbidity probe which measures total cell density in the culture due to the scattering of light by the cells. The incident light is collimated and the transmitted light intensity is measured using a small detector to limit the angle of incidence and detection so that only unscattered light is transmitted to the detector. (b) The OD sensor using LED as light source, with a diffuser to make the intensity more uniform and a collimator. The detector consists of a solid angle reducer coupled to a fiber that ends at a photodetector. The OD sensor has the same design as the OD sensor in Kevin Lee's thesis.[40] 110

3-13 Study of scattering cross section as a function of wavelength for polystyrene microspheres suspended in water. The scattering cross section for mammalian cell lines having a larger cell diameter is 2 times cross section area of the cells while for bacteria cells, the scattering cross section is only half the cross section area of cells for visible wavelengths, which is typically used in OD measurements. Therefore, the OD measurements are expected to saturate at a much lower cell density for mammalian cells as compared to bacteria cells.[28] 112

3-14 From the OD measurements in the spectrophotometer shown in (a), a linear relationship between the measured absorbance and cell density is obtained for low cell densities. At high cell densities ($> 8 \times 10^6$ cells/mL), the absorbance measured is non-linear. This is due to the shadowing effect of cells at high densities for the spectrophotometer with a path length of 1 cm. Since the RECA Micro-bioreactor has a flat form factor, the path length of the OD sensor is 5 times shorter than that of the spectrophotometer. Hence, the OD sensor in the RECA is able to achieve linearity at least up to a cell density of 22.2×10^6 cells/mL, potentially even at higher cell densities. Results shown in (b).114

3-15 The evaporation rate of the RECA Micro-bioreactor with Resistance Line 1 is measured by performing an optical density (OD) measurement on food dye injected into the growth chamber of the micro-bioreactor. The increase in absorbance over time is related to the increase in dye concentration as the volume decreases. The experiment was performed overnight (7-8 hours). The measured evaporation rate is $4.7\mu L/hr$ with a local 45°C humidifier attached.	116
4-1 Capacitance of the cell suspension versus frequency in the log scale. The difference between low frequency and high frequency capacitance around the β -dispersion gives the change in capacitance due to the presence of viable cells in the suspension.	121
4-2 Physical and equivalent circuit model for the Electrical Double Layer (EDL) parasitics.	123
4-3 Effects of electrode polarization on the dielectric spectra. Figure (a) shows the theoretical prediction of the dielectric spectra for CHO cells of densities 2×10^6 cells/mL and 1×10^7 cells/mL. With the effects of electrode polarization added to the spectra, the resultant graph results in a rapidly increasing capacitance at low frequencies as shown in (b). The dispersion due to the cells is completely buried in the electrode polarization parasitics.	124
4-4 The effects of the media conductivity on electrode polarization. This is an experiment performed by measuring KCl solutions of increasing concentration. As conductivity increases the time it takes to form the EDL decreases and hence the electrode polarization shifts to higher frequencies for high conductivity media.	126
4-5 Schematic showing dimensions for the analytical model for the cell constant of the Interdigitated Electrode. For the electrodes drawn in this figure, $N = 9$. D refers to the driving electrode and S refers to the sensing electrode.	132

4-6 An ideal equivalent circuit of the four electrode configuration (H_C, H_P, L_P, L_C) showing sample impedance, Z_S split into 3 sections (Z_L, Z_M, Z_R) and the electrode polarization impedance, Z_P . Division of the voltage between the inner electrodes, H_P and L_P , with the current gives Z_M which does not include any polarization impedance, and hence the four electrode measurement, ideally, can be AC electrode polarization free.	134
4-7 This figure shows how the four terminals of the LCR meter cannot be directly used to perform four electrode measurements for dielectric spectroscopy	136
4-8 Printed Circuit Board (PCB) with identical gold interdigitated electrodes used for testing the electrode geometry	137
4-9 Calibration of electrode cell constant with 10mM, 20mM, 50mM and 100mM KCl solutions	139
4-10 General model for the residuals of the interdigitated electrodes	140
4-11 Log-log plot of dielectric spectra before and after electrode residuals correction	143
4-12 Calibration of DS electrodes with CHO Cell Density	145
4-13 Plot of polarization capacitance of the CHO medium corrected for background capacitance and averaged between a 400kHz bandwidth around 1MHz, $\Delta C_{<1M>}^{pol}$, with respect to the resistance, R_S , of the medium. This plot consists of all the measurement of the supernatant from the 9 day shake flask culture (\blacktriangle), the supernatant from the 4 dilution samples from the CHO calibration measurement (\blacksquare) and also a data point which correspond to the 100mM KCl solution sample (\bullet). The fitting curve (-) is obtained from fitting a 3 rd order polynomial to the data set. From the graph, there seems to be a clear relationship between the resistance measured and the polarization capacitance of an aqueous medium, either a 100mM KCl solution or CHO medium of slightly varying conductivities	148

4-14 (a) Live, dead and total CHO cell densities counted under the microscope, (b) The results of the dielectric spectroscopy measurements compared with offline live cell counting, and (c) optical density measurements compared with offline total cell counting for the daily samples taken from the shake flask CHO batch cultures	149
4-15 Photograph of Gold interdigitated DS electrodes on printed circuit board (PCB) with a polycarbonate measurement chamber, machined in the lab. A supporting PCB board is designed to convert the 4 point measurement of the LCR meter to the 2 point measurement required by the interdigitated electrodes with a holder for the Glass Vial.	151
4-16 Calibration of electrode cell constant with 1mM, 10mM and 100mM KCl solutions	153
4-17 Log-log plot of dielectric spectra before and after electrode residuals correction	154
4-18 Equivalent Circuit and Nyquist Plot for the CPE Model in series with the parallel RC model of an aqueous solution. The parallel RC circuit is represented by a semicircle in the Nyquist plot approaching zero as $\omega \rightarrow \infty$. The Constant Phase Element (CPE) model is represented by a line with a slope at an angle $\theta = (\pi/2)\alpha$ that goes to infinity as $\omega \rightarrow 0$	156
4-19 Fresh CD CHO medium without cells were measured every 5 minutes (a) with unconditioned electrodes and (b) with pre-conditioned (soaked in DI water for 24 hours prior to measurement) electrodes. The large variation in spectra for the unconditioned electrodes shows that the electrodes need to be hydrated overnight before performing any Dielectric Spectroscopy measurements to ensure the formation of a stable EDL.	158
4-20 The graph shows the time it for the temperature, pH and conductivity to stabilize after removing the sample from the CO ₂ incubator for dielectric spectroscopy measurements. Measurements performed in a beaker.	159

4-21 After inserting the measurement sample into the Dielectric Spectroscopy measurement chamber, the sample takes \sim 30 minutes to equilibrate. 160

4-22 The CPE correction performed on (a)fresh CHO Medium without cells and (b)a CHO cell culture suspension. The water line is a line marking the dielectric constant of water.(a) For the fresh CHO medium, after CPE correction the spectra should fall on the water line since the permittivity of CHO medium should just be the permittivity of water. The spectra flattens out and falls on the water line as predicted. However, the CPE model only holds for a particular frequency range and hence at very low frequencies, the permittivity drops below the water line. (b) After CPE correction, the dispersion of the live cells are revealed and shown in the figure on the right. A Cole-Cole model is then fitted to the dispersion curve to obtain the $\Delta\epsilon$ that is linearly related to the viable cell density in the culture. 162

4-23 Dielectric Spectroscopy validation with live cell density. The author's results are shown in blue squares (\square). An R^2 value of 0.9524 is obtained for the fit. Values from literature, dielectric spectroscopy measured on CHO cells using large commercial Aber Probes is shown as red triangles (\triangle).The results match quantitatively to literature values. 163

4-24 Step by step description of the process of patterning platinum interdigitated electrodes on a polycarbonate substrate via shadow masking in a sputtering machine. 165

4-25 Actual picture of platinum interdigitated electrodes (Large IDES) sputtered on polycarbonate substrate. Polycarbonate substrate remains flat after deposition 166

4-26 Photograph of the stencils that is used as a mask for sputtering Platinum electrodes (Small IDES). (A) The final sputtered electrode, (B) Polycarbonate (PC) stencil + thin metal stencil (0.002 in = 0.051 mm thick) for the horizontal lines, (C) Polycarbonate (PC) stencil + thin metal stencil (0.002 in = 0.051 mm thick) for the vertical lines, (D) Thick metal stencil (0.015 in = 0.381 mm thick) for the horizontal lines (used with PC stencils to clamp the stencil onto the substrate) and (E) Thick metal stencil (0.015 in = 0.381 mm thick) for the vertical lines (used with PC stencils to clamp the stencil onto the substrate)	167
4-27 Actual picture of platinum interdigitated electrodes (Small IDES) sputtered on polycarbonate substrate. Polycarbonate substrate remains flat after deposition	168
C-1 Growth curve for the (a) Invitrogen and (b) Sanofi CHO cell lines. The Sanofi cell line has a longer stationary phase than the Invitrogen cell line because it has been optimized for production.	194

List of Tables

1.1	Criteria for Micro-bioreactor Based Upon Parameter Achieved for Current Industrial Processes	30
1.2	Offline Sampling Volume Requirements	35
1.3	Downstream Processing Sampling Volume Requirements	36
1.4	Comparison of the capabilities and performance of state-of-the-art micro-bioreactors for CHO cells with bench top bioreactors	39
1.5	Growth and Death Rate of CHO Cells for experiments with our micro-bioreactor (PIBA) compared with shake flasks and well plates for 3-5 day cultures	45
3.1	Summary of parameters and validation methods for the RECA Micro-bioreactor	89
3.2	Results from the characterization of the different Air Resistance Lines	95
3.3	Calculated dissolved carbon dioxide concentrations from NaHCO_3 solutions at 25°C from measured pH values and known concentration of NaHCO_3	100
3.4	Physical Parameters used in the calculation of the gas transfer rates, $k_{L\alpha}$, for oxygen and CO_2	106
3.5	Summary of Specifications of the RECA Micro-bioreactor and comparison with Industrial Bioreactors	117
4.1	CPE correction performed in literature for different types of electrodes and media conductivity	129

4.2 Geometrical description of the Interdigitated Electrodes(IDES) and the corresponding calculated cell constant	132
4.3 Resistance between Platinum electrodes (Small IDES) sputtered on Platinum for using stencils of different thickness	167

Chapter 1

Introduction

For the last decade, many different types of micro-bioreactors have been developed for microbial fermentations with fair success.[66] However, the implementation of micro-bioreactors for Chinese Hamster Ovary (CHO) cells have lagged behind microbials due to the fact that CHO cell cultures are more complex as compared to bacteria cell cultures, despite being a very important cell line for biopharmaceutical manufacturing. The success of micro-bioreactors for microbial cell cultures has spurred recent interests in developing micro-bioreactors for CHO cells, the main production cell line of biopharmaceutical companies. As described in Section 1.1, there exists a need for biopharmaceutical companies to reduce costs of production and time to market of new biotherapies in order to be competitive. Section 1.2 examines the role of micro-bioreactors in helping biopharmaceutical companies revolutionize their upstream development capabilities resulting in a better Quality by Design (QbD) approach. In order to design a micro-bioreactor for CHO, the CHO cell physiology and how it differs from microbial cultures and subsequently, how these differences will affect the design of the micro-bioreactor must be understood.(Section 1.3) Besides the design modifications necessary for accommodating the different CHO cell physiology, the micro-bioreactor must also mimic the process conditions in an industrial bioreactor in order for the micro-bioreactor to serve as an accurate scale down model of large scale bioreactors. The physical restrictions on the scaling and size requirements for the micro-bioreactor needed to emulate large scale bioreactors, the

minimum working volume needed for offline samplings to meet the analytical requirements, and the requirements of an online viability sensor are described in Section 1.4. Finally, Section 1.5 describes the state-of-the-art micro-bioreactors designed for CHO cells and compares them with our proposed micro-bioreactor for CHO cells. The state-of-the-art viability sensor for micro-scale devices are also explored in the same section.

1.1 Biopharmaceutical Development

The use of biologics, like monoclonal antibodies, recombinant proteins and nucleic acid based proteins, in pharmaceuticals have been well received in the last decade. Therapeutic monoclonal antibodies have revolutionized various oncology treatments because they have less side effects than traditional cytotoxic drugs.[62, 63, 64] In 2007, there are 22 therapeutic monoclonal antibodies in the market with a value of over \$17 Billion and the market expected to increase to around \$49 Billion globally by 2013.[32] Some of the well known licensed monoclonal antibody treatments are Rituxan for cancer, Remicade for arthritis, Synagis for lung disease, and Herceptin for breast cancer.[8, 61]. Currently, more than 50% of the pharmaceutical industry's pipeline portfolio consist of recombinant proteins and monoclonal antibodies and over 600 new biologics are being developed every year. Therapeutic recombinant proteins and monoclonal antibodies are produced by recombinant mammalian cells, genetically modified to overproduce the therapeutic protein. Mammalian cell lines are preferred because they contain organelles and enzymes that can synthesize, fold and chemically modify the protein to form tertiary structure, like glycosylation, which is essential for the therapeutic function of the protein. The latter process is known as post-translational modification. In some cases, where post-translational modifications of the proteins are not required, some recombinant proteins, like Insulin, can be produced in the more robust and faster growing cells like *Escherichia Coli*. However, most therapeutic proteins in production currently require post-translational glycosylation which can only be found in eukaryotic cells, of which 70% are produced

using the Chinese Hamster Ovary (CHO) cell line.

In spite the rapidly growing biologics market, biopharmaceutical companies are constantly faced with pressures to reduce costs from health care providers. Moreover, the long time from discovery to market of biopharmaceuticals frequently results in early patent expiration and profit losses. Competition from generics also drives biopharmaceutical companies toward finding avenues to lower development and manufacturing costs. There also exists an urgency for pharmaceutical companies to develop a large portfolio of new drugs in order to stay ahead of rival biopharmaceutical companies.[32, 13] Typically, a new drug will take around 6-9 years to go through development, manufacturing, clinical trials and FDA approval before becoming available on the market.[16] There are many benefits of shortening the time to market including longer validity of the patent when the drug is released to the market, the ability to test and develop more biologics simultaneously to increase the chances of finding a blockbuster drug and lowering the overall cost of the drug. The upstream development process for producing recombinant proteins is currently very complex and time-consuming. For the drug protein to be FDA approved, there must be consistency in the quality of the recombinant drugs produced, in particular, the glycosylation and effectiveness of therapeutic proteins must retain the same quality even for different culture batches. Since the quality of the glycosylation of the recombinant protein can be influenced by process conditions, the control and monitoring of process parameters in a bioreactor becomes very important.[69] Moreover, since therapeutic monoclonal antibodies are used at high doses over a long period of time, in order to meet market demands, the cell culture must be able to produce a high product titer while maintaining the same product quality.[42] All these requirements must be maintained during scale up and scale down of the production batches. It is important to start right and therefore, an important cost cutting strategy would require making the upstream process development more accurate and efficient.

1.2 Motivation for Micro-bioreactors

The upstream development of bioprocesses for the production of recombinant proteins consists of the following four stages: 1. Clone Selection, 2. Clone Stability Tests, 3. Process Development and 4. Scale Up Experiments. First, 1000 clones are grown in stationary 96 well plates to find the fastest grower and highest producer clones based on Enzyme-linked Immunosorbent Assay (ELISA) results. The selected clones, typically around 50-100 clones, are then grown in shake flasks, which is an agitated environment similar to bioreactors but without any pH, temperature, dissolved oxygen (DO) or feed rate control. Stability tests to ensure that the clones will not mutate over many generations will also be performed during this stage. From the shake flask experiments, only 4-6 clones are selected and transferred to bench scale experiments before scaling up to large scale industrial bioreactors. There is a cost-limiting factor determining the number of clones selected at this stage because bench top bioreactors and scale up experiments are very costly to run. This selection process is risky because there is evidence that clone selection from measuring growth and productivity alone as a single end point in 96 well places is not a predictor for selecting a stable cell line.[3] Moreover, shake flasks with no instrumentation or control over pH, DO or feed may not be able to select the the most productive clone with a stable glycosylation profile since the product titer and quality can be affected by the actual process conditions. [69] Therefore, a crucial technology missing in conventional upstream development protocol is a miniaturized high throughput and instrumented secondary clone selection system with online sensors that is an almost exact scale down model of an industrial bioreactor with sufficient volume for offline characterization of product titer, glycosylation profules and other important process conditions.

In the near future, biopharmaceutical companies will be looking into building cellular function models that will help elucidate the effects of feed rate, physical and chemical stresses on the cells' metabolic state. Having predictive models of the impacts of manufacturing conditions on industrially relevant cell lines would greatly accelerate the upstream process optimization by adopting a Quality by Design(QbD)

approach.[59] Often times, the overexpression of the recombinant proteins is rate limited by an enzyme whose kinetics are not well understood. Understanding the rate limiting steps affecting the productivity of cells will greatly reduce the experiments needed to find the optimal processing conditions for the recombinant cell line. The large data banks required to form a complete cellular function model require a high throughput platform that can run at a much lower operating cost than bench scale bioreactors but with the same set of instrumentations. This miniaturized biotechnology platform would have to be automated and run at least 20 experiments in parallel in order to complete the experiments in a reasonable time frame.

1.3 Physiology of CHO

The Chinese Hamster Ovary (CHO) cell line is an important cell line for producing recombinant protein therapeutics, accounting for almost 70% of the biotherapy market, far exceeding other commonly used mammalian cell lines such as 3T3, BTK, HeLa and HepG2. In 2006, the worldwide sales of biopharmaceutical products produced using the CHO cell line alone exceeds US\$30 billion.[?] With the burgeoning interests in expanding the range of biologics produced from CHO cells, there is an increasing demand for upstream development in high-throughput micro-bioreactors, such as microfluidic devices and well plates, specifically for recombinant CHO cell research and biotechnological process optimization. In recent years, micro-bioreactors in the form of microfluidic devices and well plates have emerged for upstream development of microbial cell lines.[66] The development of micro-bioreactors for mammalian cell lines like CHO cells have not gained as much momentum mainly because of the added complexity when trying to adapt these microbial micro-bioreactors for the more sensitive mammalian cell lines. The design criteria for micro-bioreactors designed for mammalian cell lines are listed with yeasts and *E. Coli*, a bacterial cell line in Table 1.1.[2]

Unlike bacteria or yeast cells, the growth and productivity of Chinese Hamster

*wet cell weight

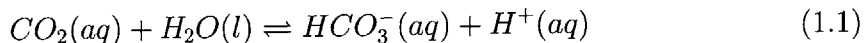
Table 1.1: Criteria for Micro-bioreactor Based Upon Parameter Achieved for Current Industrial Processes

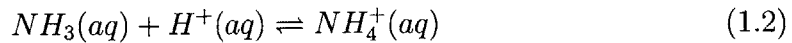
Parameters	Mammalian Cells	Yeast	<i>E. Coli</i>
Growth rate	0.041-0.075 h ⁻¹	0.5-4 h ⁻¹	0.1-4 h ⁻¹
Doubling time	15-24 h	0.5-5 h	0.1-4 h
Cell Density	10 ⁶ -10 ⁷ cells/mL	200-500 g/L wcw*	200-500 g/L wcw*
OUR	<5 mmol/Lh	<300 mmol/Lh	<300 mmol/Lh
k _L a	1-15 h ⁻¹	200-400 h ⁻¹	200-400 h ⁻¹
DO	>20%	>20%	>20%
Agitation	50-150 rpm	100-3000 rpm	100-3000 rpm
Dissolved CO ₂	35-80 mmHg	<5%	<5%
Temperature	32-38 °C	18-30 °C	18-37 °C
pH	6.8-7.15	4-8	6-7.5
pH Control	Caustic or CO ₂ addition	Acid or caustic addition	
Cycle time	20 days	<7 days	<4 days

Ovary (CHO) cells are very sensitive to process conditions. CHO cells, like most mammalian cells, can easily undergo necrotic or apoptotic cell death under physical and chemical stresses. To give a sense of their sensitivity to shear stress, a CHO cell's shear stress tolerance is 3 orders of magnitude lower than that of an *Escherichia coli* (*E. Coli*) cell, a common type of bacteria used in biotechnology. Shear stress above 0.005 Nm⁻² have been shown to affect protein glycosylation in CHO cells due to morphological deformation of the endoplasmic reticulum, the organelle responsible for folding and glycosylation of the protein.[33] Therefore, the micro-bioreactor must be designed to have a mixer that generates low shear stress and yet provide a fast enough mixing to prevent large gradients which may cause nutrient starvation or toxicity. Moreover, the long doubling time of CHO cells(22-24 hours) require a much longer culture time for CHO cells, typically 2-3 weeks long, as compared to *E. Coli* cultures which lasts only up to 4 days due to their much shorter doubling time(1 hour). For long term cultures, evaporation becomes a major problem because of the high surface to volume ratio of small working volumes of micro-bioreactors. Water loss can also cause the osmolarity of the culture medium to increase to toxic levels within 5 days. Evaporation compensation strategies will need to be employed for micro-bioreactors running long term cultures like CHO cell cultures. The longer doubling time of CHO cells also makes the culture more easily contaminated since the cells can

be easily overtaken by faster growing yeast and bacteria cells. The micro-bioreactor must therefore be able to maintain sterility throughout the 10-14 days of culture duration and all process including sample removal and incubation must be performed without compromising the sterility of the growth chamber.

Since Chinese Hamster Ovary (CHO) cells are widely used for making therapeutic proteins, they have been very extensively studied and their optimal growth conditions well documented. An important process parameter for CHO cell cultures is the partial pressure of carbon dioxide, pCO_2 , in the medium. The pCO_2 also affects the pH and osmolarity of the culture medium as shown in Equation 1.1. Removal of CO_2 can increase pH and reduce osmolarity of the culture medium. A high pCO_2 in the medium can also cause the internal pH of the cells, pH_i , to drop since CO_2 is non-polar and hence, diffuses freely through the cell membrane. The decrease in pH_i can alter the cell metabolism and affect the performance of the cytosolic enzymes [46]. Moreover, changes in the cytoplasmic pH can also alter the pH in the endoplasmic reticulum which affects post-translational protein processing, like glycosylation and secretion.[71] Since CO_2 is a byproduct of cell metabolism, efficient stripping of CO_2 is necessary for a CHO cell bioreactor. CO_2 gas can also be used to control pH and it is a preferred strategy over liquid acid addition because it doesn't increase the osmolarity of the medium as much as liquid additions. However, when the CHO cells reach a high density, stripping of CO_2 gas will become harder and liquid base addition will be necessary to neutralize the acidity caused by the accumulation of CO_2 gas in the medium. For these reasons, pCO_2 control is very important for CHO cell micro-bioreactors since it affects osmolarity, pH and glycosylation of the cells. The optimal range of pCO_2 is between 31-75 mmHg (0.04-0.10 atm)and if it exceeds 99 mmHg (0.13 atm), it will be detrimental to the growth, productivity and product quality of CHO cells.





On a separate note, mild hypoxia has been shown to cause a decrease in oxygen consumption of the cells without affecting cell growth rate, maximum cell density, recombinant protein production rate or recombinant protein activity.[43] The CHO cell line also shows optimal growth in culture media with pH between 7.0 and 7.6. If the pH exceeds 8.2 or drops below 6.9, the protein glycosylation will be affected since the diffusion of unprotonated NH_3 at high pH(Equation 1.2) and CO_2 at low pH(Equation 1.1) through the cell membrane can alter the internal pH of the golgi apparatus.[7] The glucose uptake rate, q_{GLC} , is $1.0\text{-}1.5\text{ mMol}/10^{10}\text{ cells/h}$, the oxygen consumption rate, q_{O_2} , is $1.25\text{-}1.5\text{ mMol}/10^{10}\text{ cells/h}$, and the ratio of lactose production to glucose consumption rate, $Y_{LAC,GLC}$, is $1.1\text{-}1.2$ for CHO cells as reported in literature.[43] Typically for CHO cell culture, the desired osmolarity is in the range between 260-320mOsm/kg, mimicking serum at 290mOsm/kg.[58] The specific death rate of mammalian cells has been shown to steadily increase as the osmolarity is increased from 320 to 375 and 435 mOsm/kg. [15]

1.4 Design Specifications

1.4.1 Micro-bioreactors

Bench top bioreactors are the standards for scale down models of industrial bioreactors at a scale of 1000-10,000 times smaller than industrial bioreactors. What makes bench top bioreactors a good model and how can we scale it down even further to a microscale bioreactor 1000 times smaller than a 1L bench top bioreactor? Since volume and surface area scale differently with length, the physical and chemical environment experienced by the cells even in bench top bioreactors that are geometrically identical to industrial bioreactors will be different. The physical and chemical environment of the cells can strongly affect the cells' physiology and productivity and hence must be maintained constant or within the limits of critical values during scaling. First, the

gas transfer rate of O₂ and CO₂ must be sufficiently high so that dissolved oxygen level remain above the oxygen uptake rate of the cells and waste gas like carbon dioxide are efficiently removed. Secondly, the maximum shear rate experienced by the cells must remain the same or below the critical value that affects productivity during the scaling, this is especially important for mammalian cells like CHO due to their shear sensitivity.[33] The circulation time is also an important parameter since it affects the frequency at which the cells experience the high shear. The repeated deformation of the endoplasmic reticulum is reported to affect protein glycosylation.[22] Bioreactors with different chamber volumes will have very different circulation time before the cells circulate back to the tip of the impeller and hence, some bench top bioreactors are equipped with a circulation line that allows the physical environment of the cells to mimic the circulation time seen in large industrial scale bioreactors. On the other hand, the mixing rate of the micro-bioreactor must be sufficiently fast and uniform so that there is no region in the culture where the cell is nutrient starved or have a large concentration gradient. When designing scale down models of bioreactors, the energy dissipation rate has to be maintained constant so that the transfer of internal energy to the cell remains constant.

Micro-bioreactors can be instrumented with online sensors like pH, dissolved oxygen (DO), dissolved carbon dioxide (DCO₂) and optical density (OD) sensors. However, in order to fully characterize the condition of the cell culture offline sampling to monitor other important culture parameters will be necessary. Firstly, offline sampling for cell viability measurements is necessary to ensure that the cell viability remains high during the culture, since CHO cells are very fragile. It would be desirable if cell viability can be measured in real-time as an online sensor in the micro-bioreactor, like the dielectric spectroscopy electrodes which will be discussed in Chapter 3. For fed-batch cultures, where glucose is fed to the cells in the middle of the culture, osmolarity will be a very important parameter and can only be measured offline since it typically involves freezing the sample to determine the freezing point. A high osmolarity can repress cell metabolism and cause cell shrinkage. Next, to monitor cell health and productivity, the concentration of metabolites and product titer

in the culture medium needs to be measured and by conventional methods, these are measured offline since it requires the addition of reagents. In some cases, the online sensors will need to be recalibrated to account for any drifts during the culture and hence these measurements need to be performed offline using a blood gas analyzer as a standard for comparison. Furthermore, end point measurements to ensure that the final products have the right glycosylation, are not fragmented and have the right peptide groups and function, will be necessary. The growth chamber volume of the micro-bioreactor must have sufficient volume for these offline samples and also for the end point protein titer and quality analysis in order for these micro-bioreactors to function as well as bench top bioreactors for the earlier experiments.

The sample volume required for offline measurements on a few commercial instruments are shown in Table 1.2 Since the samples for these instruments are typically taken from shake flasks and large scale bioreactors, the recommended sample volumes for these instruments can be rather large. For micro-bioreactors, dilutions of the samples may be necessary to make up for the large volume required, since micro-bioreactors tend to have small working volumes. For cell viability measurements, hemacytometer measurements or manual counting under the optical microscope requires sample volume simply because only a small number of cells are counted, typically around 500 cells per hemacytometer. Statistically, counting 1000 cells would mean that the measured viability would lie within $\pm 5\%$ of the actual viability value of the population for 95% of the samples. If the hemacytometer counting were performed twice per measurement, the accuracy of $\pm 5\%$ can be achieved. However, to obtain a better accuracy, automated cell counting methods, for example the Cedex HiRes, Vi-CELL and Countess Analyzers, are used. The Cedex HiRes and Vi-CELL requires 300-500 μ L of sample volume and allow the user to select the number of images they want counted from the sample. The larger the number of images counted, the smaller the error but the image processing will be time-consuming. Dilutions of up to 10 folds are common when measuring samples with high cell density $\sim 10^8$ cells/mL. The measurable cell densities are between $10^4 - 10^9$ cells/mL and hence, even at an incubation density of 2×10^5 cells/mL, a dilution of 10 fold will still be

Table 1.2: Offline Sampling Volume Requirements

Cell Viability Measurements (5 Samples)

No	Instrument	Required Volume	Dilution	Sample Volume
1	Hemacytometer	25 μL	1:1 - 1:10	2.5 - 25 μL
2	Cedex HiRes Analyzer (Innovatis)	300 μL	1:10	30 μL
3	Vi-CELL (Beckman-Coulter)	500 μL	1:10	50 μL
4	Countess (Invitrogen)	10 μL	1:1 - 1:10	1 - 10 μL

Blood Gas Analyzer (2 Samples)

No	Instrument	Required Volume	Dilution	Sample Volume
1	Cobas b 221 (Roche)	50 μL	1:1	50 μL
2	Ciba Corning 840 (Corning)	45 μL	1:1	45 μL

Osmometer (5 Samples)

No	Instrument	Required Volume	Dilution	Sample Volume
1	Osmomat Auto (Gonotec)	50 μL	1:1	50 μL
2	5010 Osmette III (PSi)	10 μL	1:1	10 μL
3	Model 20G Osmometer (Advanced Instruments)	20 μL	1:1	20 μL

Metabolites and Protein Titer (5 Samples)

No	Instrument	Required Volume	Dilution	Sample Volume
1	RX Daytona (Randox)	150 μL	1:2	75 μL
2	YSI 2700 Select (Metabolites Only) (YSI)	100 μL	1:2	50 μL
3	Octet QK (Titer Only) (ForteBio)	100 μL	1:2	50 μL

Table 1.3: Downstream Processing Sampling Volume Requirements

No	Measurement	Minimum Weight	Volume (700mg/L)	Volume (500mg/L)
1	SEC (Size Fragmentation)	20 μg	30 μL	60 μL
2	SDS-PAGE (Electrophoretic Fractionation)	4 μg	10 μL	20 μL
3	Protein A HPLC (Purification)	20 μg	30 μL	60 μL
4	HPAEC-PAD (Glycosylation)	200 μg	300 μL	600 μL
5	WCX (Separation)	20 μg	30 μL	60 μL
Total		264 μg	400 μL	800 μL

within the measurement range. Since most users do not utilize all the images, a part of the sample will be discarded without being counted. This is the reason why not all automated cell counting machines require such a large volume. Countess, for example, requires only a 10 μL sample volume and hence can be used without requiring any dilution except for high cell density cultures.

The next measurement is the offline pH, dissolved oxygen (DO) and dissolved carbon dioxide (DCO₂) measurements using the blood gas analyzer. Since dissolved gas levels can change when the sample is removed from the environment of the growth chamber of the bioreactor, this measurement should be performed as fast as possible to prevent any degassing. Hence, the samples for the blood gas analyzer cannot be diluted. The recommended sample volumes for two commercial blood gas analyzers are shown in Table 1.2. The samples for offline osmolarity measurements using a freezing point osmometer also cannot be diluted because osmolarity is not a linear function of concentration for most biological fluids. A freezing point osmometer operates by measuring the depression of the freezing temperature due a change in chemical potential from the presence of solutes in the solution. The sample size is controlled by the size of the cooling chamber and temperature probe. From Table 1.2, we can see a wide range in recommended sample volumes for the freezing point osmometer. The last offline measurement is the measurement of the concentration of metabolites and product titer. The RX Daytona and YSI 2700 listed in Table 1.2 utilizes a pipette to draw out a fixed volume of samples to mix with different reagents that tests the different components in the sample. The RX Daytona can measure concentrations

of glucose, glutamine, glutamate, lactate, ammonia and immunoglobulin G (IgG) requiring only $57\mu\text{L}$ of sample volume for the reagents. However, since the machine dips an automated pipette into a tube to draw out the required volume, the sample volume required also depends on the depth of the pipette in the tube. From our experiments at Sanofi Aventis, Frankfurt, utilizing the RX Daytona, the minimum sample volume at the operating height for the automated pipette is $150\mu\text{L}$. The sample can be diluted 2 fold to reduce the sample volume needed, any further dilution would result in the glutamine concentration dropping below the measurement range for CHO media supplied with glutamate since glutamine will only be synthesized by the cells as needed. For the YSI 2700 analyzer, which measures the concentration of glucose, glutamate, glutamine and lactate, the pipetted volume is $25\ \mu\text{L}$ but the minimum sample volume needed for the operation of the machine is $100\mu\text{L}$. The YSI Analyzer has to be supplemented with the Octet QK for product titer measurements, requiring a sample volume of $100\ \mu\text{L}$. The recommended dilutions and final sample volume for each measurement are listed on the table together with the total number of offline samples needed for each parameter per 14 day CHO cell culture. From the table, it is estimated that the total volume removed for offline sampling is approximately 650 - $1000\mu\text{L}$, depending on which instruments are used. For the end point analysis, Table 1.3 shows the protein weight required for the different downstream analysis of protein titer and quality. The sample volume needed for downstream analysis are shown on the table for a product titer of 700mg/L and 350mg/L . The total volume needed for the end point analysis is between 400 - $800\ \mu\text{L}$. In order for the micro-bioreactor to provide sufficient sample volume for offline and downstream analysis, the working volume of the micro-bioreactor must have be 2mL or higher.

1.4.2 Viability Measurements in Micro-bioreactors

Maintaining high cell viability in the CHO cell population is an important first step before any experiments on CHO cells can be performed, be it in a micro-scale environment or a large scale environment. In large scale environments, offline sampling is often performed to monitor CHO cell population viability via a cell counting method

either optically with exclusion dyes or electrically using a Coulter counter. Since micro-bioreactors typically have cell suspension volumes between 10 nL to 1 mL, offline cell counting methods, typically requiring 20 L of sample each time, would significantly decrease the cell culture volume over a the culture period (typically 10 days). For micro-bioreactors, an online method is preferred for cell viability monitoring due to the small volume of the growth chamber. On the other hand, the higher data density of online sensors would be an added advantage for research based studies in microenvironments. Since the sensors will be in contact with the cell suspension, there are very stringent requirements on the types of sensors that can be utilized for online cell physiology monitoring. Firstly, the online sensing method must be able to perform its measurement without affecting cell viability, productivity and physiological state. With live cells, the conditions of the media will also change over time due to cell metabolism, hence a good online sensor must also be able to work reliably even under changing media conditions. Additionally, the sensor must also be sterile and non-toxic during the entire duration of the experiment and be compatible with common sterilization methods without compromising the sensor's physical or chemical conditions. Dielectric spectroscopy (DS) first introduced by Harris et. al [26] for online cell viability monitoring is ideal for micro-environments because it is label-free, scalable to micro-scale systems and compatible with most sterilization methods.

1.5 Review of State-of-the-Art

1.5.1 Micro-bioreactors

With the increasing demand for high throughput miniaturized instrumented bioreactors, micro-bioreactors with working volume below of 15mL and below have been developed by research groups and some are commercially available as well. The approaches are varied in form factor and implementations. The validation of disposable and non-invasive optical pH and DO sensors against electrochemical probes used by large scale bioreactors have spurred the integration of pH and dissolved oxygen (DO)

Table 1.4: Comparison of the capabilities and performance of state-of-the-art micro-bioreactors for CHO cells with bench top bioreactors

Type	Applikon 24	SIM Cell	HTBR	Ambr(TAP)	PIBA	RECA	Bench Top
Source	[11]	[41]	[35]	—	—	—	—
Max Density ($\times 10^6$ cells/mL)	2.6	12	2.3	—	5	30	30
$k_L a(h^{-1})$	<30	7	7	—	— (<500)	1-15	1-15
Volume	5-6 mL	300-700 μ L	35 mL	10-15 mL	1 mL	2 mL	1-30 L
Parallel Individual Control Sensors	24	6	12	24-48	2	2	1
pH	pH, Feed	—	pH, DO, Feed, DCO ₂	pH, DO, Feed T	pH, DO, Feed T, DCO ₂	pH, DO, Feed T, DCO ₂	pH, DO, Feed T, DCO ₂
pH,DO	pH, DO, OD	pH, DO	pH, DO	pH, DO, OD, T	pH, DO, T, DCO ₂	pH, DO, T, DCO ₂	pH, DO, T, DCO ₂
Incubator Agitation	Yes Shaker	Yes Rotator	Water Bath Rotator	Water Lines Propeller	No Membrane Deflection	No Membrane Deflection	No Propeller
Bench Validation Comments	Yes 24 Deep Well Plate	Yes Cassettes on a Rotator	Yes Miniature Bioreactors	— Miniature Bioreactors	— Microfluidics	Yes Microfluidics	— Bench Top Bioreactors

monitoring at the microscale.[34, 25] The implementation of optical DO sensors in shake flasks was the first step in bringing online sensing onto the shake flask platform. [24, 75] Weuster-Botz et al. have also demonstrated pH and feed control in DASGIP shake flasks with integrated syringe pumps for liquid injections and pH probes.[74] However, the periodic monitoring of DO and pH requires the flasks to be removed from the incubator to the sensor platform using an automated robotic arm, which is very costly.

In order to achieve a higher throughput, these optical pH and DO sensors have been integrated with 24 well plates. DO and pH control can be achieved by sparing oxygen and carbon dioxide through a permeable membrane at the bottom of the wells.[11, 31] The Applikon 24 well plate bioreactor works well for microbial cultivations[31], but has problems with foaming when used for Chinese Hamster Ovary (CHO) cells, even with the addition of anti-foam. This caused the bioreactor to lose DO control, and pH control have to be attained by manual liquid additions by an operator.[11] Bucheneauer et al. combined microfluidics and well plates in a single platform where automated liquid injections are performed using pneumatic valves in the microfluidic section under the well plate. The well plate has only 6 wells, of which 2 are used as reservoirs.[9] The integration of microfluidic pumps with well places can automate feed and liquid pH control. However, gas control of pH using CO₂ gas important for CHO cells is not present in this platform.

Besides modifying shake flasks and well plates, SimCell's solution for high throughput miniaturization is to design micro-bioreactors in the form of cassettes agitated by a rotator and a robotic arm is used to transfer the cassette from the rotator to a sensing platform for pH, DO and OD measurements. These online measurements are supplemented by sample removal for offline measurements of glucose, viability, titer and product quality.[41] However, the small sample volume removed and high dilutions for the sampling causes too large an error in the analysis of viable cell density, which have to be extrapolated for certain data points. The working volume of 500-700 μL as used by SIMCell is insufficient for frequent and accurate offline analysis. Ambr (TAP) biosystems developed micro-bioreactors with a much larger working volume,

up to 15mL each. The micro-bioreactors have a similar form factor to bench-top bioreactors with a stirrer in the middle of a cylindrical chamber. Liquid injection for feed and pH control is controlled by an automated pipette and pH and DO optical sensors are located under the chambers. The Ambr (TAP) micro-bioreactors are quite similar to bench-top bioreactors except that it lacks a CO₂ sensor and individual micro-bioreactor pH control using CO₂ gas.

1.5.2 Viability Sensors

Most of the current work on dielectric spectroscopy in micro-scale environments are on immobilized cells or in a flow device, e.g. flow cytometry. There are only two papers on cell viability measurements of suspended cells in micro-environments, specifically for yeast[30] and bacteria[23]. Iliescu et. al.[30] designed a simple microfluidic chip with three different two planar electrode configurations. They compared the dielectric spectra from 10⁷cells/mL of live yeast cells to dead yeast cells suspended in a phosphate buffered saline (PBS). Electrode polarization effects were not corrected in their dielectric spectra because the aim of the paper was not for utilizing the electrodes to quantify the density of live cells but to show the difference in the spectra due to the different electrode geometry. Gomez et al.[23] designed a silicon microfluidic chip with two parallel planar electrodes for measuring the viability of 10⁵-10⁹ cells/mL Listeria cells suspended in a Tris-Glycerine buffer in a 5.27nL chamber. Electrode polarization effects are corrected by the subtraction method using the spectra of the Tris-Glycerine buffer. In the two papers, cells were inoculated into a known buffer before measurement. There was no variability in the conditions of the buffer since the cells are freshly inoculated just before measurement. Unfortunately, this method cannot be used for an online measurement of cell viability since the cells will need to be resuspended in a special media.

To compare with industrial standards, the most common method for monitoring cell viability in Chinese Hamster Ovary (CHO) cells bioreactors is offline cell counting, either using an automated cell counter like the ViCell or manually via a hemacytometer. Such offline measurements require frequent sample removals and do

not provide real-time data. This problem is exacerbated for small volume reactors such as micro-bioreactors as frequent sampling may drastically reduce the suspension volume in the micro-bioreactor. For ethanol production by yeast, some bioreactors are equipped with the Aber probe system, which is a probe with 4 electrodes, using the principle of dielectric spectroscopy to monitor cell viability online. Dielectric spectroscopy is the preferred method of online cell viability monitoring since it is label-free, scalable to micro-scale systems and compatible with most sterilization method. In this thesis, we will develop dielectric spectroscopy electrodes for potential integration into the micro-bioreactor as an online cell viability sensor.

1.6 Predecessor Micro-bioreactors

1.6.1 PIBA Micro-bioreactor

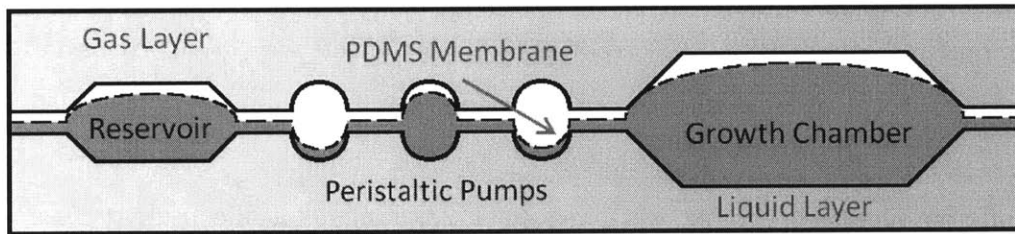


Figure 1-1: Simple diagram of the side profile of the micro-bioreactor showing the gas layer and liquid layer separated by a thin PDMS membrane.

The PIBA micro-bioreactor was the main micro-bioreactor for our experiments with Millennium Pharmaceutical CHO Cells. The micro-bioreactors fabricated in our group consists of two machined polycarbonate gas and liquid layer separated by a thin PDMS membrane ($70\mu\text{m}$). A side profile of the gas and liquid layer is shown in Figure 1-1 with schematics showing the reservoir for feeds, peristaltic pumps for injections and a mixer for the growth chamber. The deflection of the PDMS membrane actuates the valves and mixer inside the micro-bioreactor by pressurizing the gas layer with air. The membrane also permits gas transfer from the head space in the gas layer to

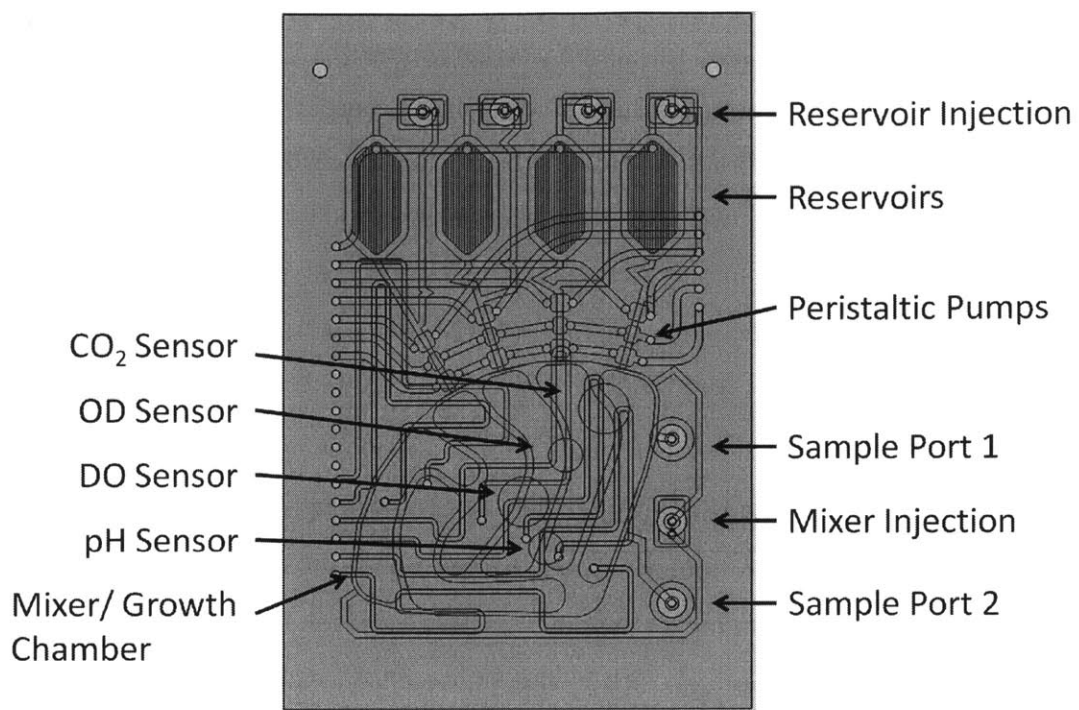


Figure 1-2: Top view of the PIBA micro-bioreactor designed for Chinese Hamster Ovary (CHO) cells cultivation in Millennium Pharmaceutical Inc (MPI).

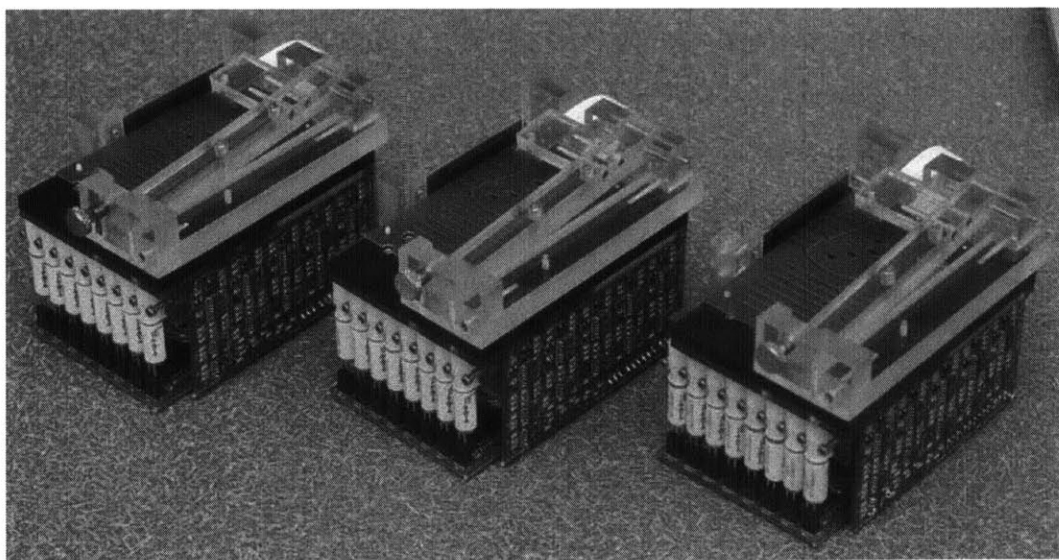


Figure 1-3: A photograph of the compact PIBA infrastructure, which includes the solenoid valves, the control boards and the gas manifold.

the cell culture in the growth chamber in the liquid layer. The gas layer and liquid layer are fabricated from CNC machined polycarbonate (PC) sheets and the PDMS membrane is fabricated from spinning PDMS solution onto a thin plastic sheet. The layers are then chemically bonded through the method described in a paper by Kevin Lee from our group.[39] In order to route the gas lines to the gas connector, a third layer made of CNC machined polycarbonate, the connector layer, is adhered to the gas layer using a double sided adhesive. There are occasions where one layer is insufficient for the high density of gas lines and hence, for the PIBA, there's a fourth layer for the gas lines.

The top view of the PIBA micro-bioreactor is shown in Figure 1-2. The four layers of the micro-bioreactor are superimposed in the figure. The bottom most layer, the liquid layer, have 4 chambers that act as feed reservoirs and one large growth chamber. The reservoirs and growth chamber are filled using pipettes through the PDMS septa fabricated by molding PDMS using machined PC molds. The PDMS septa are encapsulated in the two uppermost gas line layers and have a lip that opens up during injection. After injection, the PDMS septa automatically reseal themselves to form a sterile enclosure. These injections must be performed using sterile pipette tips inside a laminar flow hood. These PDMS septa are what distinguishes the PIBA from the other micro-bioreactors in our group. Harry Lee developed it specifically for sterile sampling of CHO cell cultures and has performed experiments to validate the septa's sealing abilities to maintain sterility. The feed reservoirs are filled at the beginning of the experiment with $100\mu\text{L}$ of solution in each chamber. If necessary, the reservoirs can be refilled during the experiments. The growth chamber is filled using the same method with 1mL of CHO culture. Since there is additional head space in the gas layer of the growth chamber, it is possible to fill the chamber with more than 1mL of liquid but this would reduce the chamber's mixing capabilities since this chamber is designed for 1mL working volume. The other distinguishing feature of the PIBA is how mixing is achieved in the PIBA. The PIBA growth chamber consist of one large chamber in the liquid layer and six smaller tubes in the gas layer that will be sequentially pressured to move the liquid around to induce mixing. The reservoirs

Table 1.5: Growth and Death Rate of CHO Cells for experiments with our micro-bioreactor (PIBA) compared with shake flasks and well plates for 3-5 day cultures

Experiment	3 Days		4 Days		5 Days		Agitation
	μ	κ	μ	κ	μ	κ	
Shake Flasks	0.715	5.0%	0.660	5.6%	0.606	4.7%	Shaker (250 rpm)
Well Plates (Inc)	0.604	4.9%	0.489	9.1%	0.463	9.0%	
PIBA NS (Inc)	0.643	5.8%	0.545	9.1%	0.600	6.6%	
PIBA NS - Full	0.624	9.0%	0.547	21.5%	0.309	34.3%	Continuous
PIBA NS - Mid	—	—	0.302	22.8%	—	—	10 min - 1 min
PIBA NS - Slow	—	—	0.601	11.9%	—	—	10 min - 6 sec
PIBA DO+pH (Inc)	—	—	0.537	8.6%	0.627	3.5%	
PIBA DO+pH (Inc)	—	—	-0.065	100%	—	—	Shaker(250 rpm)
PIBA DO+pH - F	0.227	36.2%	-0.161	100%	—	—	Continuous
PIBA DO+pH - M	—	—	0.148	38.1%	—	—	10 min - 1 min
PIBA DO+pH - S	—	—	0.306	50.6%	—	—	10 min - 6 sec

are connected by narrow channels to the growth chamber. There are 3 valves on top of this channel that forms a peristaltic pump to inject feeds from the reservoir to the growth chamber. Sampling is performed by inserting a sterile needle through a PDMS septum molded in the form of a short cylinder. Again, sampling has to be performed inside a laminar flow hood and the accuracy of the volume drawn is determined by the resolution of the syringe. The air resistance lines for the mixer to reduce shear stress on the cells are patterned on the fourth layer of the chip as shown in Figure 1-2. They are designed to be very narrow and long to increase the hydrodynamic resistance, R_h , in order to reduce the shear stress on the CHO cells. The hydrodynamic resistance for a rectangular channel is shown in the Equation 1.3 shown below, where μ refers to the dynamic viscosity of the fluid, L , w , and h refers to the length, width and height of the channel, assuming that $h < w$.

$$R_h = \frac{12\mu L}{wh^3(1 - 0.630h/w)} \quad (1.3)$$

The PIBA micro-bioreactor maintained sterility throughout the experiments and the gas transfer rate was high enough that even without mixing, the cells could be kept at more than 90% viability after 3 days of culture. However, after 5 days of culture, the working volume of the growth chamber in the PIBA had evaporated to

half its original volume. Moreover, the growth rates tend to vary widely over different experimental trials under the same set conditions. In some cases, the growth of CHO cells in the PIBAs are comparable to shake flask cultures, but in others, there seems to be evidence of growth inhibition and death rate acceleration. The average growth rate and death rate in percent of growth rate for the different 3-5 day CHO culture experiments are shown in Table 1.5. The evaporation problem can be compensated by modifying the Chemostat micro-bioreactor to work with CHO cells because the Chemostat micro-bioreactor allows for close loop evaporation compensation, which will be described in the next section.

In addition, there were problems with water condensation clogging the resistance lines and hence this causes irregular mixing during the experiments. If we look at Equation 1.3, since the dynamic viscosity of air, $\mu(\text{air}) = 1.983 \times 10^{-5} \text{ kg/ms}$ @ 300°K , is two orders of magnitude lower than the dynamic viscosity of water, $\mu(\text{water}) = 0.798 \times 10^{-3} \text{ kg/ms}$ @ 303°K , the time it takes for water to pass through the resistance lines will be roughly 100 times longer than it takes for air to flow though the resistance lines. Hence, the slow movement of water condensates on the resistance lines can cause the air lines to be jammed. The PIBA infrastructure is also very compact, as shown in Figure 1-3. The infrastructure in the figure contains the gas manifolds, solenoid valves, control boards, heater, LEDs and photodetector boards all configured compactly. In comparison, the Chemo micro-bioreactor and the RECA micro-bioreactor's infrastructure is spread out. The compact infrastructure of the PIBA makes it very portable but harder to modify if we need to integrate a new capability.

Some materials in the micro-bioreactor growth chamber could be leaching toxic molecules into the culture medium. Material tests with CHO cells cultured inside agitated deep well plates in an incubator with polycarbonate pieces (not shown), the tape bonding the polycarbonate pieces, pH and DO sensors are shown in Figure 1-4. Except for a pH sensor that seems to be contaminated, there is a slight growth inhibition and cell death rate increase for the pH sensor alone and the combination of pH and DO sensors in contact with the cell culture. Although the results with CHO culture experiments also show the same effects, these experiments need to re-

4 Days		TCD	%	μ	κ	Ave μ	Ave κ	StD μ	StD κ
Control	1	11.3	93.1	0.420	6.9%				
	2	6.4	87.9	0.267	12.1%	0.361	8.5%	±0.083	±3.1%
	3	10.4	93.4	0.397	6.6%				
Tape	1	8.6	92.8	0.347	7.2%				
	2	7.7	90.1	0.319	9.9%	0.344	9.3%	±0.024	±1.9%
	3	9.1	89.1	0.366	10.9%				
DO	1	6.9	92.0	0.288	8.0%				
	2	8.7	90.9	0.320	9.1%	0.346	8.2%	±0.056	±0.8%
	3	10.4	92.4	0.368	7.6%				
pH	1	6.3	90.1	0.237	9.9%				
	2	7.9	90.2	0.294	9.8%	0.265	9.9%	±0.044	±0.1%
	3	0.6	85.7	-0.364	100%				
pH + DO	1	3.7	88.6	0.112	11.4%				
	2	3.7	89.1	0.113	10.9%	0.121	13.4%	±0.14	±4.0%
	3	4.2	82.0	0.136	18.0%				

Figure 1-4: Toxicity Test using Agitated Deep Well Plates for 4 days

peated because these sensors are not pre-sterilized before the experiment and could potentially be the cause of a contamination. In order to ensure that this is truly the case, these experiments should be repeated with gamma irradiated sensors to prove that the toxicity of the sensors are the cause of growth inhibition and death rate increase for the PIBA DO+pH experiments with sterilized sensors in Table 1.5. It was discovered that the irregularity in experimental results could be caused by the clogging of the air resistance lines with water from the humidifier. This makes the mixing unpredictable and some of the mixers weren't even actuated at all. The clogged airlines also blocked gas transfer which could cause the cells to enter hypoxia or a drastic decrease in pH due to the accumulation of CO₂ gas. Moreover, the high evaporation rate could be causing the osmolarity to increase to a toxic level and thus killing the cells.

1.6.2 Chemostat Micro-bioreactor

The Chemostat micro-bioreactor designed by Kevin Lee is shown in Figure 1-5. The chemostat is designed for continuous culture and hence the volume control of the chemostat is very precise. The growth chamber working volume is geometrically controlled by the size of the 3 chambers, each chamber has a volume of 500 μ L. At any given time, the membrane in one of the mixing chambers is fully deflected down while the other two chambers have their membranes deflected upwards, i.e. the working volume is 1mL. This deflection is sequentially rotated through all the mixing chambers and it is the shuttling of fluid across narrow channels in between the mixers that induces turbulent flows and generates mixing. The working volume of the growth chamber can be kept constant by always ensuring that two chambers are always filled while one remain empty. This way, if there is evaporation, we can perform a closed loop water compensation by injecting water till the two chambers are filled completely, while one remains empty. Hence, the volume is always kept constant and evaporation can be compensated exactly. Moreover, a continuous culture requires continuous feed, so the feed reservoirs are connected directly to external reservoirs through barbs, instead of PDMS septa as in the PIBA. Similarly, the growth chamber

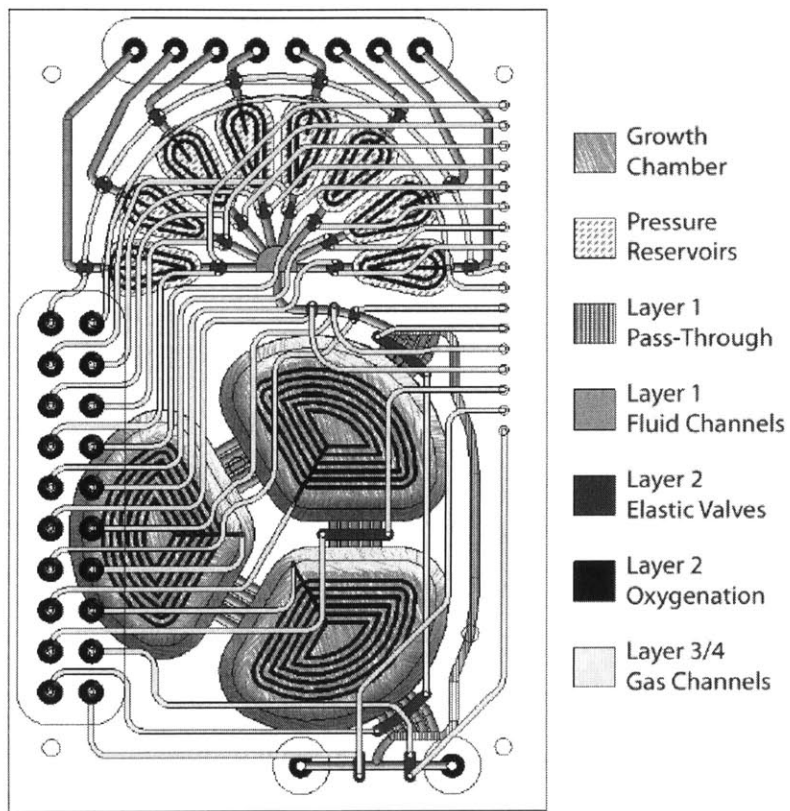


Figure 1-5: Top view of the Chemostat micro-bioreactor showing the positions of the input lines, feed reservoirs, peristaltic pumps, growth chamber, sensors and sampling port

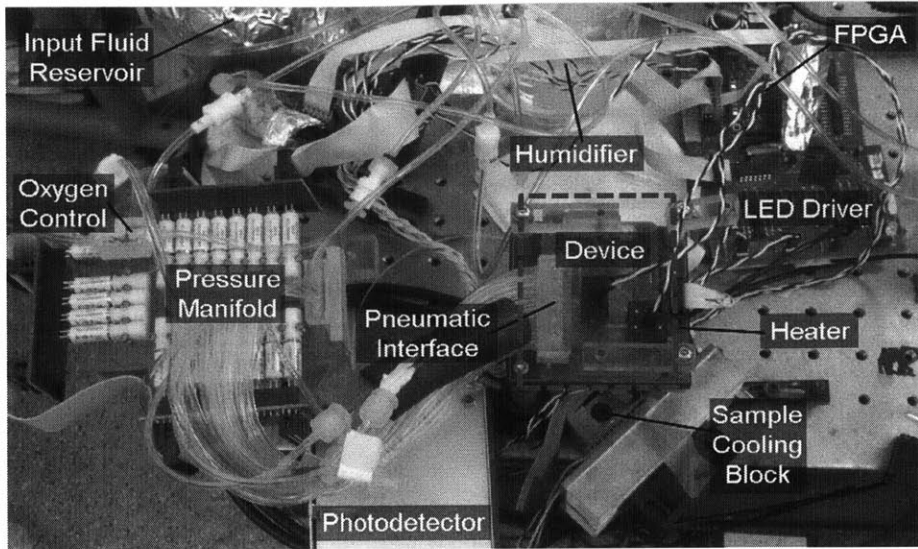


Figure 1-6: A photograph of the Chemostat micro-bioreactor infrastructure showing the FPGA board controlling the valves, the remote 80°C humidifier, the feed reservoir, the gas manifold, the heater, photodetector and LED driver printed circuit boards, and the cooling block for the sample.

is injected with cell culture through a barb with a valve that opens and blocks the channel connecting the barb to the growth chamber after injection. The sampling is performed through a separate barb connected to the same channel. Since this is a chemostat, there's a pass through channel on the side of the growth chamber where new medium is added into the growth chamber. The mixer is connected to this pass through channel and then the culture medium is mixed with the feed in the pass through channel. After uniform mixing has been achieved in all 3 chambers and the pass through channel, the mixture in the pass through channel is ejected either for sampling or as waste. Samples collected will be kept in an Eppendorf tube cooled by the sample cooling block as shown in Figure 1-6. However, for our experiments with Millennium, since the CHO is grown in batch, the pass through channel has not been utilized. In order to reduce shear stress on the cells, there are air resistance lines off-chip, placed along the air lines connecting the micro-bioreactor to the gas manifold. This facilitates optimizing the air resistance since resistance lines can be changed without having to change the micro-bioreactor.

For the chemostat micro-bioreactor, the channels in between the mixing chambers in the micro-bioreactor were narrow, and hence, to reduce shear stress, mixing rate has to be decreased to such a slow rate, that there was insufficient gas available for the cells. Our experiments used the same unmodified micro-bioreactor that had been designed for culturing *E. Coli*, a bacteria that is more robust than CHO cells. The CHO cells in the experiments stopped growing but their viability remained high after 3 days of culture indicating that they may be undergoing hypoxia, which can cause growth inhibition but not cell death. We ran a few experiments with the Chemostat micro-bioreactor. Working with the chemostat micro-bioreactor allowed us to change the resistance lines without swapping micro-bioreactors. It also allows us to perform closed loop evaporation compensation since the volume can be geometrically controlled. However, for our experiments with CHO culture from Sanofi, this advantage is lost since the working volume will vary irregularly due to sampling, but if we were to run this culture as a fed-batch culture, for more than half the culture days, close loop evaporation control can still be utilized. The maximum shear stress experienced by cells in the Chemostat occurs at the rectangular channels in between the mixers and hence can be determined exactly if the flow rate can be computationally modeled. This is unlike the PIBA where the location of the maximum shear is undetermined and the complicated dynamics of the PDMS membrane will need to be modeled to find the maximum shear stress experienced by the cells. The new micro-bioreactor for CHO cells attempts to leverage the existing infrastructure around the micro-bioreactor cassette. With these considerations that the new micro-bioreactor, RECA, will be based on the chemostat micro-bioreactor design and will employ some of the infrastructure from the chemostat micro-bioreactor. The next few sections will deal with the issues that the RECA micro-bioreactor will need to face, and following that, the design of the RECA micro-bioreactor, gas manifold and infrastructure.

1.7 Thesis Outline

A good scale down model of a bench top bioreactor should have similar controls and online monitoring abilities as the bench top bioreactor, which includes, individual control and online monitoring of pH, dissolved oxygen, dissolved carbon dioxide and temperature. There is also feed control in bench top bioreactors for fed batch cultures. The comparison between the state-of-the-art micro-bioreactors for CHO cells and bench top bioreactors are shown in Table 1.4. From the table, we can see that the current micro-bioreactors mostly only have pH and DO sensors.[11, 41, 35] Only the thinner micro-bioreactors like the SIM Cell bioreactor have integrated online optical density (OD) sensor to measure total cell density, however, the SIM-Cell bioreactor is the only one with less than the 2mL volume required for offline and downstream analysis.[41] Most of these micro-bioreactors need to be placed inside an incubator, except the Ambr(TAP) micro-bioreactor, and hence do not have individual gassing or temperature control like a bench top bioreactor. The Ambr(TAP) micro-bioreactors have individual gassing control but not individual temperature control since the heating is done through water lines running around all the micro-bioreactors. Ideally, we would want more online sensing in order to track certain important parameters in real-time, like cell viability. Monitoring viability online would greatly increase the ability to predict cell growth and health behavior by small changes in the culture process conditions and permit real-time correction to optimize cell growth and viability in the culture. Most CHO bioreactor processes are halted when the cell viability drops below 50% and hence having a real-time correction strategy would prolong cell viability and also assist pharmaceutical companies in understanding the factors that causes early or premature termination of a CHO cell culture.

In this thesis, we propose a 2mL working volume micro-bioreactor with closed-loop and individual control of pH, temperature, dissolved oxygen (DO) and partial pressure of carbon dioxide ($p\text{CO}_2$) levels in each micro-bioreactor. The design of the new micro-bioreactor (RECA) will be outlined in Chapter 2. The design has to meet the specifications of CHO culture which has a low shear tolerance, high chemical

sensitivity, long culture duration and high risk of contamination. Besides ensuring that the micro-bioreactor meets those requirements, the physical environment of the micro-bioreactor has to match those of bench top and large bioreactors for it to be an exact scale down model of industrial bioreactors. In Chapter 3, all the physical characterization of the performance of the RECA is measured and then compared with large bioreactors, these includes gas transfer rate (k_{La}) measurements for oxygen and carbon dioxide, mixing rate and shear stress. The new CO₂ sensor is also calibrated and optimized for the best sensitivity prior to the k_{La} measurements. In addition to matching physical characteristics to industrial bioreactors, the micro-scale bioreactor has an additional optical density (OD) sensor, typically not present in larger bioreactors for mammalian cells, to monitor the growth of CHO cells in real time. The OD sensor's performance on CHO cells is characterized to obtain good linearity between the total cell density and OD absorbance within the range of cell densities of the culture. Evaporation is a large problems when it comes to high surface to volume ratio working volume bioreactors, as in this case. Therefore, the evaporation rate is determined exactly at the end of this chapter to be able to estimate the volume of water needed to compensate for the effects of evaporation. Since the OD sensor in the micro-bioreactor cannot distinguish between live and dead cells, a viable cell density sensor utilizing dielectric spectroscopy is necessary to track cell viability during the culture. Since the dielectric spectroscopy(DS) sensor is a new sensor being developed for small scale bioreactors, this thesis will also explore the design for miniaturization, calibration to remove measurement parasitics, data analysis methods and biological validation of the DS sensor for the micro-bioreactor in Chapter 4. The cell lines used in this experiments will be industrial recombinant Chinese Hamster Ovary (r-CHO) cell lines provided by our industrial partner, Sanofi Aventis, Frankfurt, Germany. This will demonstratethe applicability of the RECA to culture industrially relevant, genetically modified r-CHO cells. The research conclusion and future work will be outlined in Chapter 5.

Chapter 2

Micro-bioreactor Design

2.1 Introduction

The new design of the micro-bioreactor is called a Resistive Evaporation Compensated Actuator (RECA) micro-bioreactor. The RECA is designed specifically to work for Chinese Hamster Ovary (CHO) cell culture with a 2mL working volume to accommodate the offline and end point analysis necessary to evaluate the performance of the micro-bioreactor. The new design for RECA will also need to perform reliably throughout the 10-14 days of culture time required, work even when the volume changes irregularly due to sampling and feeding, be capable of sterile sampling in a non-sterile environment, be capable of culturing shear sensitive cells such as CHO with high viability, and have integrated gas pH control in addition to liquid based pH control. These new requirements make RECA different from its predecessors and are summarized below:

1. Low Aeration Rate
2. Variable culture volume
3. Sterile reproducible sampling
4. Shear sensitive cells
5. Gas pH control

6. Salt sensitive cells

In the last chapter, an overview of the design of the group's predecessor micro-bioreactors before RECA, the PIBA by Harry Lee in Section 1.6.1 and the Chemostat by Kevin Lee in Section 1.6.2. Both micro-bioreactors have been very successful in culturing bacteria cells with results comparable to bench scale bioreactors and have been modified for CHO cell culture by the corresponding authors.[39, 38] These micro-bioreactors are used as the baseline model for the RECA micro-bioreactor with some modifications which will be described in this chapter. These modifications are necessary to ensure that the micro-bioreactor can withstand a long term culture (Section 2.2.1), be compatible with irregular working volume during the culture (Section 2.2.2) and can be sampled without contamination in a non-sterile environment (Section 2.2.3). The design of the RECA micro-bioreactor (Section 2.3.1), gas manifold (Section 2.3.2) and infrastructure (Section 2.3.3) is discussed in the corresponding sections. Finally, the future work on the resistance lines design to reduce shear stress on the cells and the gassing pH control will be discussed in Section ??.

2.2 Micro-bioreactor Modifications

2.2.1 Low Aeration Rate

The difficulties faced by the PIBA micro-bioreactor have a lot to do with the fact that problems surface when the micro-bioreactor is used for long term cultures (10-14 days) in combination with slow gas flow rates, even though for short term cultures (2-4 days) the PIBA micro-bioreactor has been very successful in culturing high density bacteria cultures. The issue is that when the PIBA was designed, these problems were not foreseen in the design and the compactness of its infrastructure makes it hard to modify the functions of the PIBA micro-bioreactor later on. For instance, for long term cultures, evaporation becomes a much larger problem. Kevin Lee performed an experiment to measure the evaporation rate for different humidification configuration with the results shown in Figure 2-1. First the natural evaporation rate with no

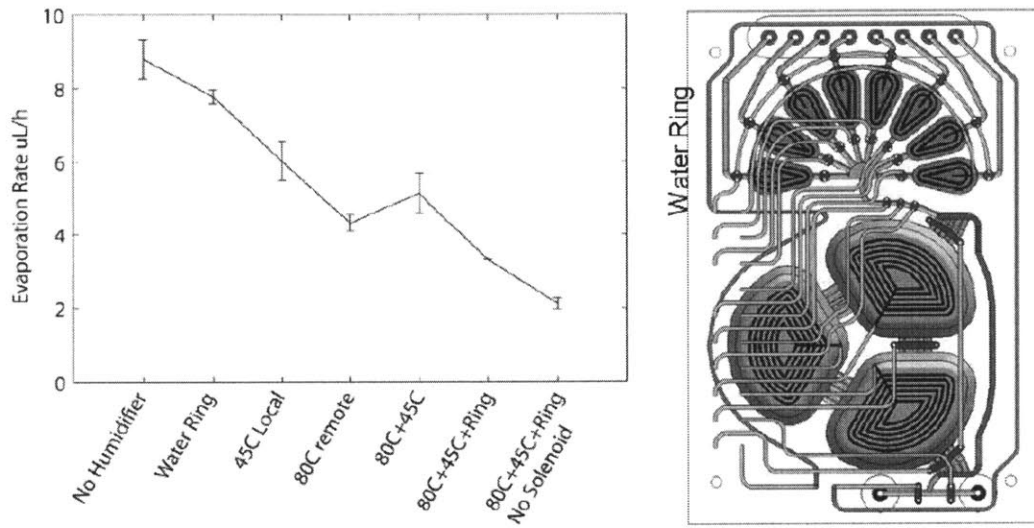


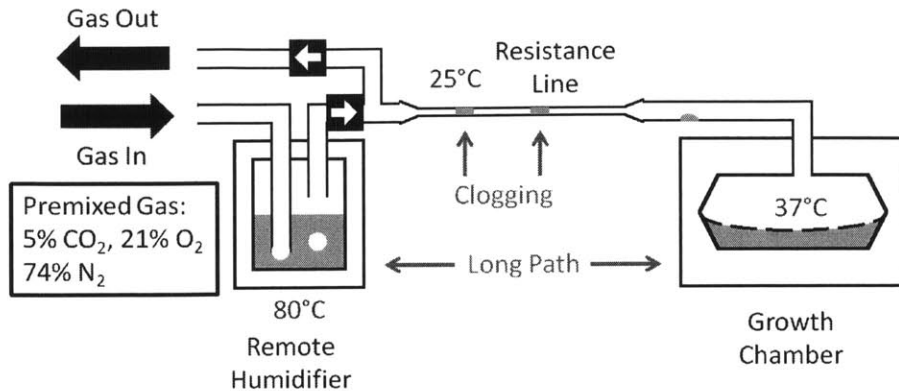
Figure 2-1: Evaporation rate of Chemostat for different humidification configurations. **Water Ring** refers to a water channel around the chip as shown by the purple line in the chemostat image. **45C Local** is a local humidifier at temperature 45°C placed between the gas manifold and the chip. **80C remote** refers to a remote humidifier at temperature 80°C placed at the gas input before the gas manifold, **80C+45C** is the combination of both the local and remote humidifiers, **80C+45C+Ring** is a combination of both humidifiers and the water ring, **80C+45C+Ring (No Solenoid)** is the combination of all above but with the solenoid removed to observe the effects of condensation on the cold metal part of the solenoid. Experiment performed by Kevin Lee on his chemostat for *E. Coli* growth.

humidification of the chemostat micro-bioreactor is measured to be around $9\mu\text{L}/\text{hour}$. That is around $200\mu\text{L}$ per day which is 20% of the 1mL working volume of the chemostat micro-bioreactor. With humidification, the best results are obtained when using the 80°C remote humidifier located at the beginning of the air lines with an evaporation rate of $5\mu\text{L}/\text{hour}$, i.e. $120\mu\text{L}/\text{day}$. Humidifying the air lines helps but it doesn't prevent evaporation completely. Theoretically, if the air above the mixer is humidified and completely saturated at 37°C , there should be no evaporation since the air above is saturated with water vapor for the given pressure and temperature. However, even though the air is saturated at 80°C , when it passes through the long air lines to reach the mixer at room temperature, the air is no longer saturated with water vapor at 37°C . And hence, even with an 80°C humidifier, there will be evaporation. Kevin tried experimenting with a 45°C local humidifier closer to the micro-bioreactor but that resulted in only slightly less humidification than the 80°C remote humidifier, with evaporation at $6\mu\text{L}/\text{hour}$, i.e. $144\mu\text{L}/\text{day}$.

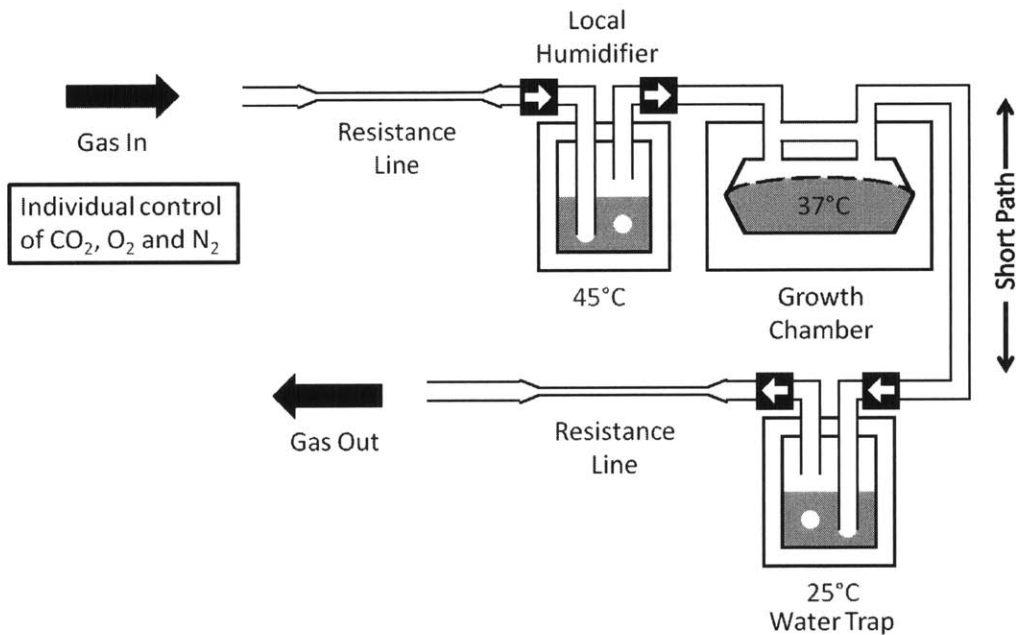
From the evaporation rate measured by Kevin, even with humidification, to prevent the culture from going into high osmolarity, evaporation compensation by injecting sterile water will be necessary for long term cultures. As described in Section 1.6.2, the Chemostat micro-bioreactor performs evaporation compensation by refilling the mixer with sterile water every 1-2 hours by injecting water till two of the three PDMS membranes in the mixer inflates fully. This method works well for fixed working volume cultures like the chemostat culture. As for the CHO culture that we are planning, the volume will be irregular throughout the culture due to offline sampling and feeding. Hence, closed loop correction for evaporation cannot be implemented at all times and the evaporation rate will need to be determined beforehand through a separate experiment. Water will be injected at the rate predicted by the evaporation rate measured under the same conditions. According to Kevin's measurements in Figure 2-1, if only 45°C local humidifiers were used, the evaporation rate would be $6\mu\text{L}/\text{hour}$. In order for the osmolarity to not change by 1-2% due to evaporation, an injection of $12\mu\text{L}$ of water every two hours would be sufficient for a working volume of 2mL. There are other methods of evaporation compensation in the literature but most

of them require the volume of the micro-bioreactor to be kept constant throughout the culture.[78] The alternative method for closed loop evaporation compensation without requiring the working volume to be kept constant would be to constantly weigh the local humidifier and the water trap and compensate for any weight increase by injecting the equivalent amount of water into the growth chamber.

The slow mixing rate for culturing CHO cells causes water to condense on the air lines, a problem that is not seen as much when there is greater air flow, as for bacteria cultures. This is especially true when a remote 80°C humidifier is used as shown in Figure 2-2(a) due to the long path that is unheated between the humidifier and the micro-bioreactor. The problem is further exacerbated when there are air resistance lines to reduce shear stress in the growth chamber. The viscosity of water is two orders of magnitude higher than air and in the narrow resistance channels, the flow rate of water is so slow that the membrane does not deflect at all within the duration of the mixer activation. Moreover, there is evidence that more condensation occurs with the presence of stainless steel parts in the solenoid valves in contact with humidified air due the higher thermal conductivity of metal as shown in the results of Kevin Lee in Figure 2-1. These experiments show a higher evaporation rate in the presence of solenoid valves than when the valves are removed. Water condensation on the solenoid valves, besides reducing the effectiveness of humidification, also can cause failures of solenoid valves over time. The new humidification strategy employs a local 45°C humidifier and a 25°C water trap as shown in Figure 2-2(b). This configuration prevents the humidified air from ever seeing the solenoid valves, which will ensure a longer lifetime of the valves. Also, in this configuration, the resistance lines are placed before the humidifier and after the water trap, hence, only dry air passes through the resistance lines to prevent any potential clogging of the resistance lines with water condensation. The downside of this method is that the air will equilibrate in the humidifier for a shorter period of time as compared to placing it at the beginning of the air lines like the 80°C remote humidifier, and hence the saturation of the air with water vapor may be incomplete. The evaporation rate with a local 45°C humidifier is predicted to be $6\mu\text{L}/\text{hour}$ for the chemostat micro-bioreactor which can



(a) Remote humidifier setup for PIBA micro-bioreactor used for experiments with CHO cells in Millennium Pharmaceutical Inc(MPI)



(b) New local humidifier setup for RECA micro-bioreactor with a water trap. The resistance lines are positions before the humidifier and after the water trap to ensure that the small resistance lines will not get clogged by water condensation. Moreover, a channel connecting between the gas in and gas out on the chip allows for flushing of the lines even when the membrane is touching the top chamber.

Figure 2-2: Schematic showing the previous humidifier strategy for the PIBA micro-bioreactor and the new humidifier strategy for RECA micro-bioreactor.

be easily compensated by water injections. Also, the additional water trap can act as a hydraulic equivalent of a capacitance on the mixer resistance, allowing the membrane deflection time to be increased since a high capacitance can increase the time constant of the deflection. This means that the resistance channels can be made wider and if there is any residual water in the channel, the droplet will be able to move faster in a wider channel. Moreover, the mixer now has separate input and output gas lines to enable flushing of the lines in case any part of the air lines are clogged. This flushing process will be performed periodically through the experiments and runs through the flush line on top of the mixers as shown in Figure 2-2(b).

2.2.2 Variable Culture Volume

As described in the last chapter, in order to completely characterize the micro-bioreactor, periodic offline sampling of $50\text{-}200\mu\text{L}$ is necessary. This causes the working volume of the micro-bioreactor to be irregular throughout the culture. In addition, for fed-batch cultures where extra feed is injected on certain days into the micro-bioreactor, in some cases the volume of the micro-bioreactor will exceed the designed working volume. The day to day volume variation expected for a batch and fed-batch 2mL working volume CHO culture is shown in Figure 2-3. If the volume in the mixer exceeds the designed maximum working volume of 2mL, the mixing will be incomplete and there will be dead zones in the mixer as illustrated in Figure 2-4. This is because the fluid will be stationary below the maximum deflection of the membrane. This can be a problem, especially for fed-batch cultures, since the volume of the micro-bioreactor is expected to exceed 2mL throughout the entire culture after Day 0. The solution is to oversample for the fed-batch culture, the oversampling strategy is shown in the last column of Figure 2-3. If we oversample to maintain a maximum volume of 2mL, closed loop evaporation compensation can be performed everyday except Day 6-8 and Day 12-14. This is an additional advantage of the oversampling strategy. For the days where closed loop evaporation compensation cannot be performed, injections will be made according to a the measured evaporation rate of the control experiments.

Day	2mL Batch			2mL Fed-Batch							
	Normal		Add	Normal		Add	Over Sample			Total	
	Samp.	Total		Samp.	Total		Samp.	Over			
0	0	2000	0	0	2000	0	0	0	2000		
1	0	2000	200	0	2200	200	0	200	2000		
2	0	2000	0	0	2200	0	0	0	2000		
3	155	1845	220	155	2265	200	155	45	2000		
4	0	1845	0	0	2265	0	0	0	2000		
5	0	1845	227	0	2492	200	0	200	2000		
6	155	1690	0	155	2337	0	155	0	1845		
7	50	1640	234	50	2520	185	50	0	1980		
8	0	1640	0	0	2520	0	0	0	1980		
9	155	1485	252	155	2617	198	155	23	2000		
10	0	1485	0	0	2617	0	0	0	2000		
11	0	1485	0	0	2617	0	0	0	2000		
12	80	1405	0	80	2537	0	80	0	1920		
13	75	1330	0	75	2462	0	75	0	1845		
14	205	1125	0	205	2257	0	205	0	1640		

Figure 2-3: Table with expected day to day working volumes of the RECA microbioreactor for batch culture, fed-batch culture and fed-batch culture with over-sampling to prevent over-filling of the growth chamber. The sampling protocol is the one defined by Sanofi-Aventis, Germany. The fed-batch protocol is assumed to be a feed of 10% increase by volume for days 1,3,5,7 and 9.

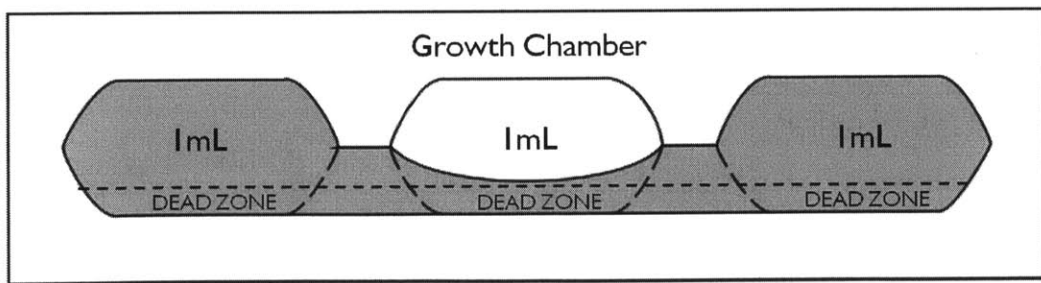


Figure 2-4: If volume exceeds 2mL, there will be incomplete mixing and a dead zone will develop. The solution is to oversample for fed-batch cultures to ensure that volume is always less than 2mL

2.2.3 Sterile Accurate Sampling

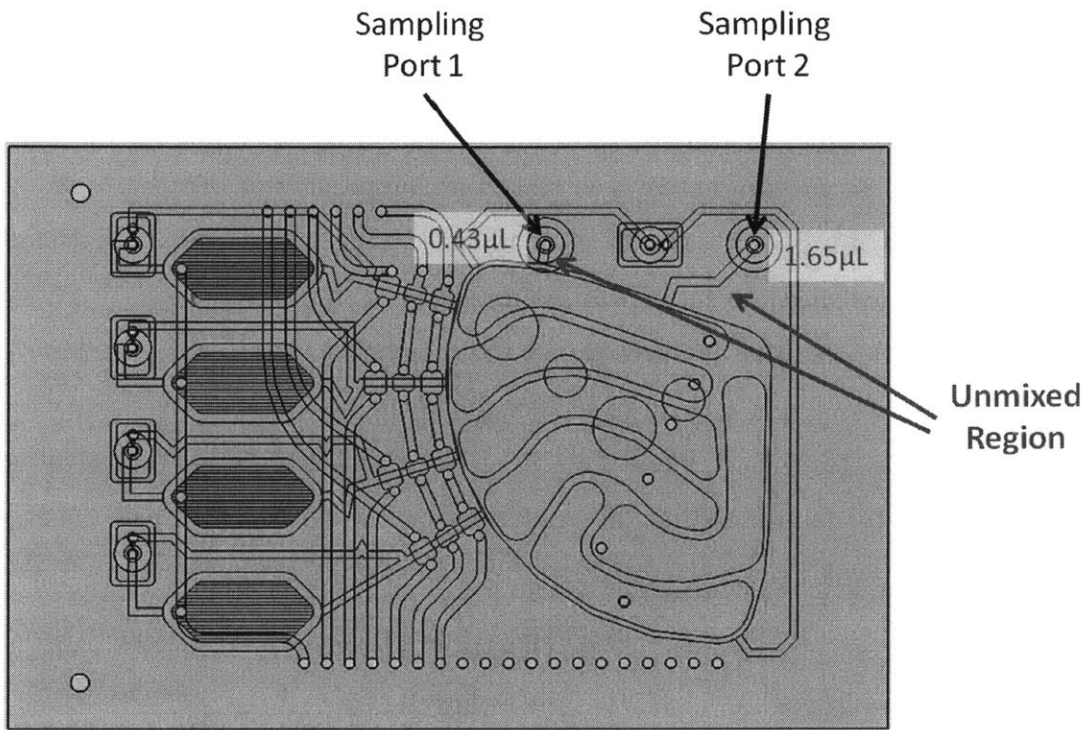


Figure 2-5: Schematic showing the sampling ports (A and B) of the PIBA micro-bioreactor with the unmixed volume of each sampling port.

Since offline sampling will need to be performed every 2-3 days, a sterile and accurate sampling strategy will need to be designed in the micro-bioreactor. Firstly, there must either be enough single use sample ports for the PIBA micro-bioreactor, which has PDMS septa for sampling through a sterile needle injected in a laminar flow hood. The septum reseals itself after use, but has a finite number of injections before it fails. From Figure 2-5, the PIBA has two sampling ports, Sample Port 1 and 2, where there is a channel connecting the sample ports to the growth chamber. After the first sampling, there will be leftover cells and culture in the channels connecting the PDMS septa to the growth chamber, especially for Sample Port 2, where the channel is longer. The culture left in this channel will remain unmixed for the duration of the culture and will contaminate the next sample with $0.43\mu\text{L}$ and $1.65\mu\text{L}$ of unmixed cells for Sample Port 1 and 2 respectively. For a sample volume of $50\mu\text{L}$, this results

in an error of 0.9-3.3%. The only way to prevent this from happening is either to have a very short channel, so that the error is minimized, or to have as many sample ports as the number of offline samples needed so that a port does not have to be reused. For CHO culture, there will need to be at least 6 sample periods, and hence, this would require six sampling ports which will be hard to fit inside such a small micro-bioreactor. So the alternative is to make the channel shorter in order to reduce contamination of subsequent samples with unmixed cells. Moreover, with PDMS septa, sampling will need to be performed in a laminar flow hood since there will need to be a sterile part that is injected into the chamber, be it a needle or a pipette tip. This makes sampling a little more challenging if the system is not as compact as the PIBA infrastructure or not run in a sterile environment. In addition, the accuracy of sampling will be determined by the gradations on the syringe and hence, a high resolution syringe will need to be purchased to draw 50-200 μ L samples. The PDMS septum also can be used only a certain number of times before it remains unsealable.

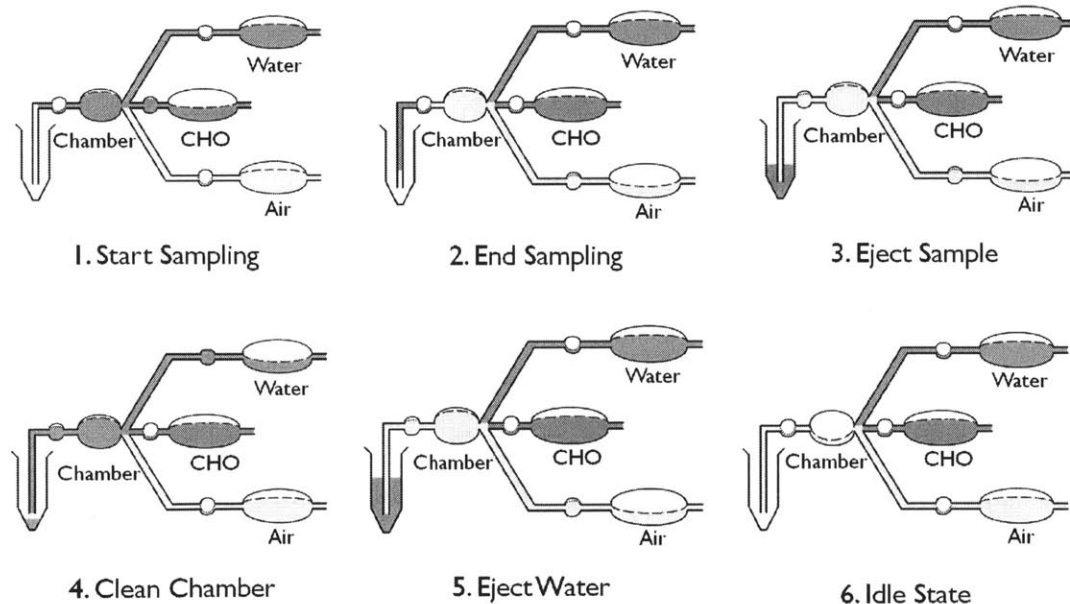


Figure 2-6: Schematic showing the sampling process of the RECA micro-bioreactor with ejecting of sample using air and cleaning of the 10 μ L sample reservoir with sterile water and then air drying it.

The Chemostat micro-bioreactor has a unique sampling strategy since it functions

as a continuous culture by default. For the continuous culture, feed is injected with a volume of $\sim 25\mu\text{L}$ and then an equal volume sample is ejected each time the feed is injected into the growth chamber. So sampling can be performed at any time point with a volume of $25\mu\text{L}$ each time. However, since our culture is not a continuous but a batch or fed-batch culture, the sampling strategy will need to be different. If we were to install a peristaltic pump such as the one for the feed injections at the same port, which injects $\sim 200\text{nL/s}$, it would require 16 minutes of continuous pumping to inject $200\mu\text{L}$ of sample. This is not practical and hence a larger sample reservoir is required. If a sample reservoir with $10\mu\text{L}$ volume is installed in the sample port, i.e. $10\mu\text{L/s}$, sampling of $200\mu\text{L}$ will require only 20 seconds of pumping. The sampling strategy employed by the new RECA micro-bioreactor with a $10\mu\text{L}$ reservoir is illustrated in Figure 2-6. The channel leading from the growth chamber to the sample reservoir must be as short as possible to reduce contamination of the sample with unmixed cell culture. The sample reservoir is also connected to the sterile water reservoir and the air line. The operation of the sampling port is illustrated in Figure 2-6. First, sample from the growth chamber is pumped into the sample chamber and pumped out into the tube connecting the sample barb to the Eppendorf tube. After the desired sample volume is pumped out from the growth chamber, air is pumped into the sample reservoir to push all the sample into the Eppendorf tube. Then water is run through the sample reservoir to clean the reservoir in step 4. After cleaning, air is again injected into the sample reservoir to dry it and keep it clean till the next sample removal. The actual design of the sample port is shown in the full design of the micro-bioreactor in Section 2.3.1.

2.2.4 Shear Sensitive Cells

Chinese Hamster Ovary (CHO) cells are very shear sensitive because they lack protective cell walls (only a cell membrane separates the contents of the cell cytoplasm from the external media) and their large size ($10\text{-}20 \mu\text{m}$) compared to bacteria cells. CHO cells are typically grown as adherent cell cultures in micro-carriers or suspension cultures in bioreactor tanks. Adherent cells are more susceptible to shear stress as

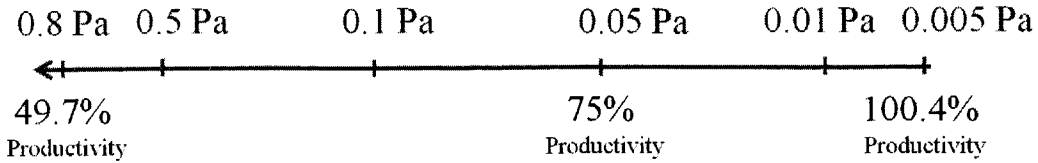
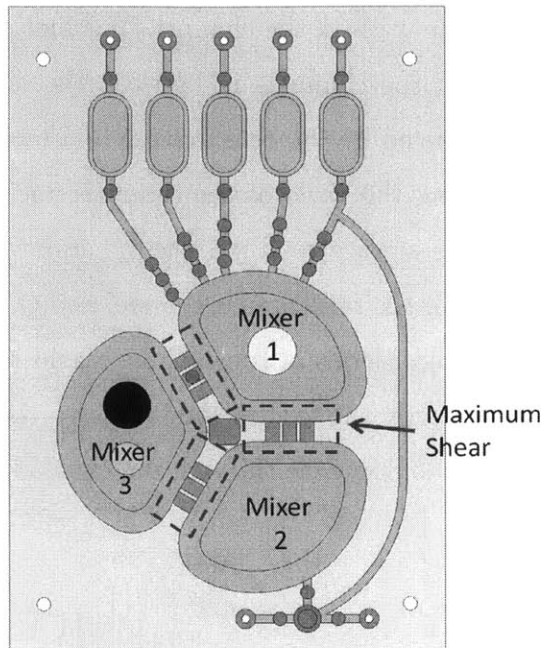


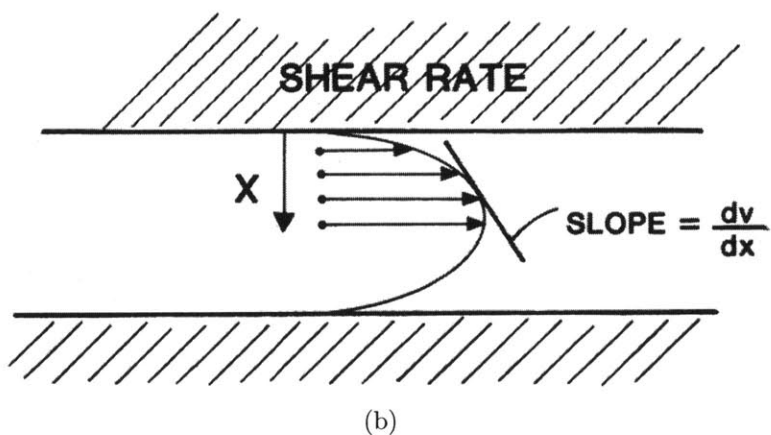
Figure 2-7: Schematic showing the effects on productivity of recombinant CHO cells due to different shear rates.[33]

compared to cells grown in suspension because they cannot freely rotate or translate to accommodate the shear forces. The CHO cells grown in our micro-bioreactor are suspension type cell cultures. Keane et al. studied the effects of shear stress on the growth and productivity of adherent recombinant CHO cell cultures.[33] In his paper, he used a flow chamber to apply a steady laminar shear stress ranging from 0.80 Pa to 0.005 Pa. In this range of shear stress, no morphological changes to the cells were observed and viability remained at > 90%. Without the addition of any shear protectants, productivity ceased completely at a shear stress of 0.1 Pa. The addition of Pluronic F-68 (0.2% [w/v]) as a shear protectant, productivity is restored at the rate that is shown in Figure 2-7. The productivity is reported as a percentage of the productivity of the control CHO culture which is static. The mixing rate that generates low shear tends to be slow. This might cause problems if the slow mixing rate causes a region in the growth chamber to be nutrient depleted for a period that is longer than the starvation time of the cells, if the slow mixing rate results in a pH gradient across the growth chamber for an extended period of time, or if the slow mixing causes too low a gas transfer rate of oxygen to support the cell density or carbon dioxide to maintain the pH level. Hence, a balance between slow mixing for low shear and fast mixing for a well aerated, homogenous culture must be achieved in order to support the growth of CHO cells in the micro-bioreactor.

From the design of the micro-bioreactor, as shown in Figure 2-8(a), the region where maximum shear occurs is along the small channels connecting the mixing chambers, highlighted in red. These channels are narrow and the no slip condition on the boundary (walls) of the rectangular channel restricts the fluid velocity at the bound-



(a)



(b)

Figure 2-8: (a)The region of maximum shear in our mixer design for our micro-bioreactor for CHO cells, highlighted in a dashed rectangular outline, and (b) the Poiseuille flow profile in a channel with the shear stress on the cells given by the slope of the velocity profile multiplied by the dynamic viscosity.

ary to be zero. For a pressure driven flow, the flow profile is parabolic, known as a Poiseuille flow, as shown in Figure 2-8(b). Since the shear stress experienced by the cells is given by the dynamic viscosity multiplied by the slope of the velocity, the highest shear stress is along the walls of the channel. The first step in reducing shear stress on the cells is to widen the channels in between the mixing chambers. The maximum shear stress experienced by the cells flowing in a rectangular channel with a Poiseuille flow profile is along the walls of the channels and given by the relation in Equation 2.1, where τ is the shear stress, η is the dynamic viscosity of water, w is the width and h is the height of the rectangular channel and Q is the flow rate. From the equation, increasing the dimensions of the channel would reduce the shear stress experienced by the cells, especially the height. Additionally, the shear stress can also be reduced by slowing down the flow rate through the channel, Q .

$$\tau = \eta \frac{\partial u}{\partial z} = \frac{6\eta}{wh^2} Q \quad (2.1)$$

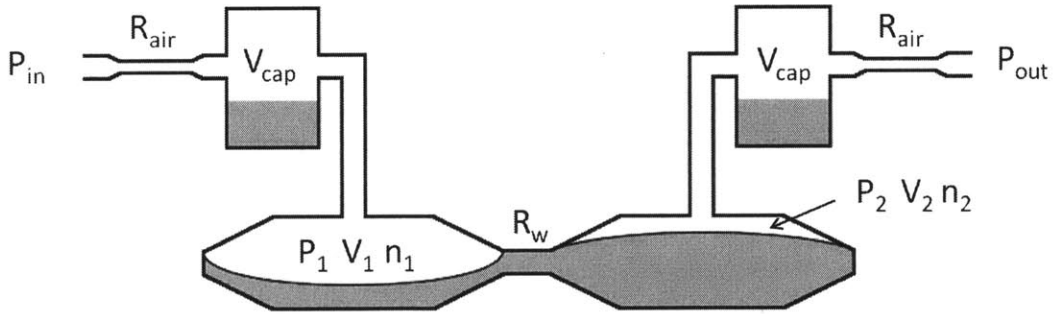


Figure 2-9: Schematic showing the parameters used in the modeling of the shear stress along the channel in between the mixers.

In the new design, the channels are widened to have a width, w , of 0.0625 in (1.56 mm) and a height, h , of 0.085 in (2.16 mm), to minimize the shear stress experienced by the cells when traveling through these channels. These are the maximum dimensions for the channels of a growth chamber with a working volume of 2mL in the form factor of our micro-bioreactor. Besides widening the channels, the flow through

the channels need to be slowed down as well. To achieve that, resistance lines are added to the air lines pressurizing the membrane inside the mixing chambers. These are shown in Figure 2-9 with the resistance of the air resistance lines labeled by R_{air} . There are also water traps and humidifiers acting as an electrical equivalent of 'capacitors' to further increase the time constant of the deflection. These volume of these 'capacitors' are represented by V_{cap} in Figure 2-9. The presence of V_{cap} slows down the deflection of the PDMS membrane in the mixing chamber and hence the flow rate through the channels, because it takes longer to pressurize a chamber with a larger volume. In order to design resistance lines to achieve shear stress in the channels that is below the critical shear stress that can be tolerated by CHO cells, a computational modeling of the shear stress as a function of different resistances, R_{air} , is performed.

The deflection of the PDMS membrane is difficult to model completely since it has a non-circular shape, more like a triangle with rounded corners. The deflection will spread out radially outward from the center of the chamber and stop when it hits the edge or the bottom of the chamber. The deflection of the membrane due to the pressure as a function of radius from the center is approximated with the small deflection plate theory for a clamped circular membrane.[19] The small deflection plate theory is used because the large deflection plate theory is impossible to invert and moreover, our deflection is too large even for the large deflection plate theory, which is only applicable for deflections of less than 6 times the thickness of the membrane. The small deflection plate theory will slightly overestimate the deflection and hence overestimate the maximum shear stress in the channels connecting the mixing chambers and underestimate the mixing time. For a circular plate with uniformly distributed load, the deflection of the plate, w , of thickness h as a function of the radius, ρ , when the plate is clamped at the circumference of a radius of a for a uniformly applied pressure, P , is given by the following equation:

$$w(\rho) = \frac{Pa^4}{64D} \left[1 - \left(\frac{\rho}{a} \right)^2 \right]^2 \quad \text{where } D = \frac{Eh^3}{12(1 - \nu^2)} \quad (2.2)$$

where D is the flexural rigidity, E is the Young's modulus, h is the plate thickness

and ν is the Poisson's ratio for the thin plate.

Integrating the deflection, $w(\rho)$, over the area of the PDMS membrane gives the volume in the chamber. If we assume V_{ss} to be the gas volume in the mixing chamber when the membrane is flat, V_n and P_n to be the instantaneous gas volume and pressure in mixing chamber n , and P_o to be the pressure at which the membrane starts touching the bottom of the chamber, we can get a relationship for membrane pressure as a function of the gas volume inside the mixing chamber. There will be two relations, one for the case when the membrane is moving freely in the chamber, $P_n < P_o$ and the other for the case when the membrane starts laminating on the bottom of the chamber, $P_n \geq P_o$. Solving Equation 2.2 by letting $w(0) = z$ where $z = 0.085\text{in}$ (2.16 mm), is the height of the chamber, P_o is calculated to be $P_o = 64Dz/a^4$.

$$P_{mem(n)} = \begin{cases} 3P_o \left(\frac{V_n - V_{ss}}{V_{ss}} \right), & \text{for } P_n < P_o \\ \frac{4P_o}{9} \left(\frac{V_{ss}}{2V_{ss} - V_n} \right)^2, & \text{for } P_n \geq P_o \end{cases} \quad (2.3)$$

Knowing the pressure that the membrane exerts on the gas, $P_{mem(n)}$ for a given volume, V_n , the total pressure exerted on the gas due to the applied pressure and the membrane pressure can be calculated. This pressure drives the deflection of the membrane and hence determines the flow rate through the channels. For an applied pressure of P_{in} to the first chamber through a resistance line to the first mixing chamber and P_{out} respectively for the second chamber as shown in Figure 2-9, we can derive 4 simultaneous equations describing (1) the rate of change of in moles of gas molecules in chamber 1 (Equation 2.4), (2) the rate of change in moles of gas molecules in chamber 2 (Equation 2.5), (3) the rate of change of gas volume in chamber 1 (Equation 2.6) and correspondingly (4) the rate of change of gas volume in chamber 2 (Equation 2.7).

$$\frac{\partial n_1}{\partial t} = \frac{P_{in} - P_1}{R_{air}} \frac{P_1}{RT}, \quad \text{with } P_1 = \frac{n_1 RT}{V_1 + V_{cap}} \quad (2.4)$$

$$\frac{\partial n_2}{\partial t} = \frac{P_{out} - P_2}{R_{air}} \frac{P_2}{RT}, \quad \text{with } P_2 = \frac{n_2 RT}{V_2 + V_{cap}} \quad (2.5)$$

$$\frac{\partial V_1}{\partial t} = \frac{P_1 - P_{mem_1} - P_2 + P_{mem_2}}{R_w} \quad (2.6)$$

$$\frac{\partial V_2}{\partial t} = \frac{(P_2 - P_{mem_2} - P_1 + P_{mem_1})}{R_w} \quad (2.7)$$

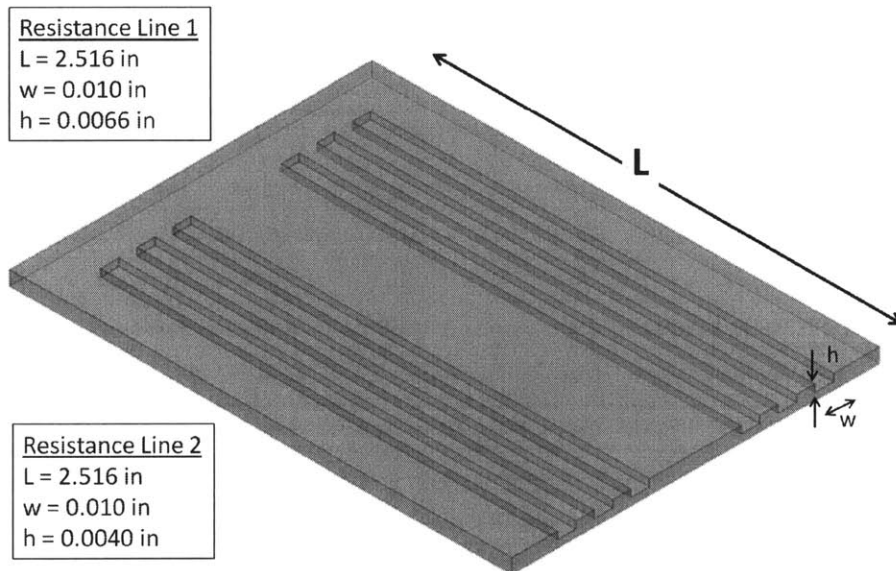
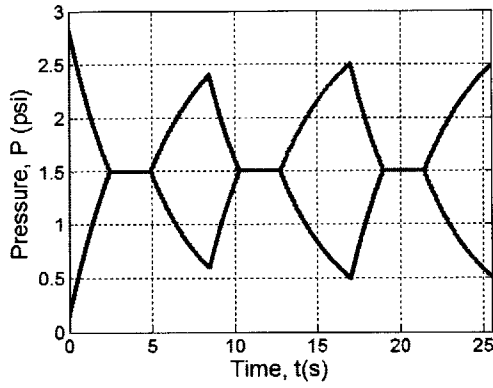
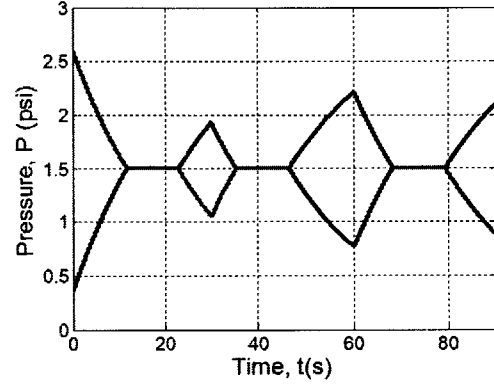


Figure 2-10: Schematic showing the air resistance lines used and their dimensions. There are 6 resistance lines, 2 for each mixer (input and output).

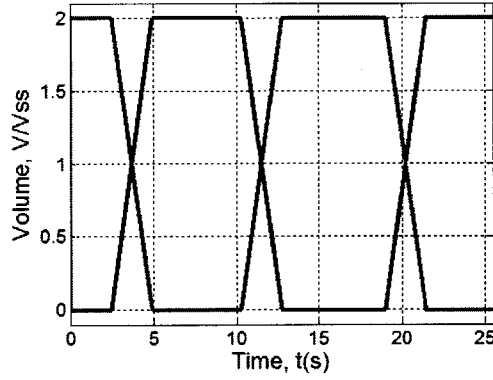
For our Sylgard 184 PDMS membrane, the Young's modulus, E , at 23°C is 1.84 Pa as reported by Sandia National Laboratories on their website. The Poisson's ratio, ν , for PDMS is 0.5 as reported in the Polymer Data Handbook.[49] The PDMS membrane is fabricated by spinning a blob of PDMS into a thin film of 70 μ m thickness. For a pressure driven Poiseuille flow profile, the hydrodynamic resistance of the three rectangular channels connecting the mixers with a width, w , of 0.0625 in (1.56 mm), height, h , of 0.085 in (2.16 mm), and length, L , of 0.09375 in (2.38 mm) for water with a dynamic viscosity, η of $0.697 \times 10^{-3} Ns/m^2$ is given by the following equation.



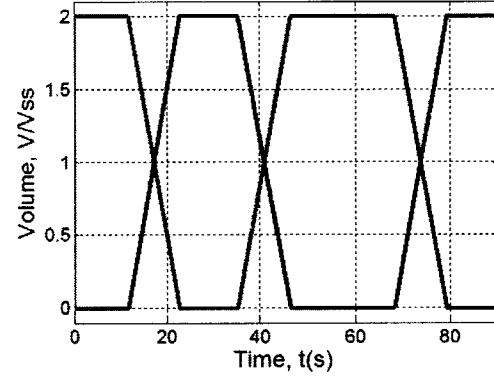
(a) Resistance Line 1



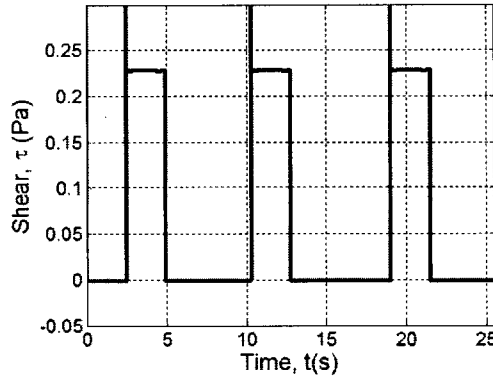
(b) Resistance Line 2



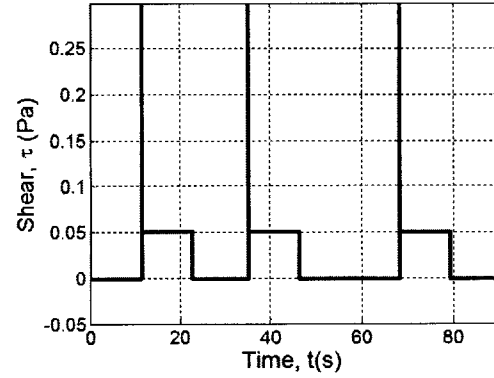
(c) Resistance Line 1



(d) Resistance Line 2



(e) Resistance Line 1



(f) Resistance Line 2

Figure 2-11: FDTD Modeling of the maximum shear stress inside the channel between the mixers for resistance line 1 and resistance line 2.

$$R_w = \frac{12\eta L}{wh^3} = 1.25 \times 10^6 Ns/m^5 \quad (2.8)$$

Using a Finite Difference Time Domain (FDTD) method, the flow rate through the channels for an operating pressure of 3 psi ($2.06 \times 10^5 Pa$) is modeled for the two resistance lines shown in Figure 2-10. The results are shown in Figure 2-11. The Matlab code is in Appendix A. In this model, there are a few assumptions that are different from the actual mixer design. Firstly, the model assumes a circular mixer, but the actual mixer is pie-shaped as shown in Figure 2-8(a). Equation 2.3 assumes the circular shape, we would expect the volume change with pressure to be different and it will definitely take more pressure to completely seal a triangular shaped mixing chamber as compared with a circular one, i.e. the $\partial V/\partial t$ will be lower in the actual case compared to the computational model. From our experiments in the next chapter, the membrane deflection was definitely slower than predicted with the FDTD model. There will be more discussion on this disparity in the next chapter.

2.3 Micro-bioreactor Design

2.3.1 RECA Micro-bioreactor

The design of the Resistive Evaporation Compensated Actuator (RECA) micro-bioreactor is shown in Figure 2-12. There are 5 reservoirs for injections, including one containing sterile water for evaporation compensation. The other four reservoirs are reserved for Sodium Bicarbonate ($NaHCO_3$) base injections, feed, and other necessary supplements. The injection is performed by a peristaltic pump actuated through the PDMS membrane sequentially pushing a plug of fluid into the growth chamber. The growth chamber looks similar to the Chemostat micro-bioreactor but is now doubled in volume to 2mL. Uniform mixing is obtained by pushing fluids through small channels connecting the three growth chambers, each having a volume of 1mL. There is also a $10\mu L$ reservoir for sampling located after the growth chamber. The sampling will be performed via peristaltic pumping of $10\mu L$ plugs. Besides the connection to

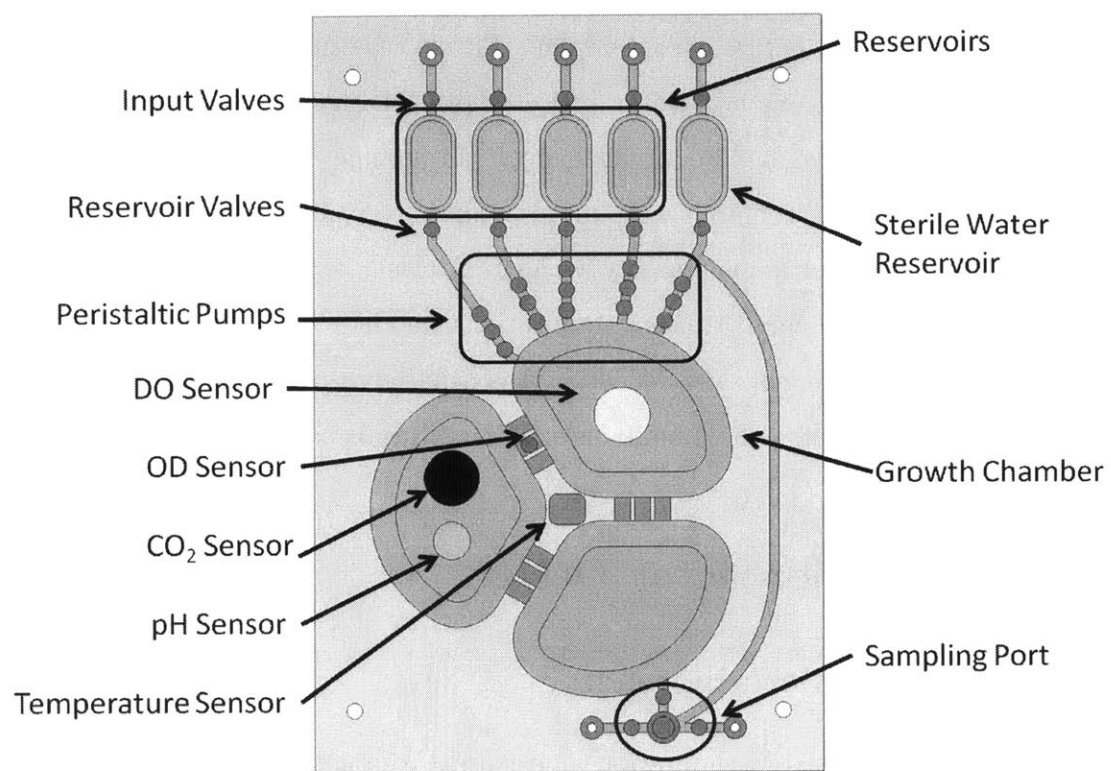


Figure 2-12: Top view of the RECA micro-bioreactor showing the positions of the input lines, feed reservoirs, peristaltic pumps, growth chamber, sensors and sampling port

the growth chamber, the sample reservoir is also connected via a channel to the sterile water line and a clean air line. Air will be injected through the sample reservoir to eject any remaining sample into the sampling container, e.g. an Eppendorf tube, and water will be injected after that to clean the sample reservoir from any cell culture or cells remaining. Clean air will then be sent through the reservoir to dry the chambers so that there would no water left to dilute the next sample. This process is repeated every sampling step.

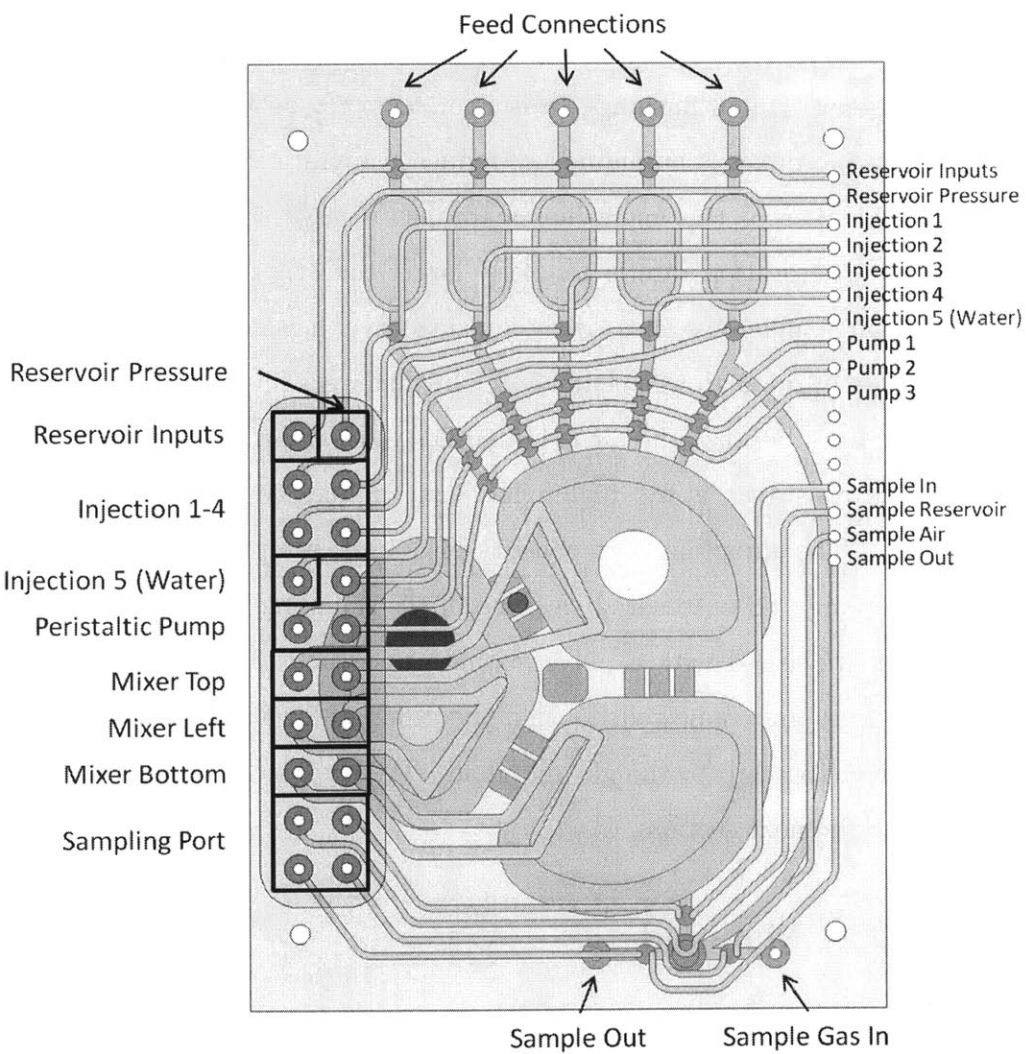


Figure 2-13: Top view of the RECA micro-bioreactor showing gas connections to the gas manifold

The connections from the RECA micro-bioreactor to the gas manifold is shown in Figure 2-13. All reservoir input valves share the same gas line since it is unnecessary to individually control each input valve. The reservoir pressure is set to be 1.5 psi ($1.03 \times 10^5 Pa$), which is lower than that of the mixing pressure of 3 psi ($2.06 \times 10^5 Pa$). The aim of the reservoir pressure is to ensure that the input to the peristaltic pumps see the same pressure and is unaffected by external hydrostatic pressure to ensure consistent pumping volume. The output of the reservoir, i.e. the injection valves, are individually controlled by separate gas lines because these are the valves that determine which feed lines are being injected into the growth chamber. Then comes the gas lines that control the peristaltic pumps. The mixers have a separate input and output line in order to allow flushing of water condensation on the mixer lines since the air coming into the mixer is humidified to reduce evaporation of the growth culture. The growth chamber of the micro-bioreactor has a large surface to volume ratio and hence, the evaporation rate is generally larger than that for larger bioreactors. Moreover, all three mixer gas lines are designed to have the same resistance, to ensure even mixing rate in the 3 growth chambers. The mixer gas lines are made wider than the rest of the lines because the air is humidified, and any condensation might clog the lines if the resistance is too high. The last air lines control the valves to the sampling port. The sampling port consists of a $10\mu L$ sample reservoir and valves to control sampling and automated cleaning of the sampling port. The holes in the top left corner are sealed with a polycarbonate cover and taped with double sided tape. The air lines are connected through the group of 20 barbs located on the left bottom corner of the chip to the gas manifold. The design of the gas manifold will be discussed in the next section.

2.3.2 RECA Manifold

A manifold is fabricated to connect the solenoid valves to the air lines to the micro-bioreactor. The design of the gas manifold is shown in Figure 2-14. The manifold has 3 layers. The barb connectors to the micro-bioreactor are situated in the center of the top layer of the manifold. The middle layer routes the output of the solenoid valves to

the barb connectors that connects the manifold to the micro-bioreactor. The bottom layer routes the main air lines to the inputs of the solenoid valves. Figure 2-15 lists all the valves with their numbers as shown in Figure 2-14 and the gas connections for easier referencing. In the table, NO stands for Normally Open and NC stands for Normally Close. The selection of which gas lines is normally open or normally closed is usually selected to be the most common state of the valve, so that more often than not, the valve is inactive, to save energy consumption. In particular, Valve 10 (Pump 2) is set to 'off' normally while all the rest of the valves are set to 'on' normally. There are also 4 gas mixer solenoid valves besides the solenoid valves needed for mixing and valving on the micro-bioreactor. Control of carbon dioxide (CO_2) gas concentration vs nitrogen (N_2) gas is achieved by changing the duty cycle of Gas Mix 3 solenoid valve. Oxygen (O_2) gas concentration is controlled via Gas Mix 2 via the same strategy. Then the two outputs are mixed together in a 50-50 duty cycle using Gas Mix 1. Gas Mix 4 is currently unused but will be available for use in case any extra valving is needed.

2.3.3 RECA Infrastructure

The complete setup is shown in Figure 2-16. The laptop controls an Field-programmable Gate Array (FPGA) board that controls the solenoid boards, the heater board and photo-detector board. The air lines are connected to a pressure regulator before being connected to the gas manifold. From the gas manifold, the valve lines are connected directly to the micro-bioreactor. The mixer input lines are connected first through an air resistance line, followed by a 45°C local humidifier before reaching the micro-bioreactor. The mixer output lines from the micro-bioreactor are connected to the water trap, then to the air resistance lines and then only to the gas manifold. The infrastructure is very similar to the Chemostat micro-bioreactor infrastructure shown in Figure 1-6, but with a few changes. First the gas manifold for the RECA is much bigger because it needs to accommodate 4 more solenoid valves to support flushing of mixer lines. Secondly, there is no remote humidifier in this setup, only a local humidifier. The RECA infrastructure also has the addition of a water trap. The po-

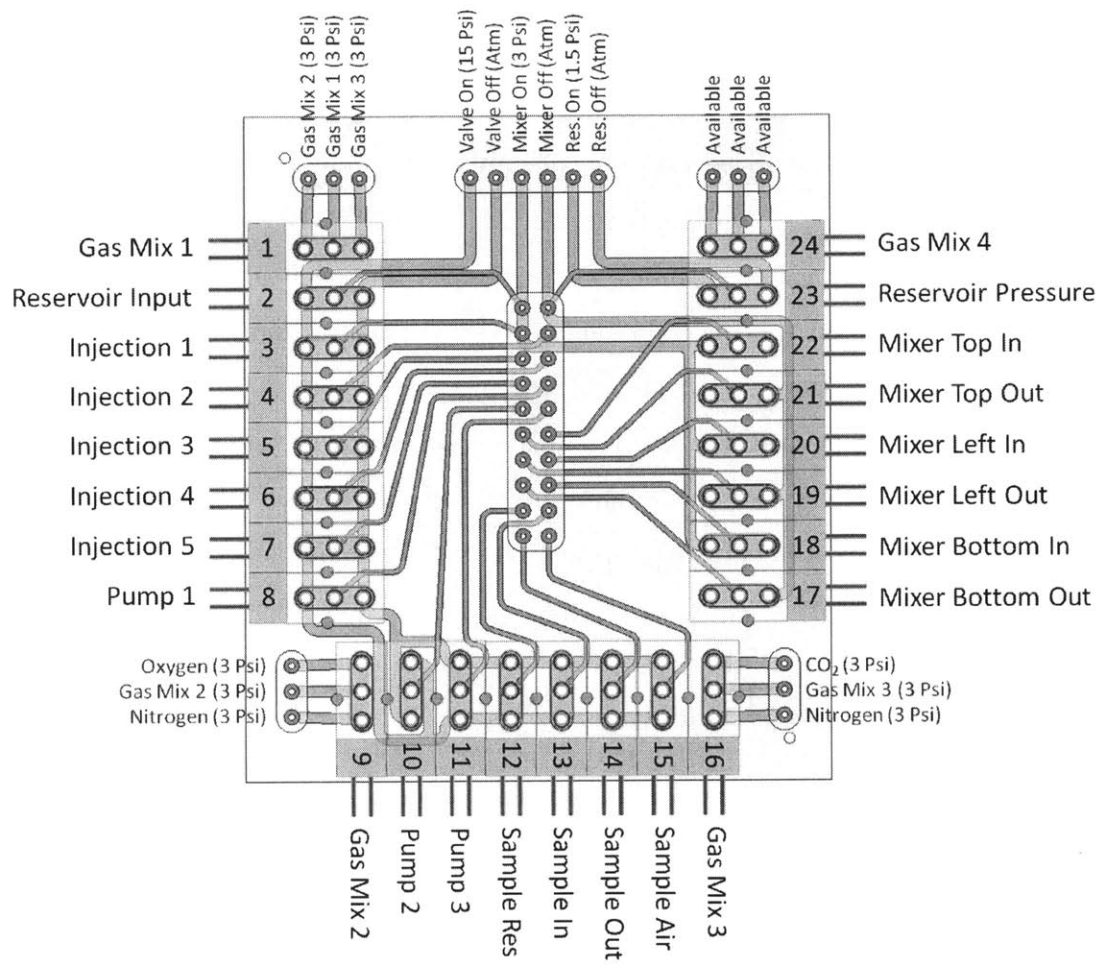


Figure 2-14: Top view of the RECA gas manifold showing gas routings for the valves, mixer, and gas mixing. The manifold consist of 3 layers, the top layer with the solenoid valves and holes drilled directly to the second layer which has the green routes, connecting the output of the valves to the gas connectors in the middle of the manifold, and the bottom layer which connects all the gas lines to the inputs of the solenoid valves, with blue routes.

Valve	Name	NO	NC
1	Gas Mix 1	Gas Mix 2 (3 Psi)	Gas Mix 3 (3Psi)
2	Reservoir Input	Valve On (15 Psi)	Valve Off (Atm)
3	Injection 1	Valve On (15 Psi)	Valve Off (Atm)
4	Injection 2	Valve On (15 Psi)	Valve Off (Atm)
5	Injection 3	Valve On (15 Psi)	Valve Off (Atm)
6	Injection 4	Valve On (15 Psi)	Valve Off (Atm)
7	Injection 5 (Water)	Valve On (15 Psi)	Valve Off (Atm)
8	Pump 1	Valve On (15 Psi)	Valve Off (Atm)

(a) Valves 1-8

Valve	Name	NO	NC
9	Gas Mix 2	Nitrogen (3 Psi)	Oxygen (3 Psi)
10	Pump 2	Valve Off (Atm)	Valve On (15 Psi)
11	Pump 3	Valve On (15 Psi)	Valve Off (Atm)
12	Sample Reservoir	Valve On (15 Psi)	Valve Off (Atm)
13	Sample In	Valve On (15 Psi)	Valve Off (Atm)
14	Sample Out	Valve On (15 Psi)	Valve Off (Atm)
15	Sample Air In	Valve On (15 Psi)	Valve Off (Atm)
16	Gas Mix 3	Nitrogen (3 Psi)	CO ₂ (3 Psi)

(b) Valves 9-16

Valve	Name	NO	NC
17	Mixer Bottom Out	Mixer Off (Atm)	Blocked
18	Mixer Bottom In	Blocked	Mixer On (3 Psi)
19	Mixer Left Out	Mixer Off (Atm)	Blocked
20	Mixer Left In	Blocked	Mixer On (3 Psi)
21	Mixer Top Out	Mixer Off (Atm)	Blocked
22	Mixer Top In	Blocked	Mixer On (3 Psi)
23	Reservoir Pressure	Res. Off (Atm)	Res. On (1.5 Psi)
24	Gas Mix 4	Available	Available

(c) Valves 17-24

Figure 2-15: Table showing the RECA gas manifold connections for the valves according to the valve number. The valve numbers are shown in Figure 2-14. NO stands for Normally Open and NC stands for Normally Closed in the table. The selection of what is NO or NC is based on energy considerations.

sition of the resistance lines with respect to the humidifier and water trap is different for the RECA as compared with the Chemostat micro-bioreactor. The Chemostat micro-bioreactor placed the resistance lines after the humidifier. Moreover, since the mixer now have an input and output line as compared to the Chemostat and PIBA where the mixer in and mixer out share the same line. This is to facilitate flushing of the mixer lines to push all water accumulated into the water trap. Moreover, a sample cooling block will not be necessary for the RECA micro-bioreactor since samples can be collected in 20 seconds as discussed in Section 2.2.3.

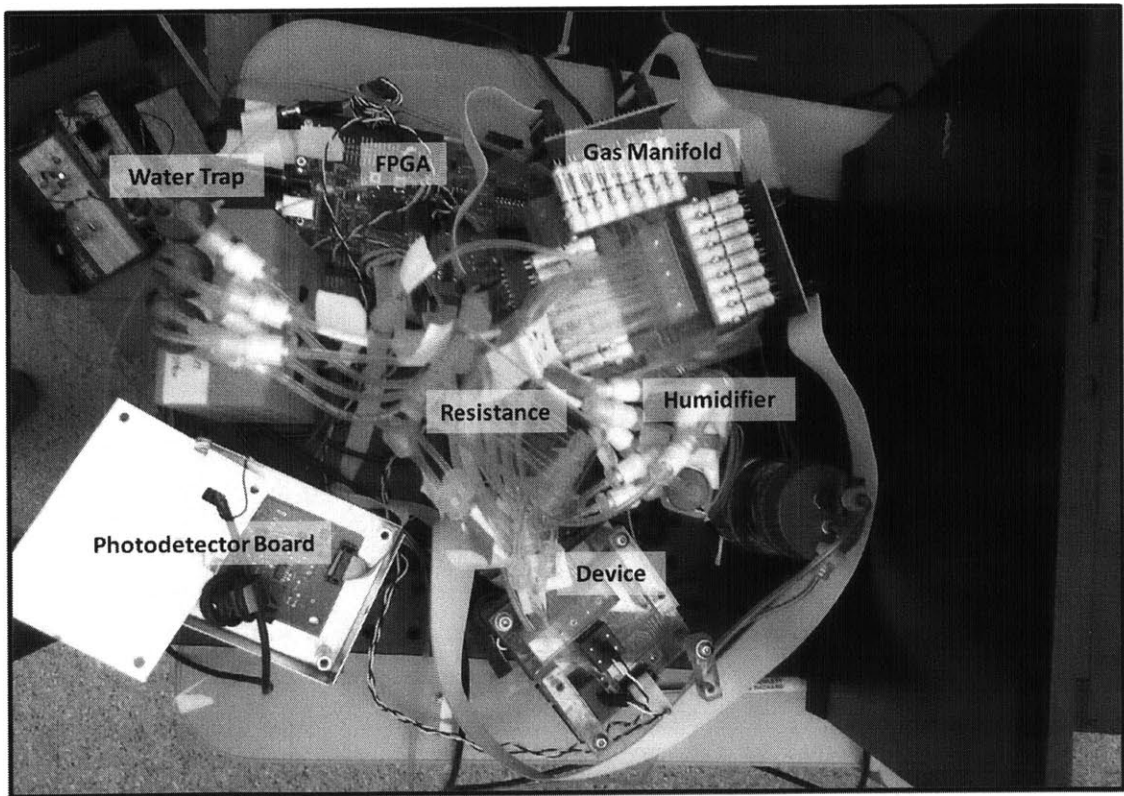


Figure 2-16: A photograph of the RECA setup with the control boards, gas lines, humidifier and micro-bioreactor

2.4 Fabrication of Micro-bioreactor

The details of the fabrication process for the micro-bioreactor are outlined in Kevin Lee's thesis.[40] A summary of the fabrication is presented in this section. The micro-bioreactor is made from polycarbonate sheets. The features of the micro-bioreactor are machined into the sheets using a Minitech Auto-Tool Changer (ATC) Computer Numerical Control (CNC) machine in our lab. With the ATC feature and lab built vacuum chuck for holding polycarbonate pieces, 4 parts can be machined in parallel with minimal operator assistance. The RECA Micro-bioreactor have 3 distinct layers, the bottom layer (liquid), the top layer (gas) and the upper layer (gas routes). The machined polycarbonate pieces tend to have surfaces that are rough and hence to obtain optically clear surfaces, the polycarbonate are vapor polished in Methylene Chloride at 70°C and then baked overnight at 120°C to remove any trace solvent and any stress resulting from solvent reflow. The fabrication process described here is illustrated in Figure 2-19 Steps 1-3.

PDMS membranes with 70 μm thickness is made by spinning PDMS that has been degassed on a fluorosilane treated silicon wafer. The thickness of the PDMS membrane is monitored using an interferometer which measures the distance (time traveled) between peaks from the reflections of light off the interfaces. The setup and fabrication method is described in Harry Lee's thesis[37] on pages 76-77. The spun membrane is then cured in the oven for 4 hours at 70°C.

The bonding between polycarbonate and PDMS is a chemical process developed in our lab.[39], illustrated in Figure 2-18. The bonding molecule is an amine functionalized silane, known as bis-trimethoxy-silyl-propyl-amine (BTMSPA). Polycarbonate has carboxyl groups groups on its surface that forms a covalent bond with the amine end of the BTMSPA molecule. The triisopropoxy group in the silane end reacts with each other to form a crosslinked silane network and also a glass-like bond (Si-O-Si) with PDMS. The crosslinked silane network protects the silane bonds to PDMS from being hydrolytically cleaved by water molecules. Without any surface activation, the bonding process is very slow and have bad coverage (low density) on the surface. In

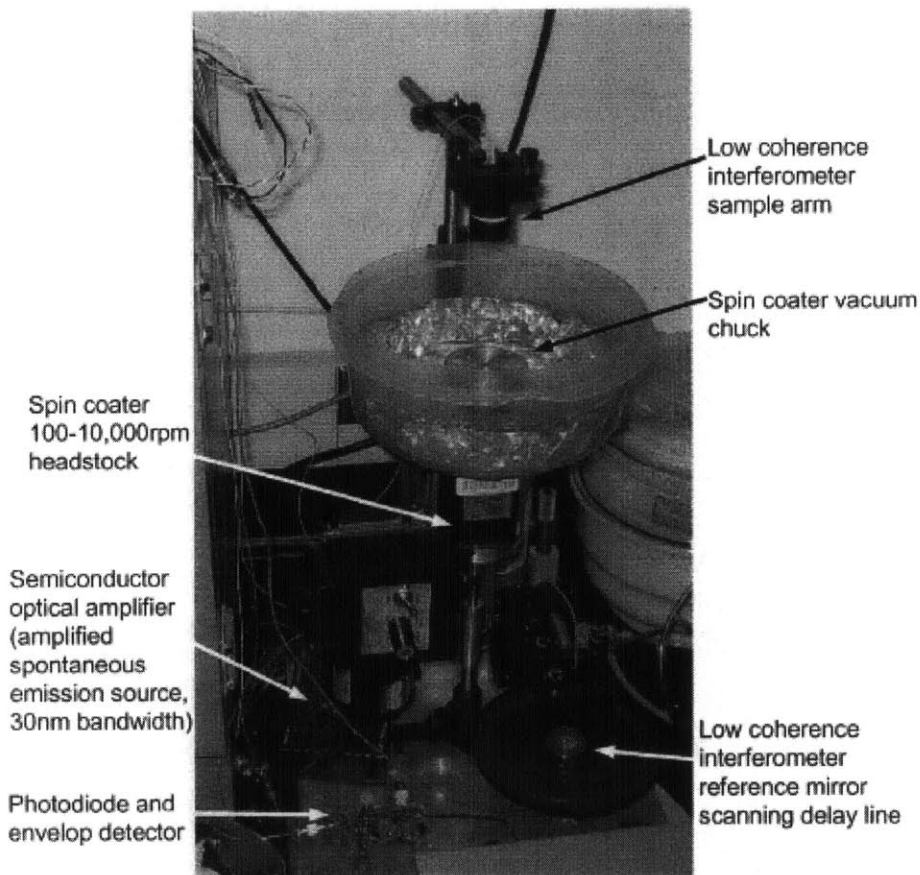


Figure 2-17: This is a photograph showing the spin coater to spin thin ($70\mu\text{m}$) PDMS membranes. The thickness of the PDMS membrane is monitored using an interferometer which measures the distance (time traveled) between peaks from the reflections of light off the interfaces.

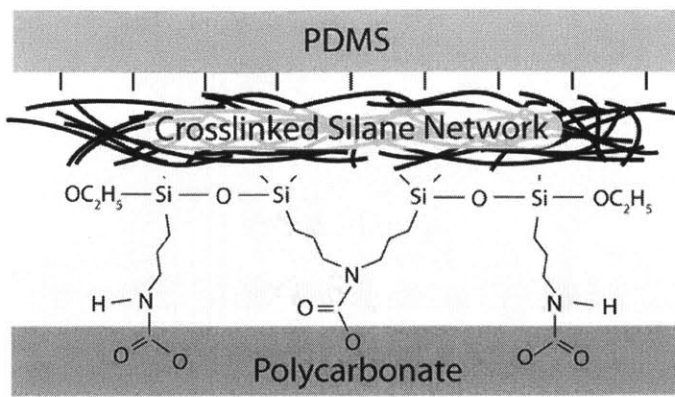


Figure 2-18: Illustration of the bonding process between PDMS and Polycarbonate. An amine functional silane is used as the bonding molecule, forming a glass-like bond (Si-O-Si) with between PDMS and the silane end of the molecule and a covalent bond between the carboxyl groups in polycarbonate and the amine group of the molecule. Since the silane end of the molecule has 3 reactive groups attached to it, a cross-linked silane network is formed. This crosslinked network forms a barrier to prevent hydrolytic cleavage by water molecules.

order to promote a higher density bonding to the surface, the polycarbonate has to be chemically treated prior to the bonding process. The chemical treatment is illustrated in Figure 2-19 Step 4 (top layer). After chemically treating the polycarbonate surface, the silane coating is applied and the covalent bond of the amine group to the carboxyl group is promoted by submerging the silane coated polycarbonate in water at 50°C. The submersion also helps with the crosslinking of the silane molecules. Once the amine is bonded to polycarbonate and the silane crosslinks are formed, the polycarbonate piece is ready to be bonded to the PDMS membrane. The surface of PDMS membrane is plasma activated by a handheld corona discharge generator before applying it to the silane coated polycarbonate surface. This process have to be done very carefully to prevent small air gaps from forming between the PDMS membrane and polycarbonate surface. The bonding process is completed by annealing the PDMS-polycarbonate bonded substrate in an oven at 130°C for 2 hours using an 18 hour slow ramping process. The full bonding process is illustrated in Figure 2-19 Steps 4-9.

After the top layer is bonded, the surface activation and bonding process is re-

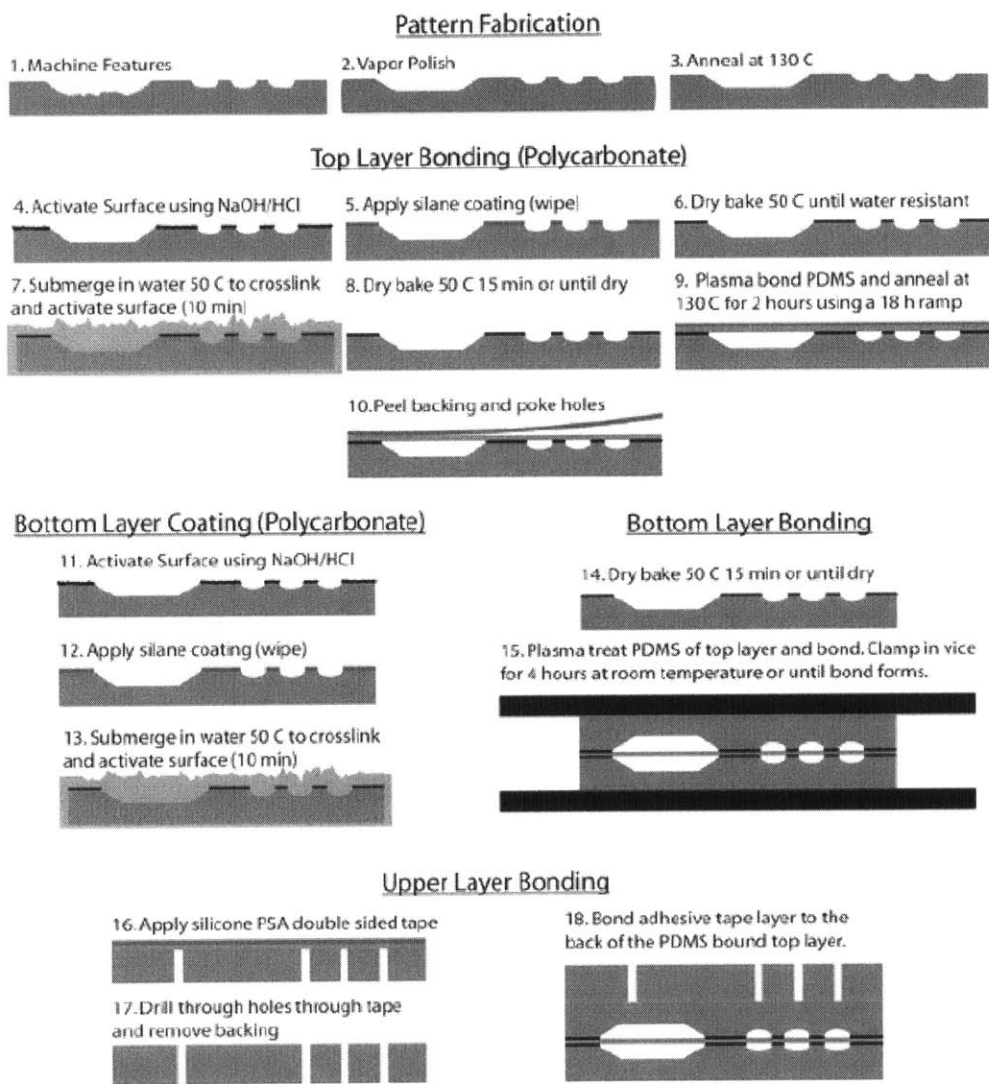


Figure 2-19: An illustration of the fabrication process for the RECA Micro-bioreactor. The details of the fabrication are described in the paragraphs of this section.

peated for the bottom layer. Since the bottom layer contains optical sensors that are temperature sensitive, the anneal process is replaced by clamping at high pressure for 4 hours or longer till a stable bond forms.(Figure 2-19 Steps 11-15) The upper layer, which has gas routes patterned on it to interface the gas connections to the micro-bioreactor, is attached to the chip with a silicone double sided adhesive film, shown in Figure 2-19 Steps 16-18. The manifold (Figure 2-14) and resistance lines (Figure 2-10) are also machined from polycarbonate sheets, vapor polished and then the layers are attached together using silicone double sided adhesive film.

2.5 Conclusions

This chapter delineated the design of the RECA Micro-bioreactor taking into consideration the physiological and physical requirements of CHO cell cultures. The long culture time and salt sensitivity of CHO cells requires the design of an evaporation compensation strategy and humidification of the gas lines. The low shear tolerance of CHO cells requires the integration of resistance lines to reduce the mixing rate. The humidification strategy will also need to be redesigned to prevent water from clogging the resistance lines. Sampling requirements define the working volume of the micro-bioreactor and a new sampling protocol that maintains sterility and produces the sample volume required is also developed in this chapter. The frequent sampling means that the working volume is not kept constant and hence, the evaporation compensation strategy has to be performed with an open loop control and the evaporation rate need to be characterized exactly (results in the next chapter) for the open loop compensation to be successful. The design of the new RECA Micro-bioreactor, the gas manifold and infrastructure supporting the micro-bioreactor is disclosed in this chapter as well. The chapter concludes with a description of the fabrication process of the micro-bioreactor and some parts of the infrastructure, including the manifold and resistance lines. The next chapter will report on the experiments performed to validate the design of the micro-bioreactor, making sure that the experimental values match the design specifications as stated in this chapter.

Chapter 3

Testing and Validation of Micro-bioreactor

3.1 Introduction

Chinese Hamster Ovary (CHO) cells have growth requirements that are different from *Escherichia Coli* that we have cultured in our micro-bioreactors in the past. The requirements for a CHO culture have been summarized in Table 1.1 in Chapter 1. In order to ensure that the newly designed RECA micro-bioreactor has the capability to grow CHO cells, the micro-bioreactor will need to be characterized to ensure it meets the growth needs of CHO cells as described in Section 1.4, namely, the gas transfer rate, k_{La} , for oxygen needs to be around $1\text{-}15 h^{-1}$, for carbon dioxide, $0.1\text{-}6 h^{-1}$, the mixing time needs to be around 20-30 seconds, and the shear stress needs to be below 0.05 Pa to prevent cell death and maintain productivity at a reasonable level as indicated in Figure 2-7. These shear effects on productivity are measured on adherent cells,[33] and the effects of shear on productivity and viability of CHO cells grown in suspension are expected to be lower due to the fact that cells freely suspended in media can rotate or translate to accommodate these shear forces.

Moreover, CHO cells, unlike bacteria cells, require a combination of acidic gas, carbon dioxide(CO_2), and liquid base, Sodium Bicarbonate (NaHCO_3), addition for pH control, to reduce the effects on osmolarity. This new capability requires the in-

tegration and calibration of a new CO₂ sensor in the micro-bioreactor. This chapter begins with the characterization of aeration and mixing with new air resistance lines which slow down the deflection time of the PDMS membrane in order to reduce shear stress on the CHO cells. The mixing time due to the slower mixing rate is also characterized for each air resistance line. Next, the new CO₂ sensors purchased from PreSens GmbH will need to be calibrated and the optimal modulation frequency for the operation of the sensors will need to be determined. Once the CO₂ sensor has been successfully integrated with the micro-bioreactor, the gas transfer rate, k_{La} , of oxygen and carbon dioxide will need to be characterized for the micro-bioreactor. Since this project is still in progress, future characterization that needs to be performed will be summarized in the last section, namely flow rate characterization with fluorescent beads to elucidate the instantaneous shear stress experienced by the cells, the actual evaporation rate of the micro-bioreactor during normal operation and the implementation of the evaporation compensation and the characterization of the sampling accuracy of the new sampling protocol.

3.2 Resistance Line Characterization

The shear sensitivity of CHO cells requires the mixing mechanism in the micro-bioreactor to be slowed down by the addition of air resistance lines leading into the mixer. Please refer back to Section 2.2.4 for more details. A drawing of the two resistance lines, Resistance Line 1 and 2, and the parameters are shown in Figure 2-10. These resistance lines provide a hydrodynamic resistance of 1.27×10^{10} Ns/m⁵ and 1.42×10^{11} Ns/m⁵ respectively. The typical hydrodynamic resistance of the air lines without the resistance lines are of the order of 10^7 Ns/m⁵. These air resistance lines combined with a humidifier and water trap, which forms the hydrodynamic equivalent of a 'capacitor' works together to slow down the deflection of the PDMS membrane. In the first part, the deflection time of the membrane is measured for the three different configuration: (1) no air resistance line, (2) with Resistance Line 1, and (3) with Resistance line 2. Once the deflection time, i.e. the time it takes

Table 3.1: Summary of parameters and validation methods for the RECA Micro-bioreactor

Parameter	Range	Method	Resistance Line	Results	Section
Deflection Time	15-40s	Image analysis of video captured via CCD camera with dye solution to elucidate deflection	No Resistance Resistance 1 Resistance 2	0.4 s 7.5 s 23 s	3.2.1
Mixing Time Constant	20-30s	Image analysis of video captured via CCD camera with concentrated dye solution injected from into the mixing chamber	No Resistance Resistance 1 Resistance 2	0.6 s 8.5 s 38 s	3.2.2
Oxygen k_{La}	$1-15\text{h}^{-1}$	Dynamic gas switching method between medical gas mixture and pure nitrogen gas	No Resistance Resistance 1 Resistance 2	TBD $1-7\text{ h}^{-1}$ TBD	3.4.2
$\text{CO}_2 k_{La}$	$0.1-6\text{h}^{-1}$	Dynamic gas switching method between medical gas mixture and pure nitrogen gas	No Resistance Resistance 1 Resistance 2	TBD $2-5\text{ h}^{-1}$ TBD	3.4.3

to completely pressurize the membrane till the membrane seals the bottom of the chamber, is determined for each configuration, the shear stress through the channels can be estimated. The mixing time then is characterized for different cycle times. A cycle time is defined as the total time that the 3 membranes are actuated. From these measurements, an optimal cycle time is obtained for each configuration.

3.2.1 Deflection Time

The total deflection time of the PDMS membrane in a single mixing chamber for the 3 cases: (1) No Resistance Line, (2) Resistance Line 1 and (3) Resistance Line 2, is measured by recording a video of the deflection using an Opteon CCD Camera. The sequence of images are recorded as a mosaic of pixels (RGGB) and processed in Matlab by applying a demosaic algorithm, white balancing each color by averaging it with the average intensity of each color in a white region of the same image and then normalizing the brightness of each image. A snapshot of every 4 seconds for the experiment with Resistance Line 2 is shown in Figure 3-1. Green food dye is injected into the mixing chamber to elucidate the mixing mechanism. At time $t=0$, the membrane completely seals the bottom of the chamber and the chamber appears white. When the membrane completely inflates with green dye, the chamber appears green and stays green after the deflection as steady state is reached. Averaging the red, green and blue color intensity of a region highlighted by the yellow square in Figure 3-1, we can obtain a graph of average intensity as a function of time for each of the different colors. The results of this measurement is shown in Figure 3-2 for the measurement involving Resistance Line 2. From the graph of the green intensity curve, the total deflection time of the PDMS membrane for Resistance Line 2 is 23 seconds. The same experiment is repeated for the case of No Resistance Line and Resistance Line 1 and a total deflection time of 0.4 seconds and 7.5 seconds are obtained respectively.

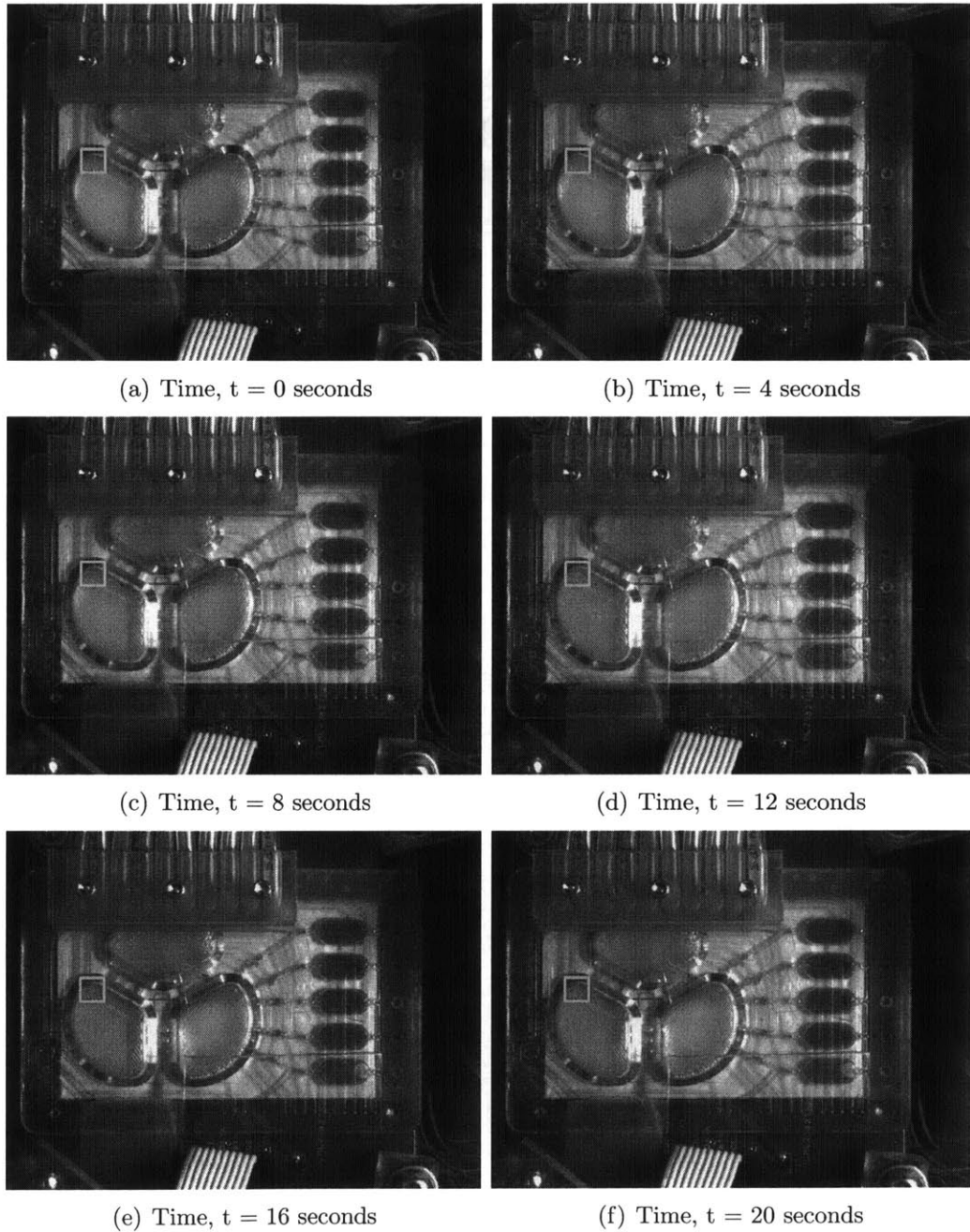


Figure 3-1: Sequence of image showing a complete deflection of the membrane in a single chamber for Resistance Line 2, with the time stated at the bottom of the figure. The yellow box shows the region of pixels in which the image analysis is performed to determine the time taken for the complete deflection of the membrane. The results are shown in Figure 3-2

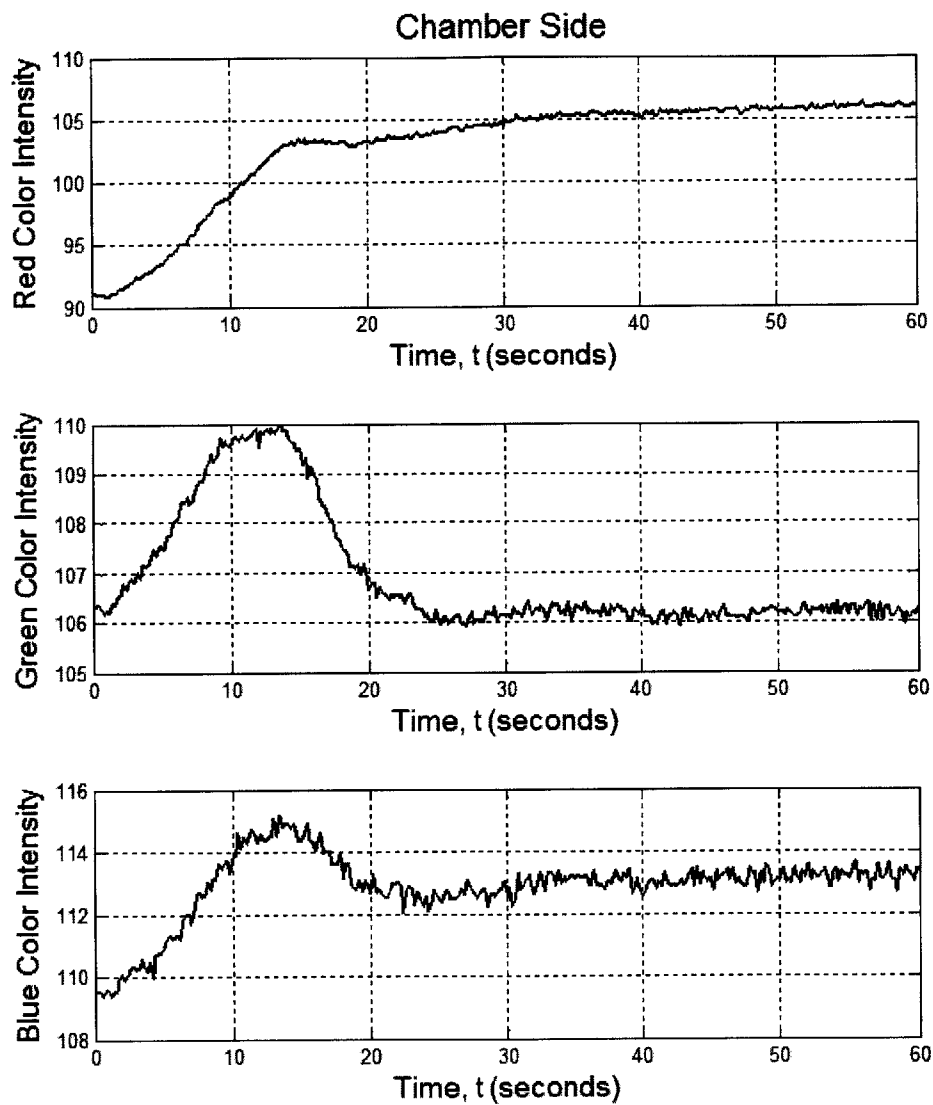
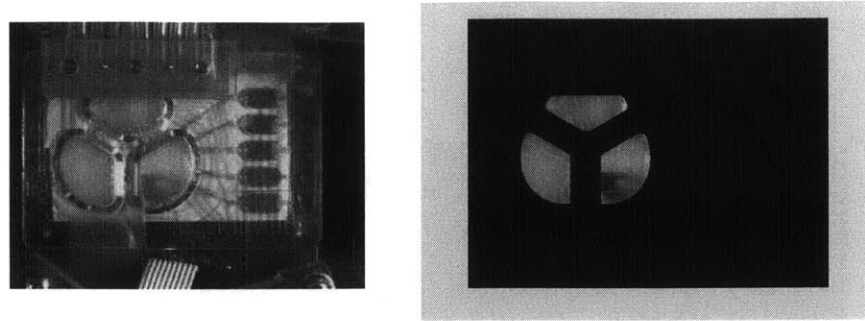
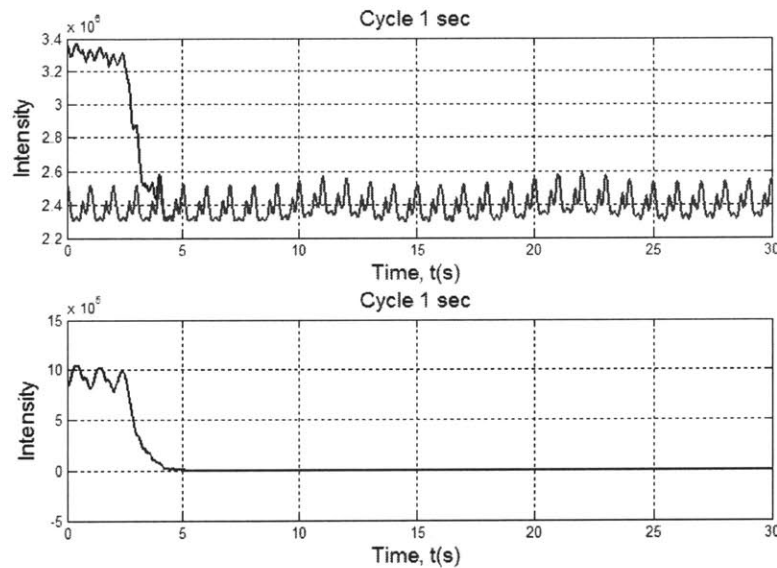


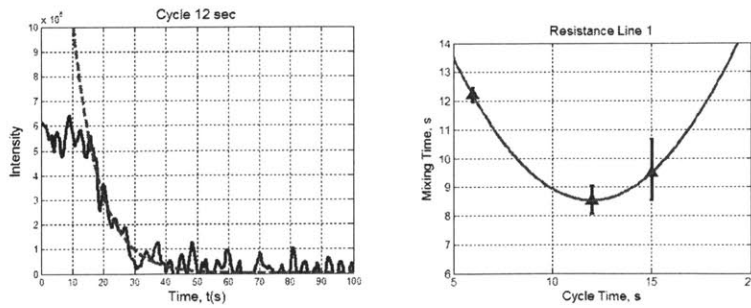
Figure 3-2: Graph showing the intensities of the Red, Green and Blue color as detected by an Opteon CCD camera. The intensity value is a mean value of intensities calculated over a square pixel as depicted in the series of images in 3-1.



(a) Original image before applying mask (b) The red channel intensity image with mask applied to the image showing only the mixer section



(c) (Top) Two graphs showing the original raw data and the oscillations due to the mixer. (Bottom) The oscillations are subtracted from the raw data to give a smooth graph before fitting to an exponential. (This is the result for the case of No Resistance Lines at a cycle time of 1 second)



(d) Exponential fit (dotted line) to total intensity change as a function of time
(e) Mixing time for different cycle times.

Figure 3-3: Mixing time characterization for Resistance Line 1 for different cycle times. Resistance Line 1 have a total deflection time of 7.5 seconds.

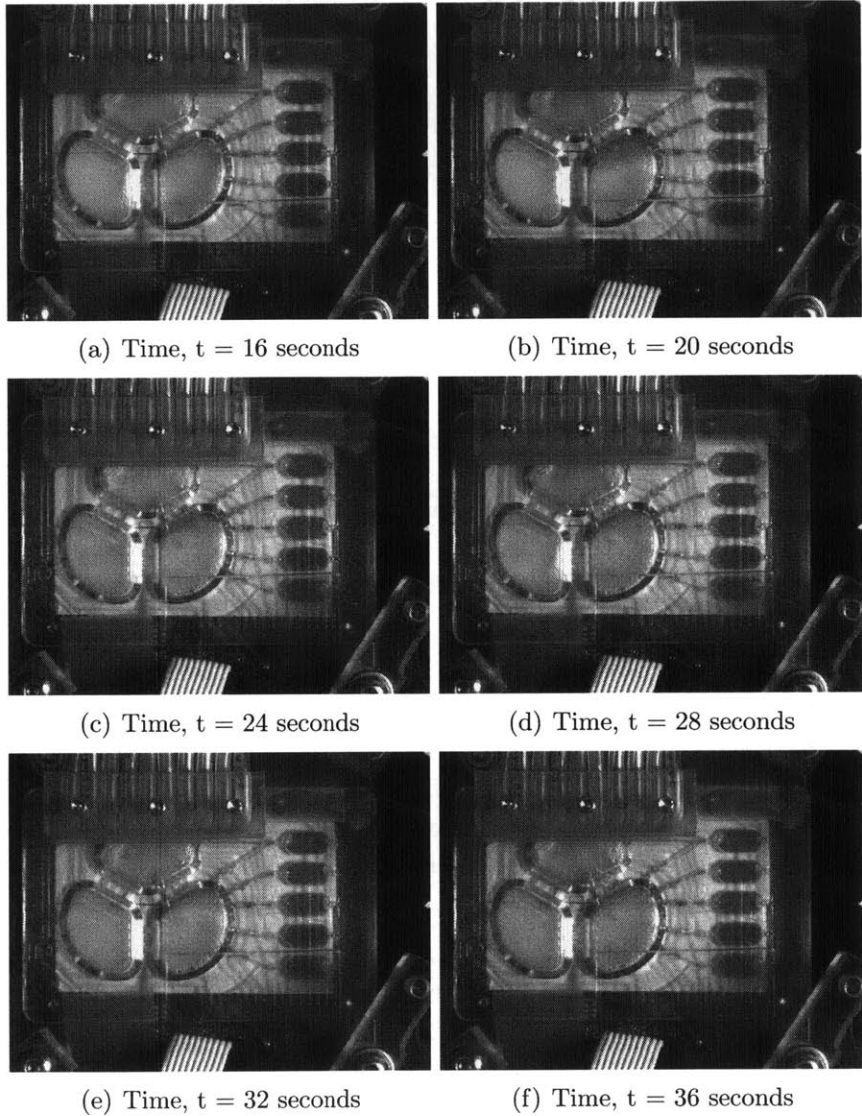


Figure 3-4: Sequence of image showing the mixing of green dye injected in from one of the reservoirs into the mixing chamber. This is the sequence of images for the mixing time measurement with Resistance Line 1 for a cycle time of 12 seconds. The time constant of the mixing time is measured to be 8.5 seconds, measured in Figure 3-3.

Table 3.2: Results from the characterization of the different Air Resistance Lines

Resistance Line	Hydrodynamic Resistance	Deflection Time	Optimal Cycle Time	Mixing Time Constant
No Resistance Lines	$10^7 Ns/m^5$	0.4 s	1 s	0.6 s
Resistance Line 1	$1.27 \times 10^{10} Ns/m^5$	7.5 s	12 s	8.5 s
Resistance Line 2	$1.42 \times 10^{11} Ns/m^5$	23 s	75 s	38 s

3.2.2 Mixing Time

The mixing time is characterized by injecting a green dye from one of the reservoirs and then observing how fast the green dye becomes homogeneous in the mixing chamber measured by the Opteon video camera. A photograph showing a snapshot of the mixing time measurement is shown in Figure 3-3(a). Since homogeneity needs to be achieved in all chambers a mask is applied to the image such that only the mixing chambers gives non-zero intensity in the entire image (Figure 3-3(b)). Moreover, the red channel is used instead of the entire RGB spectrum because the red channel gives the most contrast when a green dye is used, when the chamber is white, all channels gives an intensity that is close to 1 and when it is green, the red channel will have the lowest intensity, since the dye is blueish-green. The masked red channel will be darkest when the chamber is homogeneously green. The sum of the red intensity of all pixels as a function of time is shown in the graph in figure 3-3(c) for Resistance Line 1. The raw data contained oscillations due to the mixing, hence the oscillations are subtracted from the raw graph. The decrease in intensity is fitted to a decaying exponent, indicated by the dotted line.(Figure 3-3(d)) The time constant of the mixing as a function of cycle time, the total time for the actuation of the three membranes, is shown in Figure 3-3(e). In order to illustrate the mixing process, a sequence of 6 images taken at 4 second intervals is shown in Figure 3-4 for Resistance Line 1 at a cycle time of 12 seconds. A full summary of the characterization of the different air resistance lines is tabulated in Table 3.2.

3.3 Carbon Dioxide Sensor Calibration

3.3.1 Carbon Dioxide Sensor

The carbon dioxide sensors (pCO_2) used in our micro-bioreactor are the CO_2 sensor spots from PreSens GmbH. These sensors have gas-permeable membranes in which a short lifetime pH sensitive luminescence dye, hydroxypyrenetrisulfonic acid (HPTS), is immobilized together with a buffer and an inert reference luminescence dye with a long lifetime. Humidified CO_2 gas permeating into the membrane changes the internal pH of the buffer and the luminescence of the HPTS. The two luminophores have overlapping excitation and emission spectra so that they can be excited with the same light source and detected with the same photodetector. The excitation source is modulated at a frequency, f_{mod} , that is compatible with the long lifetime fluorophore. Fluorophores with different lifetimes, τ , will lag behind the modulated source with a phase lag of ϕ , given by Equation 3.1.[36]

$$\tan \phi = 2\pi f_{mod} \tau \quad (3.1)$$

The reference fluorophore will have a constant phase lag given by ϕ_{ref} . Since the HPTS has a very short lifetime, the phase lag will be approximately zero, $\phi_{ind} \sim 0$. The real and imaginary part of the resultant emitted fluorescence from the reference and indicator dyes, with amplitude, A_m , and phase, ϕ_m , are listed in the following equations.[29]

$$A_m \cos \phi_m = A_{ref} \cos \phi_{ref} + A_{ind} \quad (3.2)$$

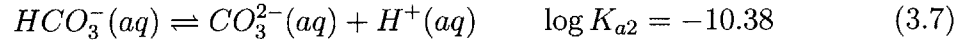
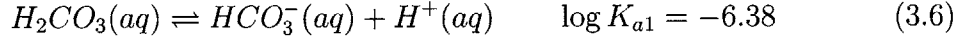
$$A_m \sin \phi_m = A_{ref} \sin \phi_{ref} + A_{ind} \quad (3.3)$$

These equations simplify to give a linear relationship between the cotangent of the phase lag of the resultant fluorescence, $\cot \phi_m$, and the ratio between the amplitudes of the indicator and reference fluorescence, A_{ind}/A_{ref} , since both $\cot \phi_{ref}$ and $\sin \phi_{ref}$

are constants.[10]

$$\cot \phi_m = \cot \phi_{ref} + \left(\frac{1}{\sin \phi_{ref}} \right) \frac{A_{ind}}{A_{ref}} \quad (3.4)$$

An increase in CO₂ will result in a proportional increase of protons in the buffer region according to the three chemical equations below, the equilibrium constants are given at 20°C.



The fluorescence of the indicator dye is due to the presence of unprotonated HPTS and hence an increase in pCO₂ will result in a reduction of the fluorescence intensity of the indicator dye. The equation that relates the ratio between the amplitudes, A_{ind}/A_{ref} , to the pCO₂ is shown in Equation 3.8, where K is derived from the pK_a of the HPTS and the pH of the buffer.[53]

$$\frac{A_{ind}}{A_{ref}} = \frac{1}{1 + KpCO_2} \quad (3.8)$$

We can then relate the resultant phase lag, ϕ_m , to the partial pressure of carbon dioxide in the liquid, pCO₂, with ϕ_0 , being the phase lag at zero pCO₂ and ϕ_{max} , being the phase lag for the pCO₂ at saturation.[10]

$$\cot \phi_m = \cot \phi_{max} + \frac{\cot \phi_0 - \cot \phi_{max}}{1 + KpCO_2} \quad (3.9)$$

Firstly. the optimal modulation frequency, f_{mod} , of the excitation light at 430nm will have to be determined. The emission of the sensor will be detected at a wavelength of 517nm. Since the indicator has a decay time in the ns range and the reference have

a decay time in the μs range, the f_{mod} will be swept between 500Hz and 30MHz to find the optimum frequency. CO₂-free Sodium Hydroxide (NaOH) solution will be prepared by dissolution of NaOH pellets in doubly distilled water after boiling and purging with nitrogen (N₂) gas.[54] For the high pCO₂ concentration solution, a 1 M NaHCO₃ solution will be used. Measurement of the phase lag will be performed for the 1 M NaHCO₃ solution and then subtracted with CO₂ free solution for the entire frequency range. The frequency at which the difference in phases, $\Delta\phi$, is the largest will be chosen as the optimal modulation frequency, f_{mod} . If we assume the response time of the reference dye to be 50 μs and that of the indicator to be 50ns, then assuming that at zero point, $A_{ind} \sim A_{ref}$, and at saturation, $A_{ind} \ll A_{ref}$, we can theoretically model the phase difference, $\Delta\phi$ as a function of the modulation frequency, f_{mod} , with Equation 3.10. The results are plotted in Figure 3-5.

$$\Delta\phi_m = \phi_{ref}(f_{mod}) - \cot^{-1} \left(\frac{\cos \phi_{ref}(f_{mod}) + \cos \phi_{ind}(f_{mod})}{\sin \phi_{ref}(f_{mod}) + \sin \phi_{ind}(f_{mod})} \right) \quad (3.10)$$

After obtaining the optimal modulation frequency, the sensors will be calibrated at that frequency with solutions with different pCO₂ concentrations at 37°C, the operating temperature. For the calibration we will use the CO₂ free solution as described earlier and dilutions of 1 M NaHCO₃ solutions. To calculate the pCO₂ in each of the standard solutions, we will need to use eqs. (3.12) to (3.14). The equilibrium constants listed in the equations are valid for a temperature of 20°C, in order to translate the equilibrium constants for 37°C, we will need to find the Gibbs free energy of the reaction according to the following equation.

$$\Delta G_0 = -RT \ln K_{eq} \quad (3.11)$$

From the equation, we can see that $T_1 \ln K_{eq}(T_1) = T_2 \ln K_{eq}(T_2)$. Hence, we will rewrite the three chemical equilibrium equations with the new equilibrium constants at 37°C.



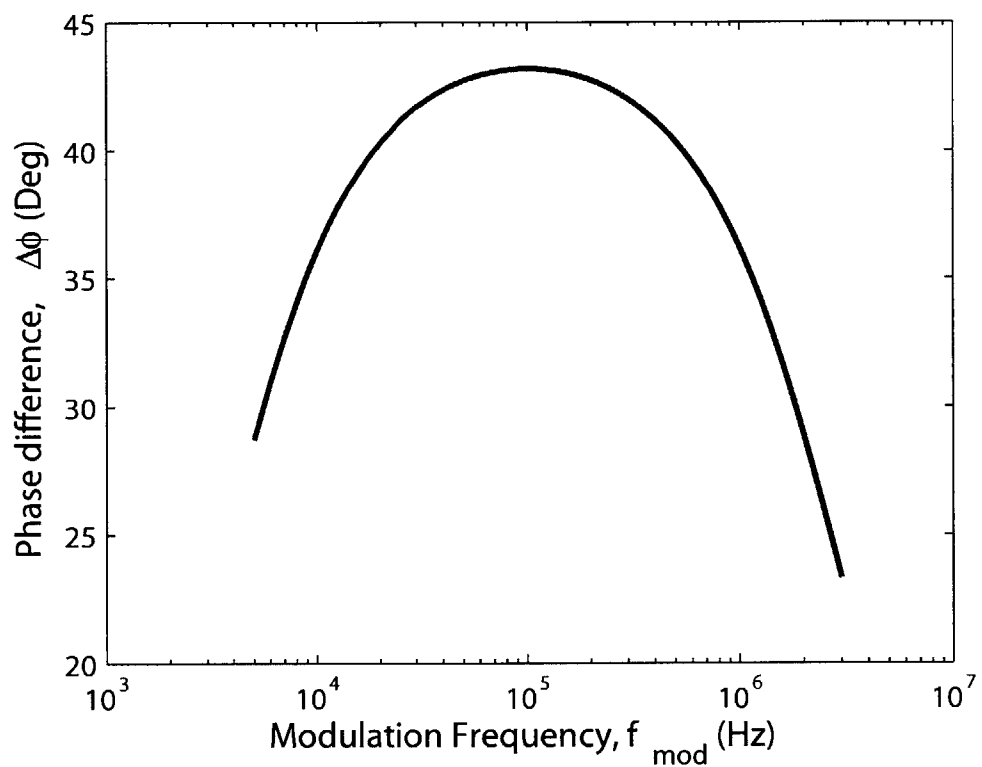
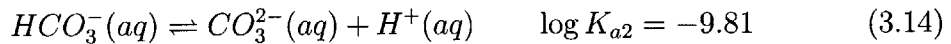
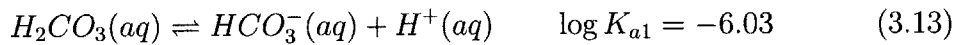


Figure 3-5: Theoretical plot of the estimated optimal modulation frequency

Table 3.3: Calculated dissolved carbon dioxide concentrations from NaHCO_3 solutions at 25°C from measured pH values and known concentration of NaHCO_3 .

NaHCO_3 (M)	pH	H_2CO_3^* (M)	pCO_2 (atm)
0.001	7.51	6.89×10^{-5}	0.0018
0.003	8.02	6.69×10^{-5}	0.0017
0.01	8.35	1.05×10^{-4}	0.0027
0.03	8.34	3.22×10^{-4}	0.0083
0.1	8.38	9.80×10^{-4}	0.0252
0.3	8.31	3.50×10^{-3}	0.0888



From these equations, we can calculate pCO_2 using the method outlined in this reference.[54] The partial pressures of carbon dioxide, pCO_2 , are listed for different concentrations of NaHCO_3 solutions in Table 3.3. The solutions have to be mixed fresh and stored in a sealed vial before and during the measurement, the vial have to remain sealed and stirred to decrease the response time of the sensor. The sensor will be calibrated with the CO_2 -free NaOH standard solutions and the rest of the NaHCO_3 solutions in increasing concentration with an LED modulated at the optimal frequency measured in the previous experiment. The calibration graph will be fitted to Equation 3.9 and the values of the constants in the equation, ϕ_0 will be obtained from the CO_2 -free measurement and ϕ_{max} and K , will be obtained from the best fit parameters.

3.3.2 Optimal Modulation Frequency

The CO_2 sensor is illuminated by an LED (430nm) modulated at frequencies between 1kHz and 100kHz to obtain the optimal modulation frequency. Since there is an electronic low pass filter that cuts off the frequency at 100kHz in the circuit, the highest modulation frequency that is possible for the system is 93kHz. The signal

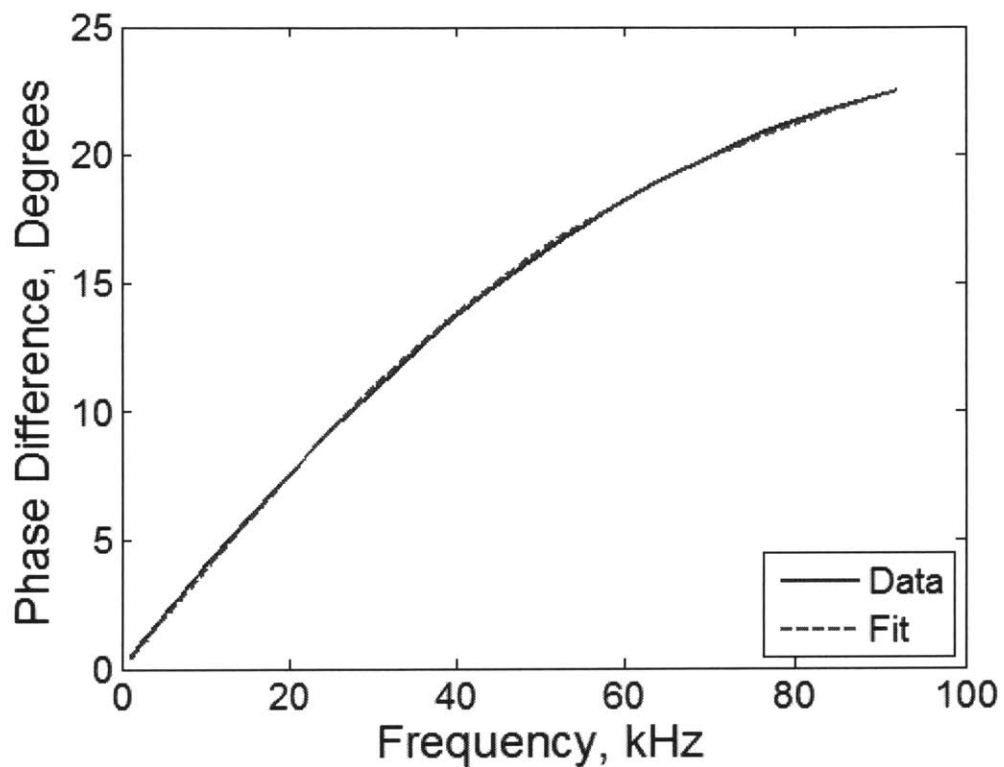


Figure 3-6: Experimentally measured phase difference between 1M NaHCO₃ and 1mM NaHCO₃ solutions for a range of modulation frequency. The data is fitted to Equation 3.4 and the lifetime of the two dyes are obtained through the fit, with the reference dye having a lifetime of 2.5 μ s and the indicator dye having a lifetime of 312 ns.

obtained from the photodiode is then compared with the reference signal and the phase lag between the two signals are obtained. This measurement is performed on 1mM NaHCO₃ solution and then repeated with 1M NaHCO₃ solution. The phase difference between the two measurements are then plotted as a function of frequency and shown in Figure 3-6. The data obtained is fitted to the Equation 3.4 to obtain the lifetimes of the reference and indicator dyes. From the fitting, the lifetime of the reference dye is measured to be 2.5 μ s, which is close to the literature value of 5 μ s [1], and the lifetime of the indicator dye is measured to be 312 ns, which is similar to the literature value of 173-293 ns [48]. From the measurements, the optimal modulation frequency that gives the highest sensitivity is the highest modulation frequency of the electronic system, which is around 93kHz. It is important to note that the modulation frequencies chosen for this sweep is selected to be prime numbers to avoid noise in the measurements due to harmonics of electrical noise sources in the background.

3.3.3 Bicarbonate Calibration

The CO₂ sensor is calibrated with Sodium Bicarbonate (NaHCO₃) solution of different concentration to represent solutions with different levels of dissolved CO₂ as listed in Table 3.3. The solutions are mixed fresh and then sealed. Just before the measurement, the pH of the solution is measured to determine the concentration of dissolved CO₂. Once the solution is injected into the micro-bioreactor with the CO₂ sensor, the phase measurement is allowed to reach steady state. The results are plotted in Figure 3-7. The data is fitted to Equation 3.9 with the value of $K = 3.43 \times 10^3$.[53] From the graph, we can see that the sensor is more sensitive to low dissolved CO₂ gas concentrations. The measured maximum phase lag, ϕ_{max} , is 147 ° and phase lag at zero dissolved CO₂ concentration, ϕ_o , is 149 °.

3.4 Gas Transfer Rate (k_{La})

In order for the micro-bioreactor to have the same aeration rate as a large scale bioreactor, the gas transfer rate (k_{La}) of the new RECA micro-bioreactor will need

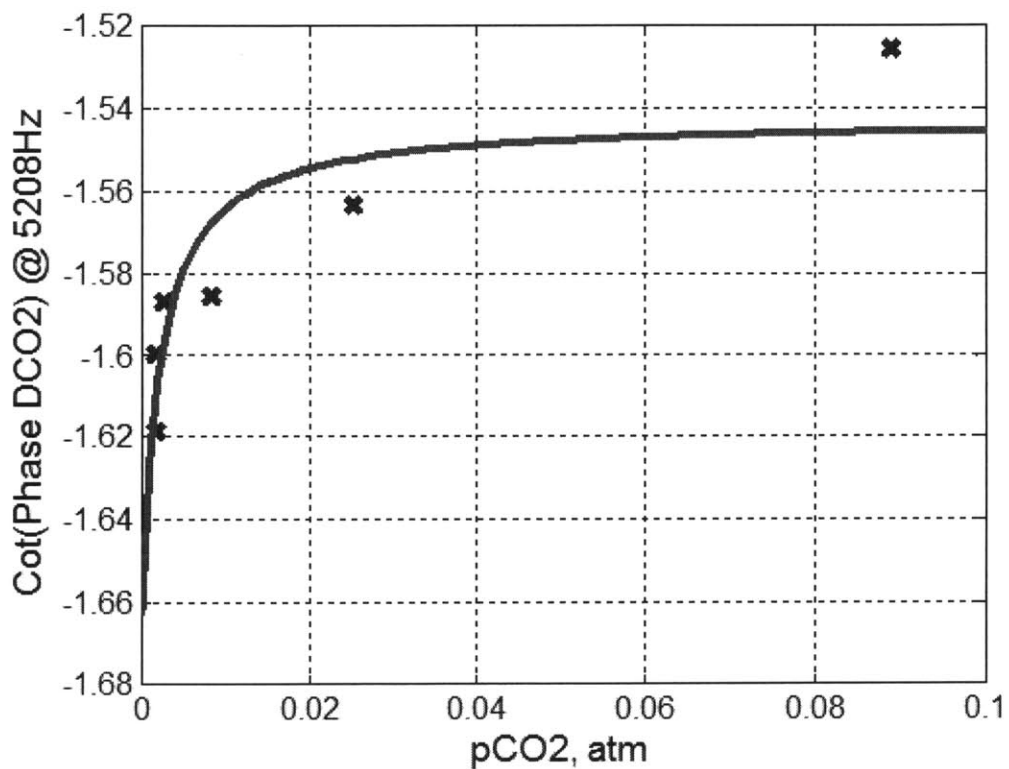


Figure 3-7: The calibration of the CO₂ sensor with Bicarbonate(NaHCO₃) solution of varying concentration. The dissolved CO₂ gas is calculated after measuring the pH immediately after mixing. The resultant dissolved CO₂ concentration is shown in Table 3.3. The data is fitted to Equation 3.9

to be characterized both for oxygen and carbon dioxide. This characterization can only be performed after the optimal mixing time is determined for each resistance line because the gas transfer rate, k_{La} , a time constant, is related to both the diffusivity of the gas species through the PDMS membrane and the liquid as well as the mixing rate in the liquid. The higher the diffusivity and mixing rate, the faster the transport of gas species to the bottom of the chamber where the sensors are located. A sufficient gas transfer rate of oxygen is necessary to ensure that the cells have sufficient oxygen and do not enter into a hypoxic state. The gas transfer rate of carbon dioxide is has to be at the right level to ensure that pH control is similar to large scale bioreactors.

3.4.1 Theoretical Estimates

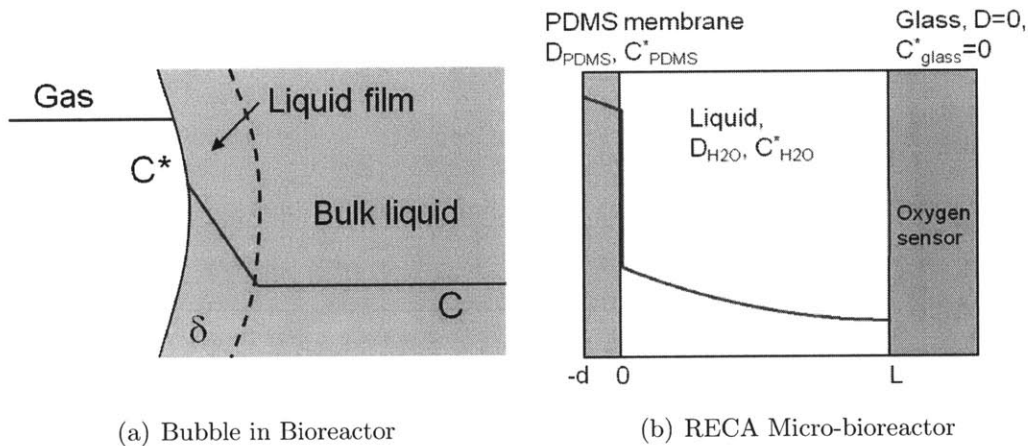


Figure 3-8: A model for the gas transfer of bench top bioreactors is shown in (a). The image shows the diffusion of gas from sparged bubbles into the bulk of the liquid through a liquid film of thickness δ . For the RECA aeration system shown in (b), the gas chamber is separated from the bulk liquid by a thin PDMS membrane, before reaching the oxygen sensor at the bottom of the chamber. There are two phenomena that dictates the k_{La} of gas in this geometry. One is the diffusion of gas through the $70\mu\text{m}$ PDMS membrane. The other is the diffusion of gas in the liquid coupled with the mixing mechanism. The resultant k_{La} will be a parallel combination of both phenomena.

In Harry Lee's thesis[37], he extended the 0-D engineering equation (Equation 3.15) for the gas transfer rate of oxygen for bubbles in bioreactors

$$\frac{dC}{dt} = k_{La}(C^* - C) - OUR \quad (3.15)$$

where C^* and C refers to the saturated and actual concentration of gas in the medium, k_{La} is the gas transfer rate through the bubble and OUR is the Oxygen Uptake Rate by the cells in the medium, to a 1-D diffusion equation (Equation 3.16) for the micro-bioreactor geometry

$$\frac{\partial C}{\partial t} = \frac{\partial}{\partial z} \left(D(z) \frac{\partial C}{\partial z} \right) - OUR \quad (3.16)$$

where $D(z)$ is the diffusivity of the gas species in PDMS, D_{PDMS} , for $-d < z < 0$ and in water, D_{H2O} , for $0 < z < L$. The model for the gas transfer is shown in Figure 3-8 for both the bench top bioreactor and micro-bioreactor. The k_{La} for the bench top bioreactor is dependent on the liquid film thickness of the bubble, δ , the total surface area of the bubbles retained in the medium, A , and the volume of the medium, V , resulting in the following equation:

$$\frac{dC}{dt} = \frac{AD_{H2O}}{V\delta}(C^* - C) - OUR \quad (3.17)$$

For the case of the micro-bioreactor, the solution is not as simple and an analytical solution can only be obtained for two limiting cases, 1. When the diffusion through water is dominant ($L \gg d$)

$$k_{LaH2O} \approx \left(\frac{\pi}{2}\right)^2 \frac{D_{H2O}}{L^2} \quad (3.18)$$

and 2. When there is instantaneous mixing, i.e. the diffusion through PDMS is dominant

$$k_{LaPDMS} \approx \frac{(D_{PDMS}/K)}{Ld} \quad (3.19)$$

where K = partition coefficient, the ratio of saturated gas concentrations in water, C_{H2O}^* , to the saturated gas concentration in PDMS, C_{PDMS}^* . The actual k_{La} is a parallel sum of these two limiting cases.

Table 3.4: Physical Parameters used in the calculation of the gas transfer rates, k_{La} , for oxygen and CO_2 .

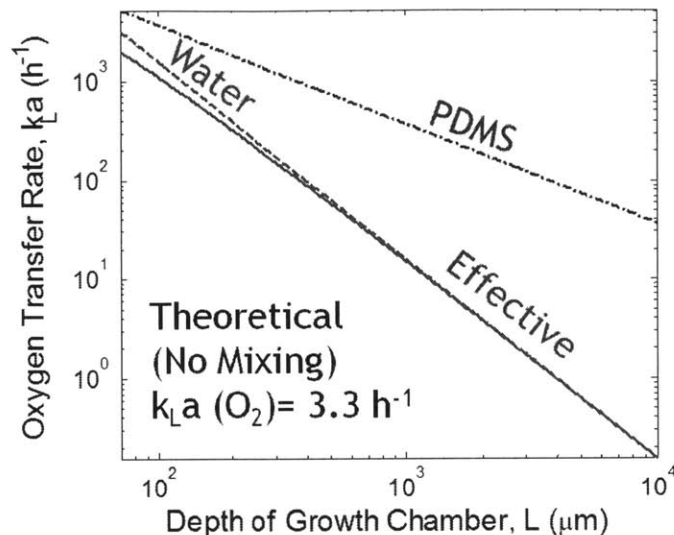
Parameters	Oxygen (O_2)	Carbon Dioxide (CO_2)
D_{PDMS}	$2.15 \times 10^{-9} \text{ m}^2/\text{s}$ [45]	$7.08 \times 10^{-10} \text{ m}^2/\text{s}$ [73]
D_{H2O}	$2.19 \times 10^{-9} \text{ m}^2/\text{s}$ [70]	$1.88 \times 10^{-9} \text{ m}^2/\text{s}$ [50]
C_{PDMS}^*	$0.9 \mu\text{M}(0.21 \text{ atm})$ [37]	$1.1 \mu\text{M}(0.05 \text{ atm})$ [73]
C_{H2O}^*	$0.27 \mu\text{M}(0.21 \text{ atm})$ [18]	$1.74 \mu\text{M}(0.05 \text{ atm})$ [17]
K	0.3	1.6

$$k_{La} = \frac{1}{\frac{1}{k_{LaH2O}} + \frac{1}{k_{LaPDMS}}} \quad (3.20)$$

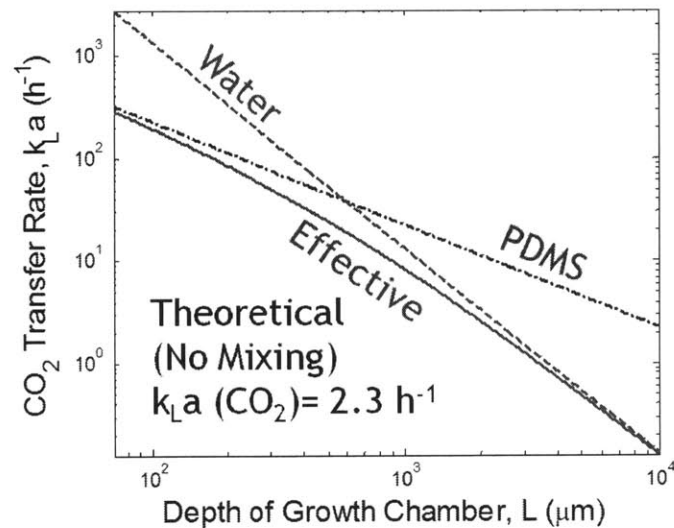
For the RECA Micro-bioreactor, the Oxygen (O_2) and Carbon Dioxide (CO_2) gas transfer rates, k_{La} , are calculated using physical parameters obtained from literature, which are summarized in Table 3.4, for different depths of the micro-bioreactor, L . With a depth of 0.085 inches, an effective k_{La} of 3.3 h^{-1} for oxygen and 2.3 h^{-1} for carbon dioxide. In this model, it is assumed that the mixing has no effect on the diffusivity of the gas molecules through the liquid and that the chamber, made of polycarbonate, is impermeable to gas. However, polycarbonate is permeable to gas and hence, this model may not accurately model the exact phenomena but provides us with a rough estimate of the expected gas transfer rate. Besides, the presence of mixing is expected to increase the k_{La} , though not a significant effect is anticipated for the RECA micro-bioreactor since it is designed to exert a low shear stress on the cells resulting in a slow mixing rate.

3.4.2 Oxygen

The experiment is performed using the dynamic gas method since for coalescent liquids, the steady state and dynamic gassing values of k_{La} are comparable.[44] In our experiments, the gas in the head space of the mixer is switched from a medical gas mixture (21% O_2 , 5% CO_2 and balance N_2) to pure nitrogen (100% N_2). The differential equation that describes the gas transfer relationship of oxygen is given by the equation below, where C represents the dissolved oxygen concentration in the



(a) Oxygen Transfer Rate through $70\mu\text{m}$ PDMS



(b) Carbon Dioxide (CO_2) Transfer Rate through $70\mu\text{m}$ PDMS

Figure 3-9: Theoretical plot of the gas transfer rate ($k_L a$) of (a) Oxygen and (b) Carbon Dioxide (CO_2) as a function of the depth of the chamber. The effective $k_L a$ is a parallel sum of both the individual $k_L a$ for the diffusion of the gas species through PDMS and Water. In this model, it is assumed that the mixing rate is slow enough that it does not affect the diffusion rate of the gas molecules through the liquid. The values of the expected $k_L a$ are shown as insets in the figures. This model also assumes that there is no diffusion of gas through the polycarbonate walls.

liquid, C^* is the saturation concentration of oxygen in the liquid and OUR refers to the oxygen uptake rate in the liquid, e.g. the oxygen uptake rate of biological cells or a molecule that absorbs oxygen in the liquid.

$$\frac{dC}{dt} = k_{La}(C^* - C) - OUR \quad (3.21)$$

Solving the differential equation above, an exponential relationship is obtained for the concentration of dissolved oxygen, C , as a function of time with $OUR = 0$.

$$C(t) = C^*(1 - e^{-k_{La}t}) \quad (3.22)$$

The results measured by the oxygen sensor utilizing the dynamic gassing method is shown in Figure 3-10 for Resistance Line 1 at an optimal mixing cycle time of 12 seconds. From the measurement, the k_{La} obtained when oxygen is diffusing from the head space through the membrane into the liquid, i.e. when medical gas mixture is in the head space, is $6.9 \pm 0.1 h^{-1}$. When the gas is switched to pure nitrogen, oxygen is now being purged from the system by low concentration of oxygen in the head space, and the gas transfer rate of purging is measured to be $1.37 \pm 0.04 h^{-1}$. As a comparison, the gas transfer rate for oxygen for a 15,000L bioreactor is $2\text{-}3 h^{-1}$ and $15 h^{-1}$ for a 2L bioreactor.

3.4.3 Carbon Dioxide

In the same experiments, the CO_2 gas transfer rate is also measured since the medical gas mixture contained CO_2 gas as well. The results are shown in Figure 3-11 for Resistance Line 1. From the an exponential fit to the data, the gas transfer rate, k_{La} of CO_2 from the medical gas mixture is $2.14 \pm 0.07 h^{-1}$ and the gas transfer rate from the liquid into the pure nitrogen gas head space is $4.93 \pm 0.04 h^{-1}$. As a comparison, the gas transfer rate of CO_2 , k_{La} , for a 15,000L bioreactor is $0.2\text{-}0.4 h^{-1}$ and for a 2L bioreactor is $5\text{-}6 h^{-1}$.

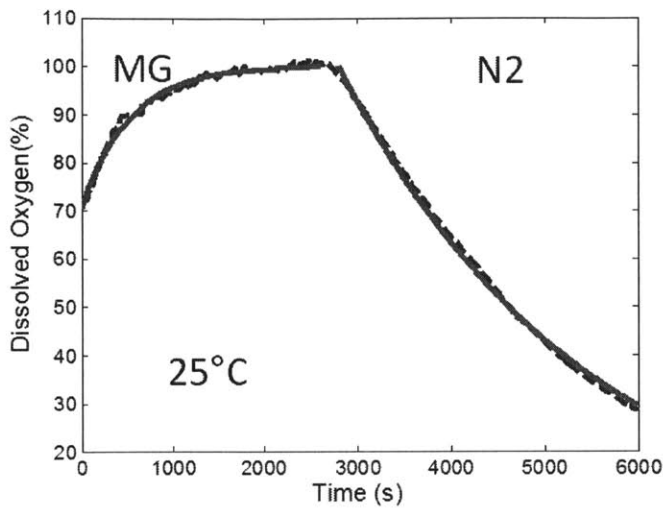


Figure 3-10: The gas transfer rate, k_{La} measurement for oxygen performed at room temperature (25°C) measured using the dynamic gassing method with Resistance Line 1. Two exponential graphs are fitted to the data to obtain the time constant which is the inverse of k_{La} . The k_{La} obtained using medical gas mixture is $6.9 \pm 0.1 \text{ h}^{-1}$ and pure nitrogen is $1.37 \pm 0.04 \text{ h}^{-1}$.

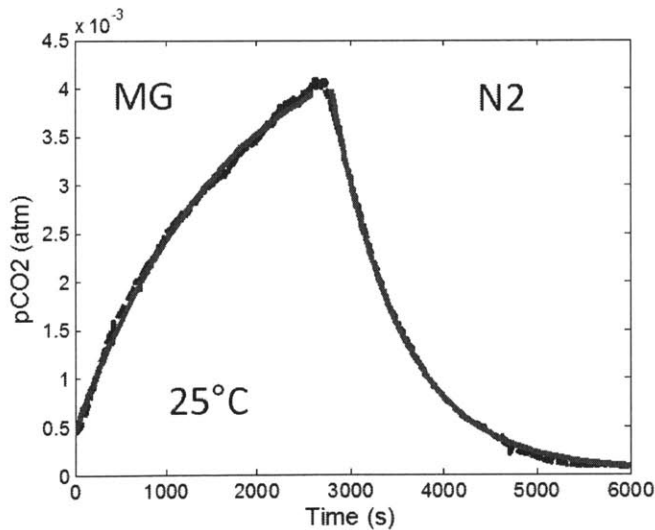
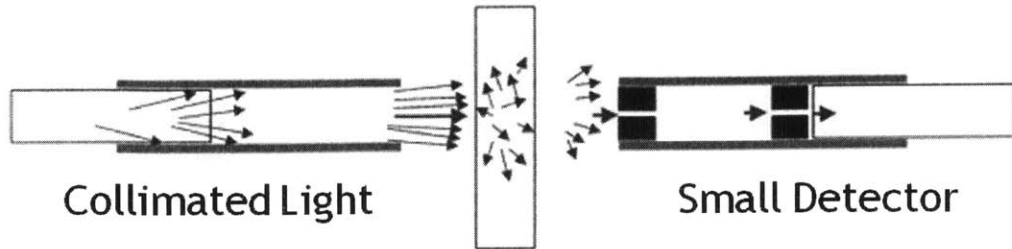
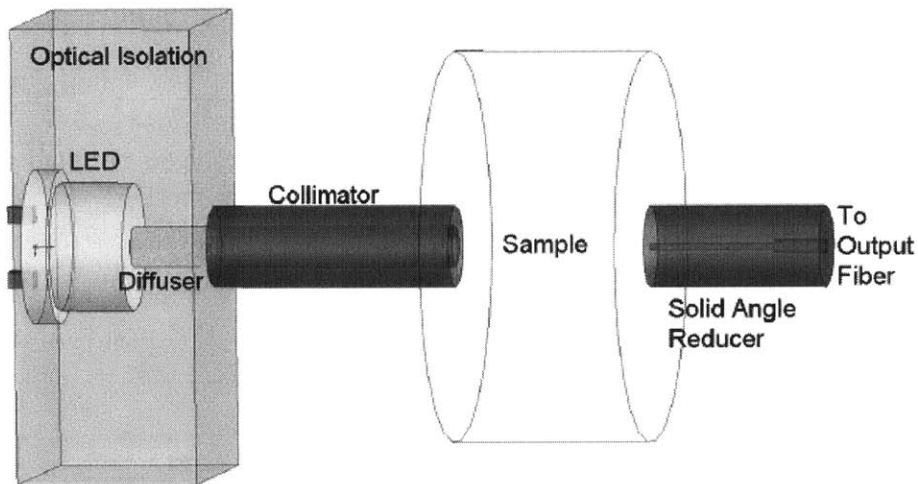


Figure 3-11: The gas transfer rate, k_{La} measurement for carbon dioxide performed at room temperature (25°C) measured using the dynamic gassing method with Resistance Line 1. Two exponential graphs are fitted to the data to obtain the time constant which is the inverse of k_{La} . The k_{La} obtained using medical gas mixture is $2.14 \pm 0.07 \text{ h}^{-1}$ and pure nitrogen is $4.93 \pm 0.04 \text{ h}^{-1}$.

3.5 Optical Density



(a) Schematic of Optical Density Apparatus



(b) LED-fiber optical density sensor

Figure 3-12: (a) The Optical Density (OD) sensor is a turbidity probe which measures total cell density in the culture due to the scattering of light by the cells. The incident light is collimated and the transmitted light intensity is measured using a small detector to limit the angle of incidence and detection so that only unscattered light is transmitted to the detector. (b) The OD sensor using LED as light source, with a diffuser to make the intensity more uniform and a collimator. The detector consists of a solid angle reducer coupled to a fiber that ends at a photodetector. The OD sensor has the same design as the OD sensor in Kevin Lee's thesis.[40]

Turbidity or Optical Density (OD) sensors are utilized to track cell culture growth in real time in the RECA Micro-bioreactor. As shown in Figure 3-12, the OD sensor sends a collimated light into the growth chamber and the cloudiness of the cell culture scatters the incident light. The unscattered transmitted light is then collected at the

bottom of the chamber. The density of light scatterers (cells) is linearly proportional to the logarithmic ratio of the transmitted light intensity to the incident light intensity. This relation can be understood by visualizing a doubling in density as the light being transmitted through 2 thin slices of identically cloudy material in series. If a fraction, x ($= I/I_o$), of the originally intensity, I_o , passes through the first slice, the total intensity that passes through both slice is $x^2 I_o$, i.e. the density is related to the power of the ratio of the transmitted intensity to the incident intensity. The same argument holds if we increase the pathlength of the light going through the cloudy material. Hence, the optical density with units of Absorbance (A), is related to the intensities by the following equation:

$$OD(A) = -\log_{10} \left(\frac{I}{I_o} \right) = \epsilon l c \quad (3.23)$$

where the base 10 for the logarithm is a convention used when measuring absorbance through liquids (natural log for gases), l is the path length, c is the cell density and ϵ is known as the molar absorptivity. Equation 3.23 is also known as the Beer-Lambert Law.

Optical Density (OD) sensors are predominantly used in bacteria and yeasts cell cultures and rarely for mammalian cell cultures because the larger cell diameters tend to saturate OD measurements even at low cell densities. To illustrate this point, Figure 3-13 shows a plot of the scattering cross section normalized to the cross section area of the polystyrene microspheres, $\sigma_s/(\pi r^2)$, against the dimensionless variable, $\delta = \lambda_1/(2r)$, which is a measure of the ratio between the incident light wavelength and the radius of the sphere.[28] The measurements span over many different regimes, from Rayleigh scattering where the particle size is much smaller than the wavelength, to the Mie regime where the particle size is of the same order as the wavelength, to the Tyrell regime where the particle size is much larger than the wavelength. Typically for OD measurements, visible light is used, typically in the wavelengths between 600-650nm. For bacteria cells with a diameter of $0.5\mu m$, the scattering cross section is approximately $0.5\pi r^2$. Mammalian cells with a diameter of $12\mu m$ and a nucleous

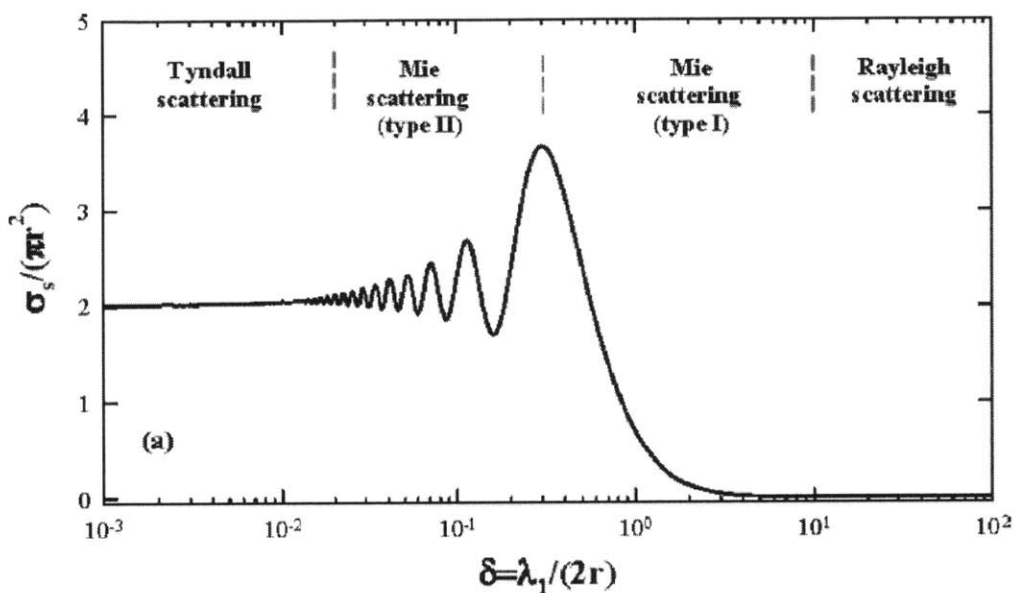
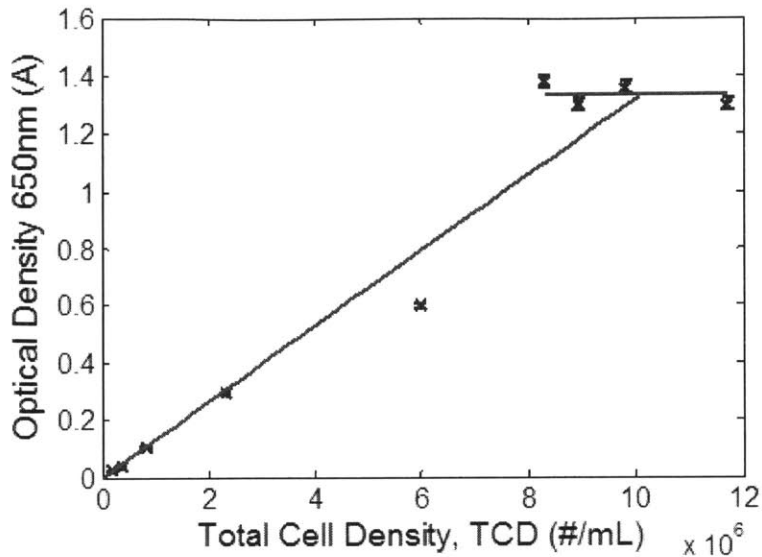


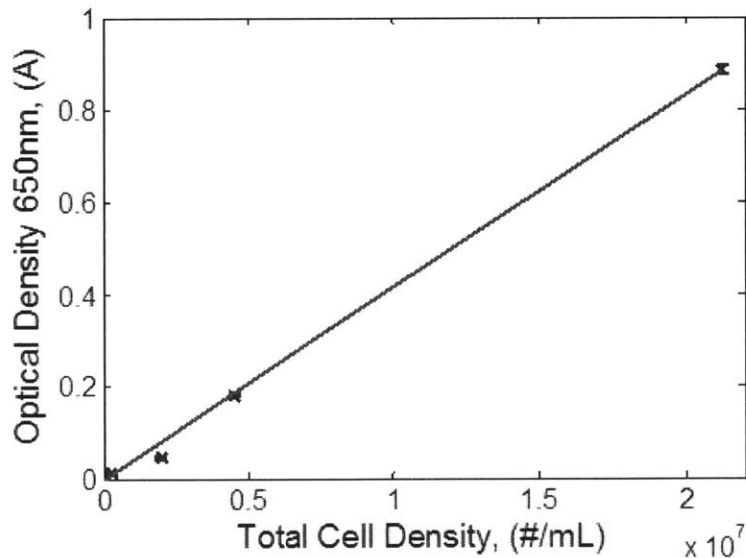
Figure 3-13: Study of scattering cross section as a function of wavelength for polystyrene microspheres suspended in water. The scattering cross section for mammalian cell lines having a larger cell diameter is 2 times cross section area of the cells while for bacteria cells, the scattering cross section is only half the cross section area of cells for visible wavelengths, which is typically used in OD measurements. Therefore, the OD measurements are expected to saturate at a much lower cell density for mammalian cells as compared to bacteria cells.[28]

of $7 \mu\text{m}$, have a much larger scattering cross section of $2\pi r^2$, which means that the mammalian cell culture will reach a saturation point much faster than bacteria cells for the same wavelength. There are OD probes where IR wavelengths are used for OD measurements of larger mammalian cells[76] but these measurements require an IR photodetector, which can be more costly.

When a bench top spectrophotometer (Model: Spectronic 20 Genesys) is used to measure the optical density of CHO cells of varying density, the OD measurements saturate at a cell density of 8×10^6 cells/mL, results shown in Figure 3-14(a). This saturation is undesirable because for CHO cells grown in a bench top bioreactor, the total cell density can reach as high as 30×10^6 cells/mL. Note that OD measurements include dead cells as well since light are scattered by both dead and live cells. From Beer-Lambert's Law (Equation 3.23), the absorbance is linearly proportional to both cell density and path length. In order to prevent the absorbance or OD from saturating at high cell densities, the path length of the measurement can be reduced so that the absorbance remains in the linear regime. The pathlength of the spectrophotometer is 1 cm but since the RECA Micro-bioreactor has a very flat form factor, the maximum path length is only 0.216 cm. Repeating the OD calibration in the micro-bioreactor shows that linearity can be achieved up to at least 21.2×10^6 cells/mL, results shown in Figure 3-14(b). Since the measurement range of the data set shown in the figure is from 0.27×10^6 to 21.2×10^6 cells/mL, and the range of densities of a CHO cell culture spans from 0.2×10^6 to 30×10^6 cells/mL, the OD measurement is linear for a large part of the range needed. It would be ideal to obtain 2 more experimental data points at the edges of the measurement range to ensure that linearity is achieved for the entire range of cell densities in the cell culture.



(a) Spectrophotometer OD measurements at 650nm ($l = 1$ cm)



(b) RECA OD measurements at 650nm ($l = 0.216$ cm)

Figure 3-14: From the OD measurements in the spectrophotometer shown in (a), a linear relationship between the measured absorbance and cell density is obtained for low cell densities. At high cell densities ($> 8 \times 10^6$ cells/mL), the absorbance measured saturates. This is due to the shadowing effect of cells at high densities for the spectrophotometer with a path length of 1 cm. Since the RECA Micro-bioreactor has a flat form factor, the path length of the OD sensor is 5 times shorter than that of the spectrophotometer. Hence, the OD sensor in the RECA is able to achieve linearity at least up to a cell density of 22.2×10^6 cells/mL, potentially even at higher cell densities. Results shown in (b).

3.6 Evaporation Rate

In order to perform an open loop evaporation compensation, the evaporation rate for the RECA Micro-bioreactor should be characterized prior to performing the cell culture experiment. The increase in concentration of green food dye injected into the growth chamber is used as a parameter to calculate the evaporation rate. For this measurement, an intensive variable measurement will be more accurate than an extensive variable (e.g. volume or mass) measurement since the error is larger for an extensive variable and the characterization will be heavily dependent on the experimental procedure. Since the RECA Micro-bioreactor has an optical density (OD) sensor integrated, using the OD sensor to measure the light scattered/absorbed from the green dye is an accurate way to obtain the evaporation rate, α . The increase in dye concentration as a function of time will follow the following relation:

$$C(t) = \frac{C_o}{1 - (\alpha/V)t} \quad (3.24)$$

where $C(t)$ is the concentration of the food dye as a function of time, C_o is the initial concentration of food dye and V is the volume of liquid in the growth chamber (2mL). Since the evaporation rate is not expected to be very high, typically of the order of 1-10 $\mu L/hr$, the experiment is performed overnight (7-8 hours) to obtain a higher accuracy. The results are shown in Figure 3-15. The measured evaporation rate with a local 45°C humidifier attached is 4.7 $\mu L/hr$. If this evaporation is uncompensated, 75% of the volume of the micro-bioreactor will have evaporated by the end of a 14 day experiment. This could significantly increase the osmolarity of the medium and inhibit growth.

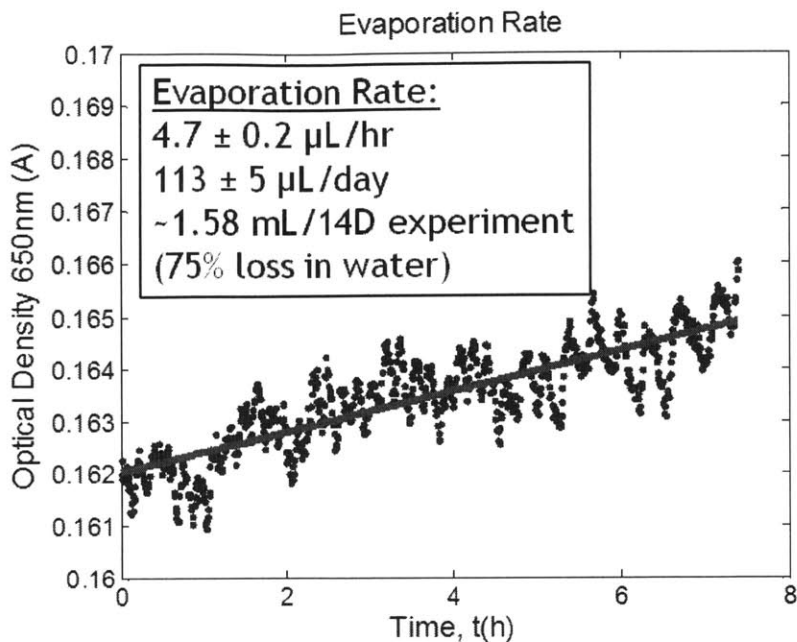


Figure 3-15: The evaporation rate of the RECA Micro-bioreactor with Resistance Line 1 is measured by performing an optical density (OD) measurement on food dye injected into the growth chamber of the micro-bioreactor. The increase in absorbance over time is related to the increase in dye concentration as the volume decreases. The experiment was performed overnight (7-8 hours). The measured evaporation rate is $4.7 \mu\text{L}/\text{hr}$ with a local 45°C humidifier attached.

3.7 Conclusions

The validation of the RECA Micro-bioreactor is in the final phase. The last few validation steps would be: (1) Testing the new pH control strategy of the RECA micro-bioreactor using acidic gassing by CO_2 gas and basic liquid addition of bicarbonate solutions, (2) Validation that open loop evaporation compensation works and (3) Testing of sampling protocol to ensure consistent volume is sampled. Upon completion of the last validation steps, the RECA Micro-bioreactor should be ready for a full biological validation experiment with the Sanofi CHO cell line. For the characterization to date, the RECA Micro-bioreactor has met all the required specifications for a small scale model of industrial bioreactors for culturing CHO cells. The validation results are summarized in Table 3.5.

Table 3.5: Summary of specifications of the RECA Micro-bioreactor and comparison with industrial bioreactors

Physical Parameter	Industrial Bioreactors	RECA Micro-bioreactor
Oxygen $k_L a$	$1\text{-}15 \text{ } h^{-1}$	$1\text{-}7 \text{ } h^{-1}$
Carbon Dioxide $k_L a$	$0.1\text{-}5 \text{ } h^{-1}$	$2\text{-}5 \text{ } h^{-1}$
Max. Shear Stress	$0.005\text{-}0.8 \text{ Pa}$	$0.008\text{-}0.025 \text{ Pa}$
Mixing Time	$20\text{-}120 \text{ s}$	$27\text{-}114 \text{ s}$
Max. OD (Cell Density)	$30 \times 10^6 \text{ cells/mL}^*$	$> 20 \times 10^6 \text{ cells/mL}$
Online Sensors	T, pH, DCO_2 & DO_2	T, pH, DCO_2 , DO_2 & <u>OD</u>
Offline Analytics	Compatible	Compatible
End Point Analytics	Compatible	Compatible

*OD sensor is typically not present in Industrial Bioreactors

Chapter 4

Dielectric Spectroscopy

4.1 Introduction

The cultivation of Chinese Hamster Ovary (CHO) cells differs significantly from that of bacteria cells. With these different requirements, the micro-bioreactor design will need to be modified significantly, the modifications have been described in great detail in Chapter 2. Besides that, new sensors need to be integrated into the micro-bioreactor for better control and monitoring of CHO cultures. One of them is the integration of CO₂ optode to monitor dissolved CO₂ levels in the media since the accumulation of dissolved CO₂ concentration is known to affect the pH and increase the osmolarity in the medium which leads to growth inhibition. The calibration of the CO₂ optode was discussed in Chapter 3. In addition, since CHO cells are very sensitive to physical and chemical stresses, cell viability is a very important parameter to monitor for CHO cell cultures. The integration of dielectric spectroscopy sensors for viability monitoring in the micro-bioreactor will greatly enhance the capabilities of the micro-bioreactor.

This chapter first outlines the theory of dielectric spectroscopy, then describes an important measurement parasitic effect known as electrode polarization. The methods of reducing (physical methods) and correcting (analytical method) for electrode polarization are then described in detail. Two possible electrode design, interdigitated and four electrode configurations are compared against each other to decide the best

design for our system. Two types of interdigitated electrodes will be used for biological validation experiments. The first set of experiments consist of larger electrode and the dielectric spectra is corrected by the subtraction method. Electrode polarization cannot be completely corrected by this method and the results show this. In order to better fit the electrodes to the micro-bioreactor, a smaller interdigitated electrode is designed. The experiments with this electrode utilizes a different correction method by modeling out the parasitics. This correction method turns out better for *in situ* measurements and the measurement results are quantitatively comparable with the results from literature values for the dielectric spectroscopy experiments on CHO cells. The chapter ends with fabrication of platinum electrodes on polycarbonate, the material used to fabricate the RECA Micro-bioreactor for future integration.

4.2 Theory of Dielectric Spectroscopy

The basics of dielectric spectroscopy for measuring viable cell density, described elsewhere [14], will be summarized in this section. When cells in an aqueous medium are placed under an electric field, charges will accumulate at the surface of the cells, containing two interfaces of different materials, the cytoplasm-cell membrane and cell membrane-aqueous medium. These charges will accumulate at the poles of the cells determined by the direction of the electric field forming dipoles, the effect is known as interface polarization. The effective permittivity of the medium is increased due to the presence of these cellular dipoles. Under an oscillating field, at low frequencies, the polarizing charges across the cell will oscillate in phase with the oscillating field. When the oscillating frequency is increased, the oscillation of the polarizing charges will lag behind the field and then diminishes at high frequencies. This creates a dispersion in the effective permittivity of the medium containing these biological cells. The position of this dispersion have a strong dependence on the geometry of the interface, i.e. the size of the cell, and the permittivity of the interface materials. For biological cells, this dispersion, known as the β -dispersion, occurs at the radio frequencies, with the high permittivity being constant at below 500kHz and

the low permittivity at above 10MHz. Therefore, the change in effective dielectric constant, $\Delta\epsilon = \epsilon_{Lo} - \epsilon_{Hi}$, of the medium between low and high frequencies at radio frequencies can be attributed solely to the presence of biological cells with intact cell membranes in the medium. Dead cells, which no longer have intact cell membranes, and cell debris do not contribute to the effective permittivity of the medium. Since the dispersion in permittivity is insensitive to dead cells, dielectric spectroscopy can be used as a method to measure viable cell density.

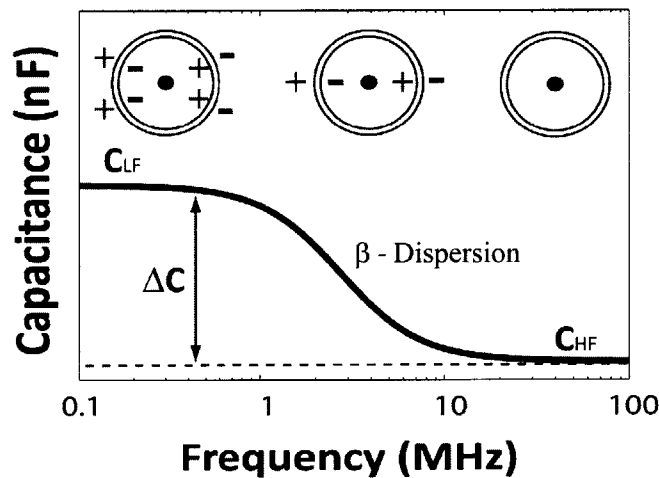


Figure 4-1: Capacitance of the cell suspension versus frequency in the log scale. The difference between low frequency and high frequency capacitance around the β -dispersion gives the change in capacitance due to the presence of viable cells in the suspension.

To model the dispersion relation, we start with the Debye equation (Equation 4.1) which describes the change in permittivity due to the orientation of polar molecules in an AC field. It is assumed that the rotation of polar molecules can be described by a single relaxation time, τ . The static permittivity and high (infinite) frequency permittivity are represented by ϵ_s and ϵ_∞ . The derivation of the Debye equations representing a dispersion for a single relaxation time is described in Appendix A. The equations are general enough and can be applied to any dispersion relation with a single relaxation time.

$$\epsilon^* = \epsilon_\infty + \frac{\epsilon_s - \epsilon_\infty}{1 + iw\tau} \quad (4.1)$$

The dispersion of actual aqueous solutions are better represented by another equation known as the Cole-Cole Model(Equation 4.2) where α is an empirically determined variable.[12] The physical justification for the power factor α is that it represents the dispersion due to a distribution of time constants around a central relaxation time, τ . The β -dispersion for biological cells can be modeled very accurately by the Cole-Cole dispersion model.

$$\epsilon^* = \epsilon_\infty + \frac{\epsilon_s - \epsilon_\infty}{1 + (iw\tau)^{1-\alpha}} \quad (4.2)$$

In order to interpret dielectric spectroscopy measurements and correlate it to viable cell density, the relationship between the permittivity, due to the polarized live cells, and the viable cell density must be determined. Modeling the polarized cells as non-interacting dipoles, Pauly and Schwann [60] showed that there is a linear relationship between the volume fraction of viable cells, P , and $\Delta\epsilon$, as shown in Equation 4.3, where r is the cell radius, C_M is the membrane capacitance and ϵ_0 is the vacuum permittivity. Typically, dielectric spectroscopy measurements are performed by applying an oscillating potential to a pair of electrodes and measuring the change in capacitance across the electrodes between low and high frequencies.

$$\Delta\epsilon = \left(\frac{9rC_M}{4\epsilon_0} \right) P \quad (4.3)$$

4.3 Electrode Polarization

When an electrode is placed in an aqueous medium, the interface potential of the electrode will attract counter ions to the electrode surface forming an electrical double layer (EDL), as illustrated in Figure 4-3(a). When an oscillating current is applied to the electrode, the current will perturb the EDL at the surface of the electrode modulating it at the same frequency but with a slight lag. This effect is known as AC

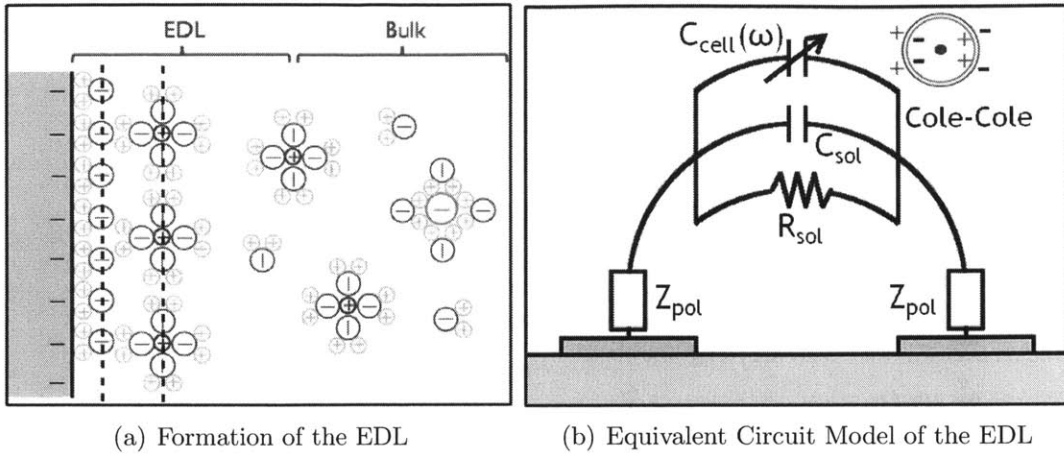
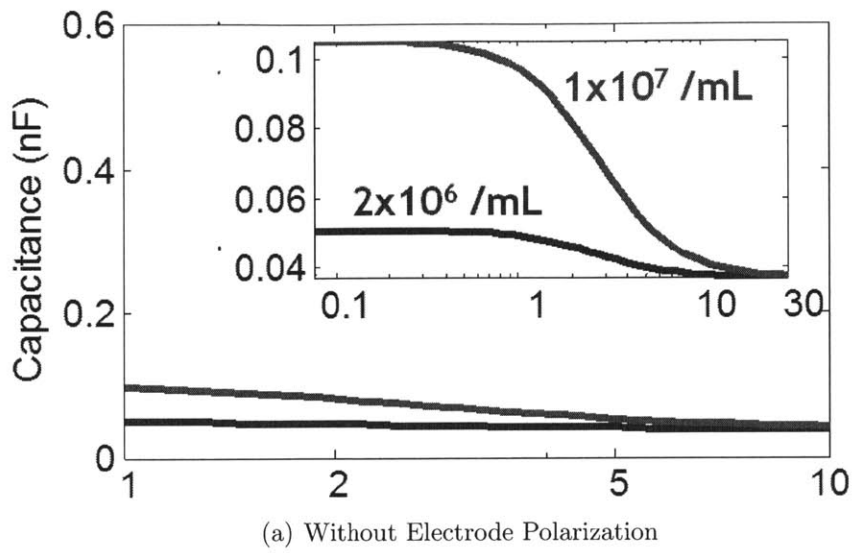


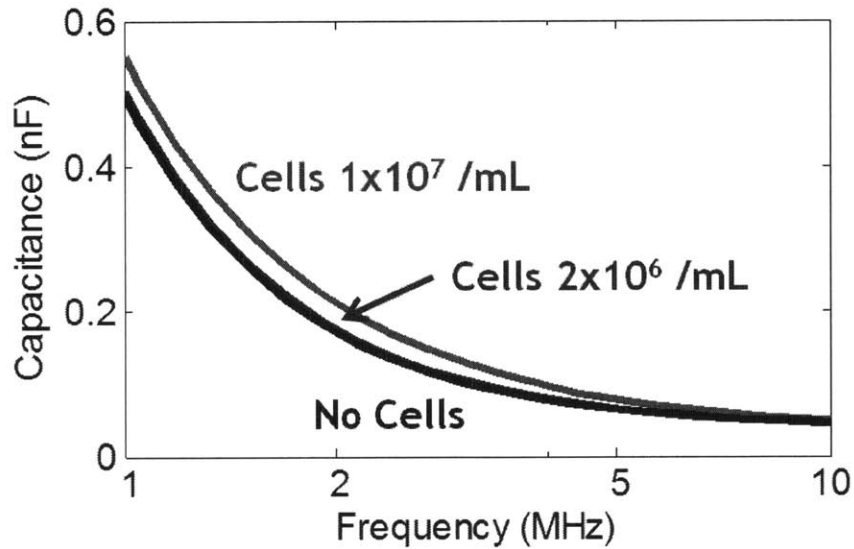
Figure 4-2: Physical and equivalent circuit model for the Electrical Double Layer (EDL) parasitics.

electrode polarization and the presence of the EDL adds a parasitic capacitance to the measured capacitance of the suspension. The equivalent circuit model for an aqueous solution of conductivity σ is represented by a resistor, $R_{sol} = (d/A)1/\sigma$, in parallel with a Capacitor, $C_{sol} = \epsilon_w\epsilon_o(A/d)$, where ϵ_w is the dielectric constant for water and ϵ_o is the permittivity of free space. These relations are specifically for a parallel plate electrode measurement where parallel electrodes of area, A are separated by a spacing, d . The dispersion capacitance of the cells adds as another element in parallel represented by a frequency dependent capacitor, $C_{cell}(w)$. The electrode polarization effects are impedances, Z_{pol} that are in series with the equivalent circuit model for the suspension, since the presence of the electrical double layer modifies the potential of the surface of the electrode. The equivalent circuit model is shown in Figure 4-3(b).

The electrode polarization effect is stronger at low frequencies when the ions have sufficient time to form the electrical double layer and when the suspension is at a higher conductivity because the higher density of ions in the medium shields the electrode more efficiently, i.e. at a faster rate. Since CHO cells are usually suspended in media of high conductivity (12-14 mS/cm), the contribution from electrode polarization to the dielectric measurement at low frequencies could be an order of magnitude higher than the contribution from the live cells and needs to be corrected



(a) Without Electrode Polarization



(b) With Electrode Polarization

Figure 4-3: Effects of electrode polarization on the dielectric spectra. Figure (a) shows the theoretical prediction of the dielectric spectra for CHO cells of densities 2×10^6 cells/mL and 1×10^7 cells/mL. With the effects of electrode polarization added to the spectra, the resultant graph results in a rapidly increasing capacitance at low frequencies as shown in (b). The dispersion due to the cells is completely buried in the electrode polarization parasitics.

(Figure 4-3). Correcting for electrode polarization for CHO cell suspensions is further complicated by the fact that the metabolism of glucose by CHO cells will increase the conductivity of the medium, which results in a corresponding change in the electrode polarization effect. In order for dielectric spectroscopy to be a complete solution for online CHO cell viability monitoring in micro-environments, there must be an online, real-time correction scheme for electrode polarization which can account for the varying conductivity of the suspension medium.

4.4 Physical Methods

When dealing with parasitics, the first step is to reduce or minimize the effects of the electrode polarization and thereafter, try to correct for electrode polarization from the measurement data. In this section, the methods of reducing electrode polarization are called physical methods because it involves careful selection of the medium conductivity, electrode material and roughness.

4.4.1 Conductivity Reduction

The medium conductivity has a significant effect on the electrode polarization as shown in Figure 4-4. The relaxation time for the formation of the electrical double layer (EDL) is dependent on the rate of diffusion of the counter ions to the charged electrode surface. If the bulk ionic concentration is higher, the rate at which ions shield the electrode to form the EDL will be much faster. Hence, the electrode polarization effect is expected to extend to higher frequencies for media of higher conductivities. It would be great if it were possible to reduce the medium conductivity so that the electrode polarization effects will shift to a frequency much lower than the β -dispersion for CHO cells. However, since the cell medium concentrations have been optimized for cell productivity and growth, altering the medium conductivity would not be an option for this particular application.

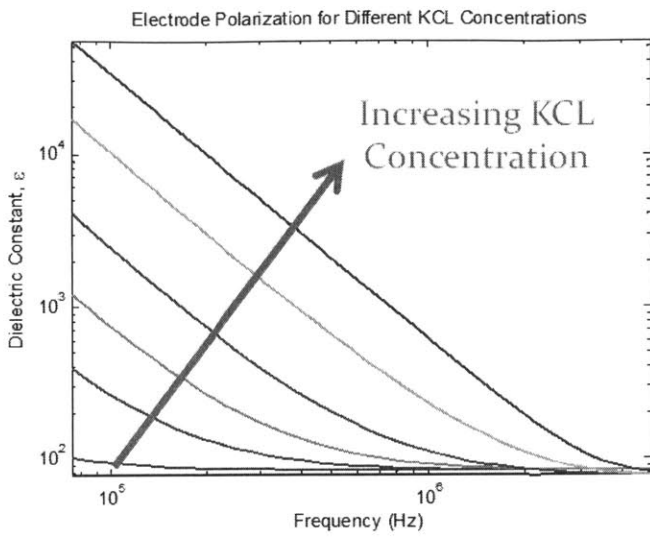


Figure 4-4: The effects of the media conductivity on electrode polarization. This is an experiment performed by measuring KCl solutions of increasing concentration. As conductivity increases the time it takes to form the EDL decreases and hence the electrode polarization shifts to higher frequencies for high conductivity media.

4.4.2 Electrode Material Selection

Alternatively, electrode polarization effects can be minimized through careful selection of electrode material. Platinum and gold electrodes have been experimentally demonstrated to have the lowest electrode polarization due to their low interface potential or polarization potential.[47] Having a lower interface potential means that when a current flows from the aqueous medium into the electrode, the electrodes have a lower tendency to polarize, i.e. current can flow freely into the electrodes without forming charges on the interface between the electrode and the aqueous medium. Electrodes that exhibit this behavior tend to have lower electrode polarization effects since they have less charge buildup at the interface when a voltage is applied across the electrodes.

Platinum electrode is the preferred electrode material for dielectric spectroscopy since it has the lowest polarization potential. Moreover, it is inert which eliminates potential chemical degradation of the electrodes. On the other hand, Gold electrode,

though having a slightly higher polarization potential, can be chemically patterned, which is impossible for Platinum electrode because it is too chemically inert. Gold reacts with thiol molecules and hence, can be coated with an anti-adhesive coating to prevent CHO cells or proteins from adhering to the electrodes.[52] There are certainly advantages to using either Platinum or Gold electrodes. In this thesis, the initial tests will be performed on Gold electrodes since it can be coated to prevent cell or protein adhesion.

4.4.3 Rough Electrodes

It has also been shown that by coating a layer of platinum black, i.e. fine platinum particles, on the electrodes, the effects of electrode polarization can be minimized further by increasing the effective surface area or the roughness of the electrodes.[47] Having microscopically rough electrodes means that the capacitance of the EDL close to the electrode interface can be increased due to the higher surface area, which reduces the impedance of the electrode polarization. Far from the electrode interface, in the bulk of the medium, these microscopic roughness appears as smooth and hence the capacitance of the medium is unaffected. This reduces the impedance of electrode polarization while keeping the impedance of the medium constant resulting in lower parasitic effects. However, the long term use of platinum black electrodes can lead to problems due to the fact that the platinum black coating will degrade over time, the degradation is accelerated when there is flow or mixing over the electrodes and the resulting particles are toxic to biological cells.[47] On these grounds, the platinum black electrodes, though effective in reducing electrode polarization, for practical reasons, is unsuitable for this application.

4.5 Analytical Methods

Since electrode polarization effects cannot be completely eliminated through physical methods, the data analysis of any dielectric spectroscopy measurements must include methods to correct for electrode polarization. The two most commonly employed

methods for electrode polarization correction are the subtraction method[14] and the constant phase element correction method.[6]

4.5.1 Subtraction Method

In the subtraction method, the dielectric spectra of the cell suspension is subtracted with the spectra of a cell-free medium with the same conductivity, matched by adding potassium chloride (KCl) salts or diluting with deionized (DI) water. Davey et al.[14] showed that the electrode polarization is strongly dependent on the conductivity of the solution and the valency of the ions but not on the exact species of the ions. Since the conductivity of most biologically relevant media are dominated by univalent ions, altering the conductivity of the culture medium using KCl solution to match the conductivity of the medium with cells is technically equivalent to measuring the supernatant directly. The advantage of this method is that it can correct for the electrode polarization exactly but the disadvantage is that it requires knowing the medium conductivity for that data point and performing an additional external measurement to obtain the dielectric spectra for the medium alone without cells. This is undesirable for an *in situ* measurement of cell viability since the measurement is now limited by the rate at which the external measurement can be performed and hence, the dielectric spectroscopy measurements are limited by *ex situ* measurements.

4.5.2 Constant Phase Element (CPE) Correction

Experiments have shown that the electrode polarization can be modeled with a constant phase element (CPE) model, an empirically determined model.[6] The CPE model describes the electrode polarization as an impedance element that is similar to that of a capacitor but have a constant phase between -45° and -90°. In the equivalent circuit model shown in Figure 4-3(b), the Z_{pol} for the CPE model is given by the following equation:

$$Z_{pol} = \frac{1}{Y_o(jw)^\alpha} \quad (4.4)$$

where $0.5 \leq \alpha \leq 1$. Since this empirical model fits the electrode polarization data so well, attempts have been made to come up with a physical explanation for the model. The closest physical explanation is the by describing electrode surface roughness by a fractal model where the angle dependence, α , is related to the fractal dimension, D , of the electrode surface by the following relation:[56]

$$\alpha = \frac{1}{D - 1} \quad (4.5)$$

where the limits of the fractal dimensions, D , for the 2-Dimensional surface ($2 \leq D \leq 3$) sets the limits of α ($0.5 \leq \alpha \leq 1$). A more physically intuitive explanation of the CPE model relates the linear relation between the resistive and capacitive component of the constant phase element to the fact that the energy dissipation and energy storage rate of the EDL are linearly related. There are many groups that have successfully used the CPE method to correct for EP effects but most of them were for low conductivity media.(Table 4.1) Yoon et al. has modeled CPE for high conductivity (biologically relevant) solutions in contact with Pt electrodes but his experiments were not performed in the presence of live cells. The focus of the next chapter will be on correcting electrode polarization effects using CPE high conductivity media with a conductivity range of 1.2-1.4 S/m in the presence of live CHO cells at different stages of the culture.

Table 4.1: CPE correction performed in literature for different types of electrodes and media conductivity

Author, Year	Electrode Type	Conductivity (S/m)
Bordi, 2001[6]	Platinum	0.7 - 0.8
Tirado, 2003[72]	Pt Black	0.005 - 0.65
Sanabria, 2006[65]	Steel	0.005 - 0.15
Yoon, 2011[77]	Platinum	0.5 - 1.4
Ben Ishai, 2012[4]	Titanium	0.001 - 0.05
Current Work	Gold	1.2 - 1.4

4.6 Design of Electrodes

The design of electrode geometry or configuration can also help to reduce electrode polarization effects. Four electrode measurements, which separate the current driving electrodes from the potential sensing electrodes have been proposed by Schwan in 1963[67] to reduce electrode polarization effects compared to simpler two electrode systems. Since then, four electrode systems for dielectric spectroscopy measurements have been implemented with various levels of success.[68, 27, 5, 55] In Schwan's ideal model, the potential sensing electrodes have infinite impedance and zero current. Real electrodes are never ideal and hence, parasitic capacitances and electrode polarization effects are still evident in four electrode methods.[51] Therefore, two electrode measurements remain popular for dielectric spectroscopy because they have a simpler interpretation, similar to that of parallel plate electrodes, and more flexibility in electrode design.

Electrodes for dielectric spectroscopy optimized for micro-bioreactors must take into account the geometry of the growth chamber. Typically, the growth chamber has a large area and a thin cross section in a microfluidic device like a micro-bioreactor. Electrodes could be patterned on one side or both sides of the growth chamber walls. Patterning the electrodes only on one side is preferred because it reduces fabrication complexity. For a micro-bioreactor, the growth chamber is typically very thin and hence the sensing depth of the electrodes becomes very important. For co-planar electrodes, the sensing depth is a function of the electrode spacing and width instead of being simply the space between two parallel electrodes. In our analysis, the sensing depth is defined as the depth for which 99% of the electric field lines penetrate. For shallow environments like micro-environments, tuning the sensing depth of the electrodes is important for optimizing the sensitivity of the measurement to the region of interest. If the electrodes are too wide or spaced too far apart, the sensing depth will penetrate far beyond the region of interest, which in this case, is the height of the cell suspension. This reduces the sensitivity of the electrodes to changes in the cell suspension since a large portion of the permittivity measured is not from

the cell suspension. For a shallow sensing depth, the electrodes are typically closer together. However, this also leads to a lower sensitivity due to a lower capacitance reading. The interdigitated electrode structure (IDES) is perfect for overcoming this problem because the high density of electrode combs still gives a high capacitance reading even for a shallow sensing depth. Another electrode geometry to consider is the four electrode structure (4ES). Although the 4ES will not be able to give a large capacitance reading, it has the advantage of being able to correct for parasitic electrode polarization effects.

4.6.1 Interdigitated Electrodes Structure (IDES)

To achieve a shallow sensing depth, the electrodes in a micro-bioreactor would have to be very narrow and close to each other. For a simple two planar electrode geometry with a shallow sensing depth, this would mean that the dielectric spectroscopy measurements would be of the order of 10pF. Since stray capacitances due to electrical lines running around the building tend to have magnitudes of approximately 1pF, the noise in this simple two electrode configuration could be as high as 10% of the measured capacitance. For the same shallow sensing depth, a two electrode system in the form of interdigitated electrodes would be able to measure capacitances on the order of 100 pF because the interdigitated structure can increase the capacitance measured without affecting the sensing depth of the electrodes. Using conformal transformation[57], we can analytically calculate the cell constant, κ , of the interdigitated electrode structure which is the inverse of the geometrical factor relating the capacitance, C , to the dielectric constant of the media, ϵ .

$$C = \frac{\epsilon\epsilon_0}{\kappa} \quad (4.6)$$

A schematic of the interdigitated electrode is shown in Figure 4-5. The interdigitated electrode geometry is defined by the number of electrodes, N , the length, L , and width, w , of each electrode, and the spacing in between electrodes, s . The calculated cell constant and expected capacitance of water for two of our proposed interdigitated

electrode geometry are shown in Table 4.2. The actual cell constant of the interdigitated electrodes determined experimentally will be lower than that predicted by the analytical model since the additional edge effects would lead to a higher measured capacitance.

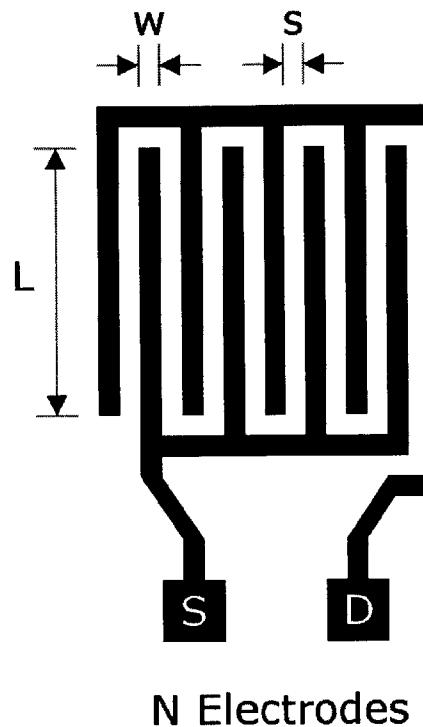


Figure 4-5: Schematic showing dimensions for the analytical model for the cell constant of the Interdigitated Electrode. For the electrodes drawn in this figure, $N = 9$. D refers to the driving electrode and S refers to the sensing electrode.

Table 4.2: Geometrical description of the Interdigitated Electrodes(IDES) and the corresponding calculated cell constant

Type	Area (in. \times in.)	N	L(in.)	w(in.)	s(in.)	$\kappa(m^{-1})$	$C_w(pF)$
Large IDES	0.85×0.89	45	0.83	0.01	0.01	2.03	344
Small IDES	0.28×0.29	15	0.26	0.01	0.01	20.43	34

4.6.2 Four Electrodes Structure (4ES)

Theoretically, an ideal four electrode measurement would not be affected by electrode polarization. Two outer electrodes will drive AC current through the sample and the potential drop across the sample is measured by the two inner electrodes connected to a high impedance voltmeter. Due to the high impedance, no current flows through the inner electrodes. Since the AC electrode polarization effect is caused by the perturbation of the electrical double layer (EDL) by the flow of AC current, the separation of the current driving outer electrode and potential sensing inner electrode will eliminate the effects of AC electrode polarization from the sensing electrodes. An equivalent circuit of the four electrode configuration is shown in Figure 4-6. The sample impedance, Z_S , is divided into 3 parts, Z_L , the measured impedance, Z_M , and Z_R , by the four electrodes. The middle section will be free from electrode polarization effects, represented by Z_P , since there would be no current flowing through the two electrodes around Z_M . Ideally, if the current is known, we can obtain Z_M without being affected by Z_P . However, a practical measurement setup might not be able to eliminate electrode polarization effects completely.

Previously, for the two electrode configuration, the measurements can be performed using an LCR meter with an auto-balancing bridge. However, even though the LCR meter has four terminals labeled, it is not designed for a four point AC measurement for large contact resistances, i.e. the resistance between L_C and L_P . Figure 4-7 describes this discrepancy. A circuit showing the auto-balancing bridge measurement configuration of the LCR meter for a two electrode configuration is shown in Figure 4-7(a). The figure shows how the four terminals of the LCR meter labeled, H_C , H_P , L_P and L_C are connected to a Device Under Test (DUT) and the equivalent circuit components connected to each terminal. The LCR meters gives the impedance of the DUT, Z_S , by taking the voltmeter reading, V_x , and dividing it by the current, given by V_r/R_r , therefore $Z_{meas} = (V_x R_r)/V_r = Z_S$. This relation only holds if we assume the contact resistance between L_P and L_C is negligible compared to R_r .

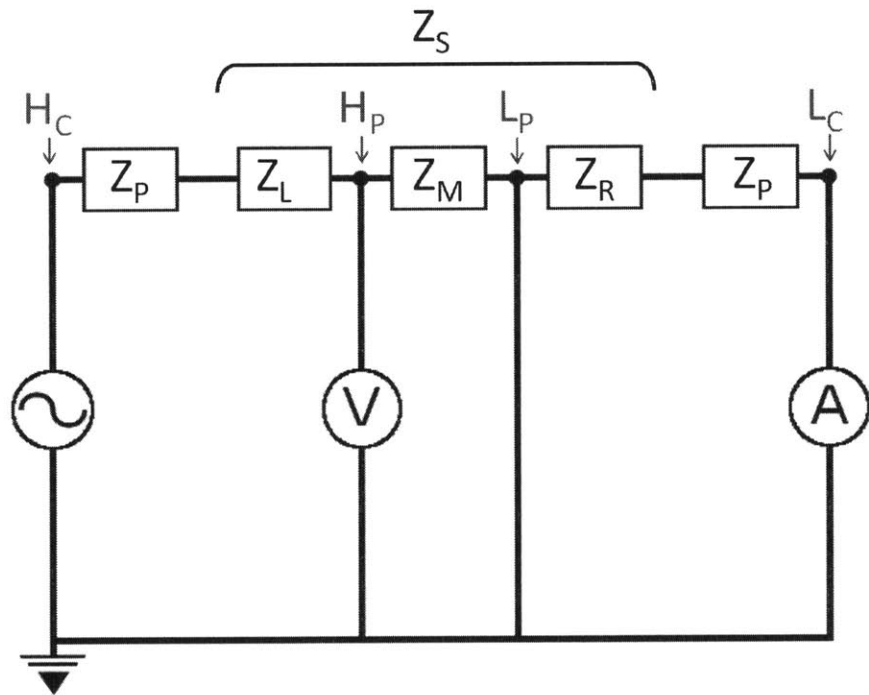
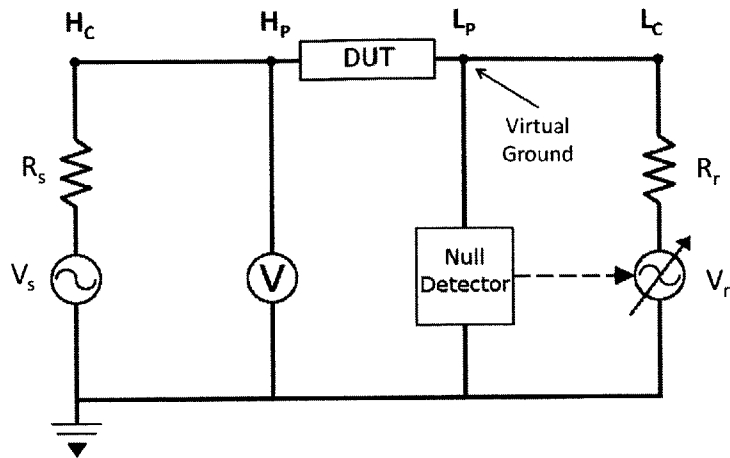


Figure 4-6: An ideal equivalent circuit of the four electrode configuration (H_C, H_P, L_P, L_C) showing sample impedance, Z_S split into 3 sections (Z_L, Z_M, Z_R) and the electrode polarization impedance, Z_P . Division of the voltage between the inner electrodes, H_P and L_P , with the current gives Z_M which does not include any polarization impedance, and hence the four electrode measurement, ideally, can be AC electrode polarization free.

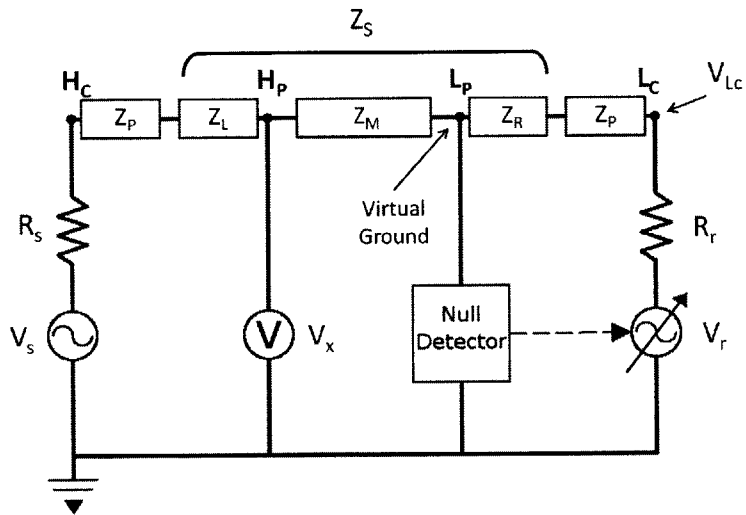
Figure 4-7(b) shows the equivalent circuit when the LCR meter is connected to a four electrode measurement configuration using the four terminals, H_C , H_P , L_P and L_C . Z_M is the impedance that we want to measure and it's related to the geometry of the electrodes and also free of electrode polarization effects. Now the meter reading, $Z_{meas} = (V_x R_r) / V_r \neq Z_M$, since $V_r / R_r \neq I$. The current, I , is given by the following two relations, $I = V_r / (R_r + Z_P + Z_R)$ and $I = (V_r - V_{Lc}) / R_r$. The first relation is hard to deal with since it involved Z_P the electrode polarization which is unknown. The second relation involved measuring V_{Lc} and knowing R_r . It is possible to build a setup to measure V_{Lc} . However, as per a call made to the technical specialists in Agilent, the makers of the LCR meter, they cannot reveal the value of the resistance R_r . The only remaining options are either to experimentally determine R_r or make a new circuit to perform the measurement without using the LCR meter. An example of a possible measurement circuit is described in this reference.[20]

4.6.3 Comparison between IDES and 4ES

The interdigitated electrode structure (IDES) is a two electrode configuration, which is easier to implement since it can be hooked up to a commercial impedance analyzer. Moreover, the interdigitated structure can provide a larger signal compared to the four electrode structure for the same sensing depth. This can be a very important factor since for shallow bioreactors, the four electrode configuration has a signal level that is close to that of parasitic capacitances ($\sim 1pF$). However, most biological media have high conductivity and hence the measurements of the IDES system can be masked by high electrode polarization effects caused by the modulation of the electrical double layer (EDL) by the current flowing through the electrode. The four electrode system (4ES) can overcome this problem by separating the current driving electrodes from the potential sensing electrodes. The 4ES system is a more complicated system to implement since it is not straightforward compatible with commercial impedance analyzers and the interpretation of the results will depend on the measurement method. However, the low electrode polarization makes it an attractive electrode configuration.



(a) A circuit showing the auto-balancing bridge measurement configuration of the LCR meter. The figure shows how the four terminals of the LCR meter labelled, H_C , H_P , L_P and L_C are connected to a Device Under Test (DUT) and the equivalent circuit components connected to each terminal.



(b) This figure shows the equivalent circuit when the LCR meter is connected to a four electrode measurement configuration using the four terminals, H_C , H_P , L_P and L_C . Z_M is the impedance that we want to measure and it's related to the geometry of the electrodes and also free of electrode polarization effects. Now the meter reading, $Z_{meas} = (V_x R_r)/V_r \neq Z_M$, since $V_r/R_r \neq I$.

Figure 4-7: This figure shows how the four terminals of the LCR meter cannot be directly used to perform four electrode measurements for dielectric spectroscopy

4.7 Large IDES Electrode Experiments

The first set of experiments were performed on large electrodes, whose dimensions are described in the Table 4.2 under the name Large IDES. These electrodes were designed to cover the entire bottom of the micro-bioreactor. A photograph of the electrodes and the connection to the LCR meter is shown in Figure 4-8. In order to perform an accurate measurement, first the cell constant of the interdigitated electrodes need to be experimentally determined. This is done in combination with the correction for the electric residuals of the electrodes described in the next section. After performing the electrode residual correction and determining the cell constant of the electrodes, dielectric properties can now be obtained but the data still contains electrode polarization effects. The next section deals with the data analysis to remove electrode polarization effects by using the subtraction method but pre-calibrated instead of measuring the spectra in parallel with the measurement. The experimental protocol for the biological validation is then described in the next section. The results are then discussed at the end of this section.

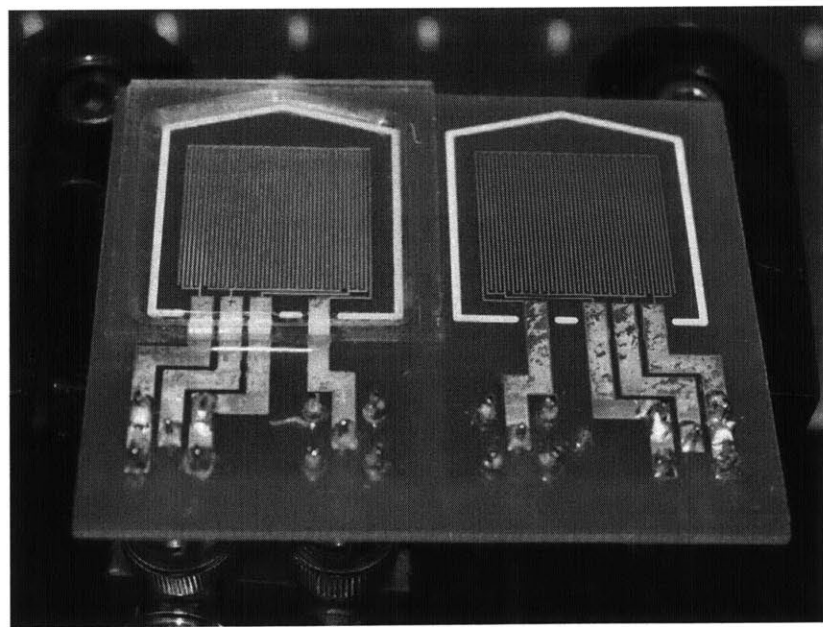


Figure 4-8: Printed Circuit Board (PCB) with identical gold interdigitated electrodes used for testing the electrode geometry

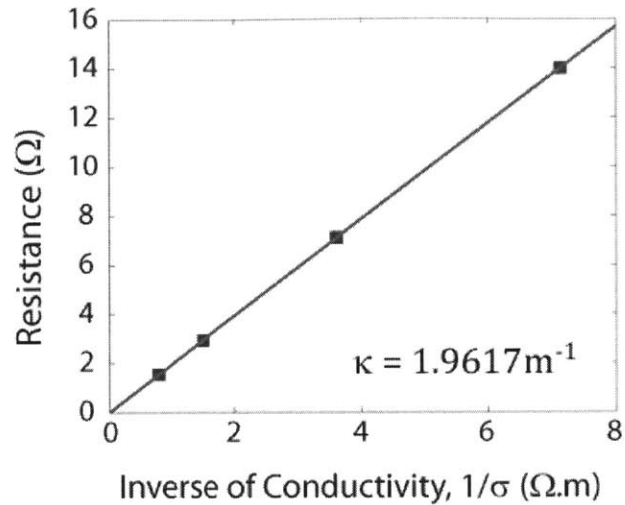
4.7.1 Calibration

Cell Constant

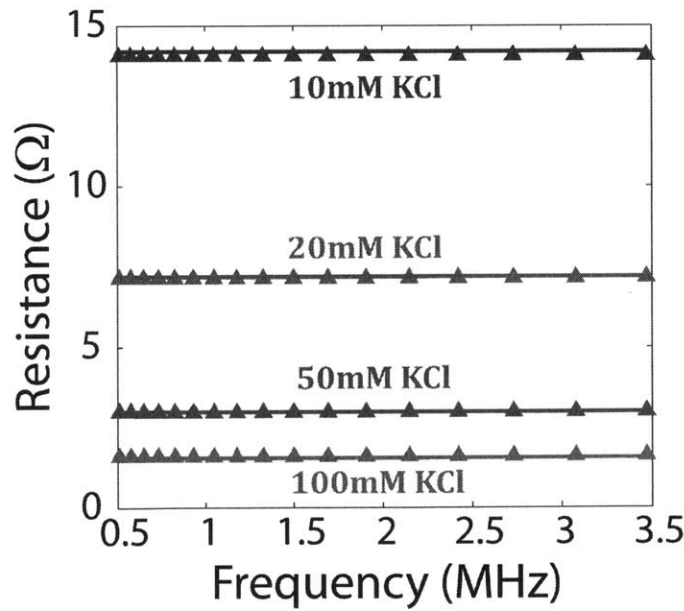
The geometrical cell constant of the electrodes is measured by calibrating the resistance of the solutions, R , measured using the interdigitated electrodes, with their respective conductivities, σ , of 10mM, 20mM, 50mM and 100mM aqueous potassium chloride (KCl) solutions. The dielectric spectroscopy measurements are performed using an Agilent 4285A LCR meter which has a frequency range between 75kHz and 30MHz. After each measurement, the electrodes are washed with deionized (DI) water 3 times and then dried with a Kimwipe to prevent contamination between the samples. The conductivities of the solutions are measured with a Thermo Scientific Orion 5 Star Benchtop pH/Ion Meter. The relationship between the geometrical cell constant, κ , to the measured resistance, R , and conductivity, σ , is given by Equation 4.7.

$$\kappa = R\sigma \quad (4.7)$$

The results of the calibration with 10mM, 20mM, 50mM and 100mM KCl solution is shown in Figure 4-16. The cell constant, κ , of the electrodes is measured to be 1.96m^{-1} , which is very close to the theoretical value of 2.03m^{-1} . In the theoretical model, edge effects have been ignored. Hence, the cell constant calculated will be higher than the actual cell constant since the additional edge effects will result in a lower value of the cell constant, i.e. a higher value of capacitance measured. The cell constant calibration with resistance is performed at lower frequencies, from 75kHz to 5MHz, because at higher frequencies the resistance will be affected by residual inductances in the electrode system. After the cell constant is determined for the electrodes, the resistance and capacitance that is expected for air, DI water and KCl solutions of different molarities are now known and can be used to correct for electrode residuals.



(a) The linear relationship between R and $1/\sigma$ data (■) and fitting curve (-) The calibrated cell constant, κ , is 1.9617 m^{-1}



(b) Measurement data(▲) and fitting curve (-) using the calibrated value of the cell constant

Figure 4-9: Calibration of electrode cell constant with 10mM, 20mM, 50mM and 100mM KCl solutions

Electrode Residuals

In general, the interdigitated electrodes will also contribute to the impedance measured by the LCR meter. To obtain the impedance of the sample, the impedance of the electrodes need to be subtracted from the measured impedance. An LCR circuit model for the interdigitated electrodes and sample is shown in Figure 4-10. If the sample has a low impedance, which is the case for high conductivity cell media, the parallel residual impedance of the electrodes, $Y_P = G_P + jwC_P$, will be shorted out by the sample impedance. Hence, only the series residual impedance, $Z_S = R_S + jwL_S$, needs to be subtracted from the measured impedance, Z_{MEAS} , to obtain the actual sample impedance, Z_{SAMPLE} . Conversely, if the sample has a high impedance, the parallel residual impedance of the electrodes, Y_P , dominates in the measurement. The measured impedance must be corrected by subtracting with the residual impedances according to the equations below.

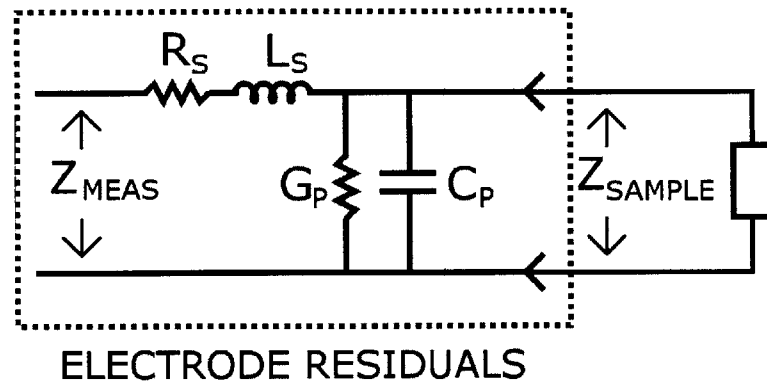


Figure 4-10: General model for the residuals of the interdigitated electrodes

For low impedance sample,

$$Z_{SAMPLE} = Z_{MEAS} - Z_S \quad (4.8)$$

For high impedance sample,

$$Z_{SAMPLE} = \frac{Z_{MEAS}}{1 - Z_{MEAS} \cdot Y_P} \quad (4.9)$$

In order to determine the electrical residuals of the interdigitated electrodes, the electrodes will be calibrated with air, deionized (DI) water, 1mM, 10mM and 100mM potassium chloride (KCl) solution. For the air or high impedance measurement, we can easily obtain the values of the parallel residual capacitance, C_P , and conductance, G_P , by assuming the sample impedance is the capacitance of air. For the 100mM KCl or low impedance measurement, the series residual resistance, R_S , and inductance, L_S , of the electrodes can be determined if the conductivity of the KCl solution is known. The permittivity of the KCl solution can be assumed to be close to the permittivity of water. The fitting for 100mM KCl solution is only performed at frequencies above 1MHz to prevent the calibration from being influenced by the effects of electrode polarization. The obtained values of G_P , C_P , R_S , and L_S is then substituted into the data for DI water, 1mM KCl, 10mM KCl solution to check for consistency using the full form of the correction for residual impedances as shown in the equation below.

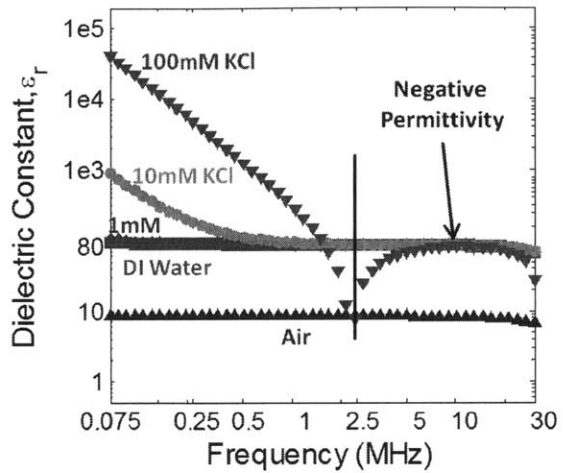
$$Z_{SAMPLE} = \frac{(Z_{MEAS} - Z_S)}{1 - Y_P \cdot (Z_{MEAS} - Z_S)} \quad (4.10)$$

When the electrodes are used to measure the dielectric spectra of Air, DI water, 1mM, 10mM and 100mM KCl solutions without correcting for electrode residuals, the results are as shown in Figure 4-17(a). The capacitance spectra is converted to dielectric constant using the experimentally determined cell constant, $\kappa = 1.96m^{-1}$. Since we know that the dielectric constant of air is 1 and of water is ~ 80 , the dielectric constant of air should be at 1 for all frequencies and the dielectric constant of DI water and all KCl solutions should reduce to the dielectric constant of water at high frequencies, when the effects of electrode polarization is diminished. From the graph, the dielectric spectra of air is heavily affected by the residual parallel capacitance of the electrode, C_P , and hence shows a higher dielectric constant than the actual dielectric constant of air. The spectra of DI water and 1mM KCl overlapping with each other, shows very little effect of electrode polarization and also are not affected by the electrode residuals since they are flat and fall exactly at 80. The dielectric spectra of 10mM KCl drops below the dielectric constant of water and for

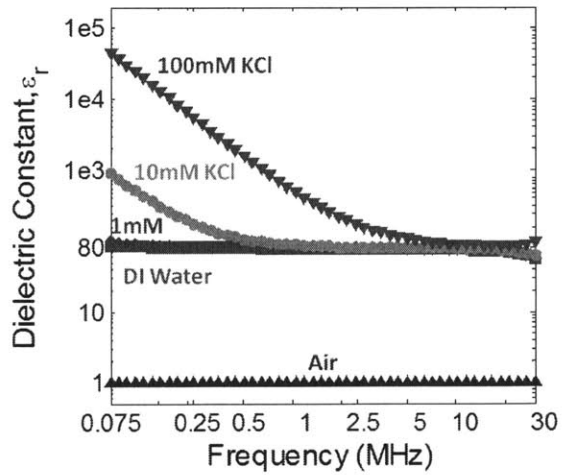
the 100mM KCl solution, the dielectric spectra even drops to negative values at high frequencies. These results are not physical and can be attributed to the growing effects of the series electrode inductance, L_S , as the frequency increases. The residual parallel electrode conductance, G_P , is very low, approximately $\sim 400\text{nS}$ and hence it's effect cannot readily be seen to affect any of the measurements. The series residual electrode resistance, R_S , is measured to be approximately 0.04Ω , and will only significantly affect the resistance measurements of 100mM KCl, which has a resistance of approximately 2Ω . From the air measurements, G_P is measured to be 391.4nS and C_P is 30.6pF . From the 10mM and 100mM KCl solution measurements, R_S is measured to be 0.045Ω and LS is 61.6nH . After correcting for electrode residuals, the resulting dielectric spectra is shown in Figure 4-17(b). From the graph, the spectra of air is now correct at the dielectric constant of air at 1 and the spectra of DI water and the KCL solutions all tend to the dielectric constant of water. Also note the increase in the effects of electrode polarization for increasing concentrations of KCl, which is expected since a larger electrode polarization effect is expected for higher conductivity solutions.

Cell Density

The CHO cell's contribution to capacitance is always empirically determined since there are no robust models and accurately measured physical values to calculate the permittivity of the cell populations suspended in a medium of known conductivity. To calibrate the dielectric spectroscopy measurements to CHO cell density, a high cell density suspension of CHO cells (3.6×10^6 cells/mL) in a chemically defined serum free culture medium, CD CHO from Invitrogen, is taken from a shake flask culture and diluted with fresh CHO medium to obtain the following samples: (A) no dilution, (B) 2:1 dilution, (C) 1:2 dilution and (D) 1:5 dilution with fresh medium. For each sample, the dielectric spectra of the suspension with CHO cells is measured and then centrifuged to removed the cells. The conductivity and the dielectric spectra of the supernatant is also measured. The dielectric spectra of the supernatant will be used for electrode polarization correction via the subtraction method.[14] To remove



(a) Uncorrected measurements: Log-log plot of the dielectric spectra of air(\blacktriangle), DI Water(\blacksquare), 1mM(\lozenge), 10mM(\bullet), and 100mM(\blacktriangledown) KCL solutions without electrode residual corrections



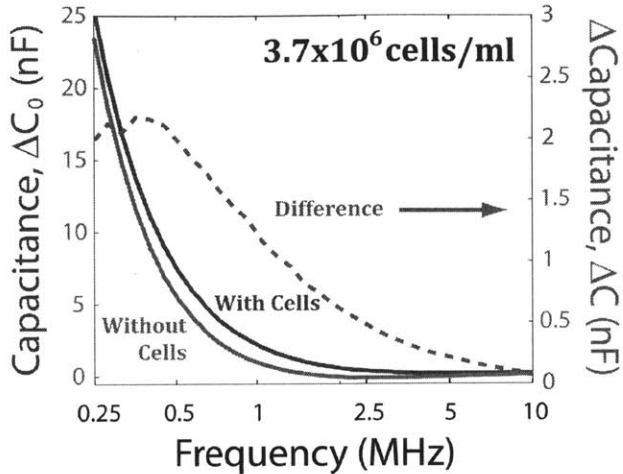
(b) Corrected Measurements: Log-log plot of the dielectric spectra of air(\blacktriangle), DI Water(\blacksquare), 1mM(\lozenge), 10mM(\bullet), and 100mM(\blacktriangledown) KCL solutions with electrode residual corrections

Figure 4-11: Log-log plot of dielectric spectra before and after electrode residuals correction

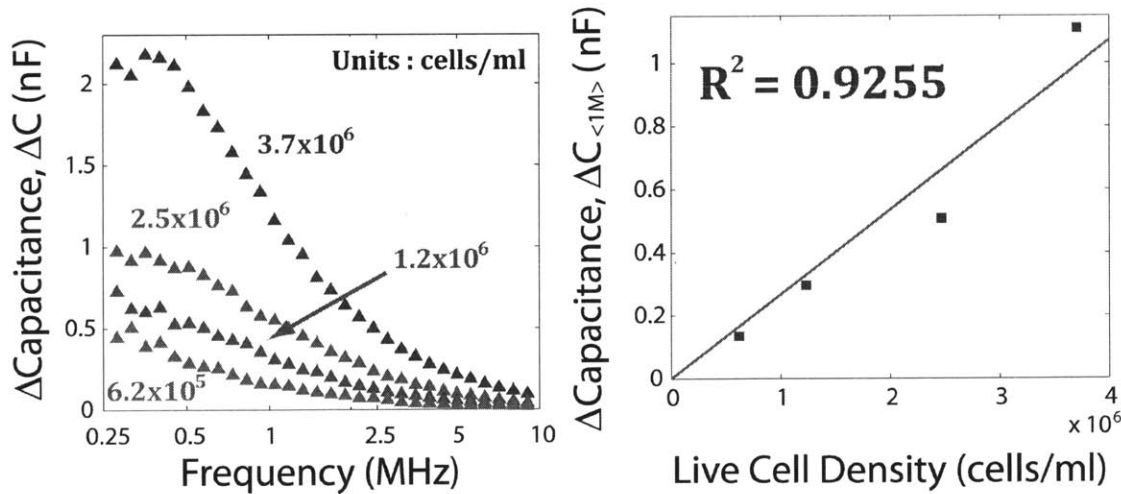
background capacitance, all dielectric spectra are subtracted with the capacitance measurement at the highest frequency, 30MHz, called C_{30M} . The resulting dielectric spectra with the background capacitance, C_{30M} , subtracted will be labeled ΔC_0 .
 $(\Delta C_0 = C - C_{30M})$

To calibrate the Δ Capacitance, ΔC , as a function of CHO cell density, dielectric spectroscopy measurements are performed on 4 samples diluted from 3.6×10^6 cells/mL CHO cell suspension with (A) no dilution, (B) 2:1 dilution, (C) 1:2 dilution and (D) 1:5 dilution with fresh medium. The cells are then centrifuged out and the capacitance spectra of their supernatant is also measured. The capacitance spectra for cell suspension (A) and it's supernatant with the background capacitance, C_{30M} , subtracted, ΔC_o , is plotted on Figure 4-12(a). Since the conductivity of the medium is 13mS/cm, which is close to the conductivity of 100mM KCl solution at 12mS/cm, the effects of electrode polarization is still present for frequencies below 3MHz. The subtraction method for correcting electrode polarization[10] recommends matching the resistance of the supernatant to the low frequency resistance of the suspension before performing a subtraction to remove the effects of electrode polarizations. For cell densities lower than 4×10^6 cells/mL, the difference in resistance between the suspension and supernatant is lower than 2.5%. In this case, a simple subtraction with the spectra of the supernatant should still be an accurate correction of electrode polarization and this corrected spectra is labeled Δ Capacitance, ΔC .

The corrected spectra, ΔC , for samples A-D are shown in Figure 4-12(b). The spectra at frequencies lower than 500kHz will be strongly influenced by electrode polarization and at frequencies higher than 3MHz, the capacitance measured will be at the lower tail of the β - dispersion. Hence, the optimal frequency point for dielectric spectroscopy measurements would be a 400kHz bandwidth around 1MHz. Averaging the DS measurements in this bandwidth, a linear relationship between Δ Capacitance, $\Delta C_{<1M>}$, and viable CHO cell density is obtained and shown in Figure 4-12(c). The correlation between $\Delta C_{<1M>}$ and viable CHO cell density has an R^2 value of 0.9255.



(a) Linear-log plot of capacitance ΔC_0 (with background capacitance C_{30M} subtracted) versus frequency for 3.7×10^6 cells/ml CHO cells in CHO Medium. The difference between the two curves gives the Δ Capacitance, ΔC .



(b) Linear-log plot of the capacitance spectra for samples A (3.7×10^6 cells/ml), B (2.5×10^6 density), C (1.2×10^6 cells/ml) and D (6.2×10^5 cells/ml)

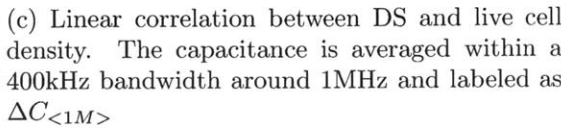


Figure 4-12: Calibration of DS electrodes with CHO Cell Density

4.7.2 Shake Flask Validation

To validate the dielectric spectroscopy electrodes as an online cell viability sensor, the electrodes are used to characterize cell culture aliquots removed daily from a 150mL shake flask culture of CHO cells in the Invitrogen CD CHO, a chemically defined serum free CHO culture medium. CHO cells undergoing different phases of growth starting from lag phase to exponential phase, steady state and subsequently cell death are measured in their original culture medium so that the measurement conditions are as close to online measurements as possible. From the 8mL aliquot removed, 1mL is used for optical density measurements in the Spectronic 20 Genesys, a spectrophotometer from Spectronic Instruments, 1mL is used for offline cell counting by fluorescently staining the cells with the Invitrogen Live/Dead Mammalian Cells Kit and using a hemacytometer to count the cell density by taking images under an Olympus Microscope and performing image analysis using Matlab, 3mL for dielectric spectroscopy measurements on the suspensions with cells and 3mL is to be centrifuged to remove the cells for dielectric spectroscopy measurements on the supernatant for electrode polarization correction. For the offline cell counting, the cells are counted in four quadrants of the hemacytometer and averaged to obtain the live and dead cell density. The shake flask culture ran for 9 days at which most of the CHO cells have died. Daily aliquots are taken from Day 0 to Day 9, providing 10 data points for the entire culture period. Initial characterization of the interdigitated electrode structure is performed using gold interdigitated electrodes patterned on a printed circuit board (PCB) as shown in Figure 4-8.

4.7.3 Subtraction Method

In a real online measurement situation, the spectra of the supernatant is not readily available and furthermore, the changing conductivity of the culture medium due to the metabolism of the cells during the different phases of cell growth further complicates the correction for electrode polarization. The subtraction method[14] recommends subtracting the dielectric spectra of the cell suspension with the dielectric spectra of

the supernatant modified with KCl salts to match the conductivity of the cell suspension at low frequency. This method requires us to extract the supernatant from a cell culture which will require frequent sampling which is not possible for a small volume micro-bioreactors. In order to correct for electrode polarization without the need for extra sampling to obtain the supernatant, the following method is proposed for electrode polarization correction. First, the polarization capacitance of CHO cell culture medium without cells is measured at different days and plotted as a function of the resistance of the medium. This graph is shown in Figure 4-13. The polarization capacitance, $\Delta C_{<1M>}^{pol}$, is defined as the capacitance measured with the background capacitance subtracted and then averaged between a bandwidth of 400kHz around 1MHz. This measurement is repeated for the 4 samples of CHO media extracted from the calibration measurements and also for 100mM KCl solution. From the plots, we can see that all the data points fall around the same curve. This means that polarization capacitance only depends on the resistance of the medium since the relation holds for both CHO cell culture media and KCl solutions. With this calibration graph, from the measured resistance of the cell suspension at low frequencies, the polarization capacitance for a medium with resistance matched to the resistance of the cell suspension can be extracted from this calibration graph and then subtracted from the capacitance measured, $\Delta C_{<1M>}$, to correct for electrode polarization effects.

4.7.4 Results

The interdigitated electrodes are used to measure the live cell density of daily samples taken from a shake flask CHO culture to demonstrate the electrodes' ability to measure cell viability under actual physiological culture conditions. Figure 4-14(a) shows the progression of the live, dead and total cell densities as a function of days for the shake flask culture obtained via cell counting of CHO cells fluorescently stained under an optical microscope. The live cell density curve shows the CHO cells undergoing different phases during growth, lag phase (Day 0-2) when the cells are adjusting to the fresh new medium, exponential growth phase (Day 2-4), stationary phase (Day 4-7) and finally death phase (Day 7-9) when the cells start dying due to insufficient

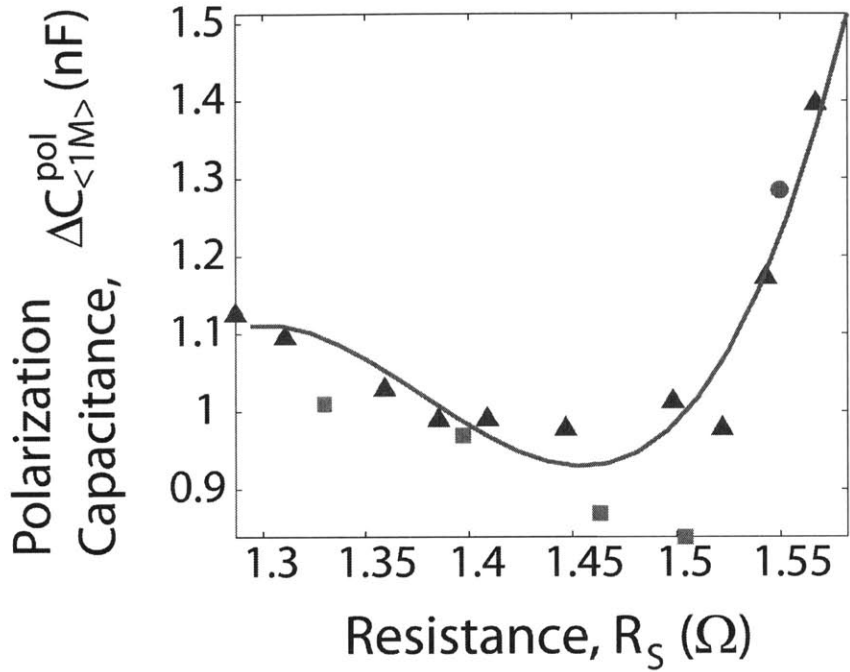


Figure 4-13: Plot of polarization capacitance of the CHO medium corrected for background capacitance and averaged between a 400kHz bandwidth around 1MHz, $\Delta C_{<1MHz>}^{pol}$, with respect to the resistance, R_S , of the medium. This plot consists of all the measurement of the supernatant from the 9 day shake flask culture (\blacktriangle), the supernatant from the 4 dilution samples from the CHO calibration measurement (\blacksquare) and also a data point which correspond to the 100mM KCl solution sample (\bullet). The fitting curve (-) is obtained from fitting a 3^{rd} order polynomial to the data set. From the graph, there seems to be a clear relationship between the resistance measured and the polarization capacitance of an aqueous medium, either a 100mM KCl solution or CHO medium of slightly varying conductivities

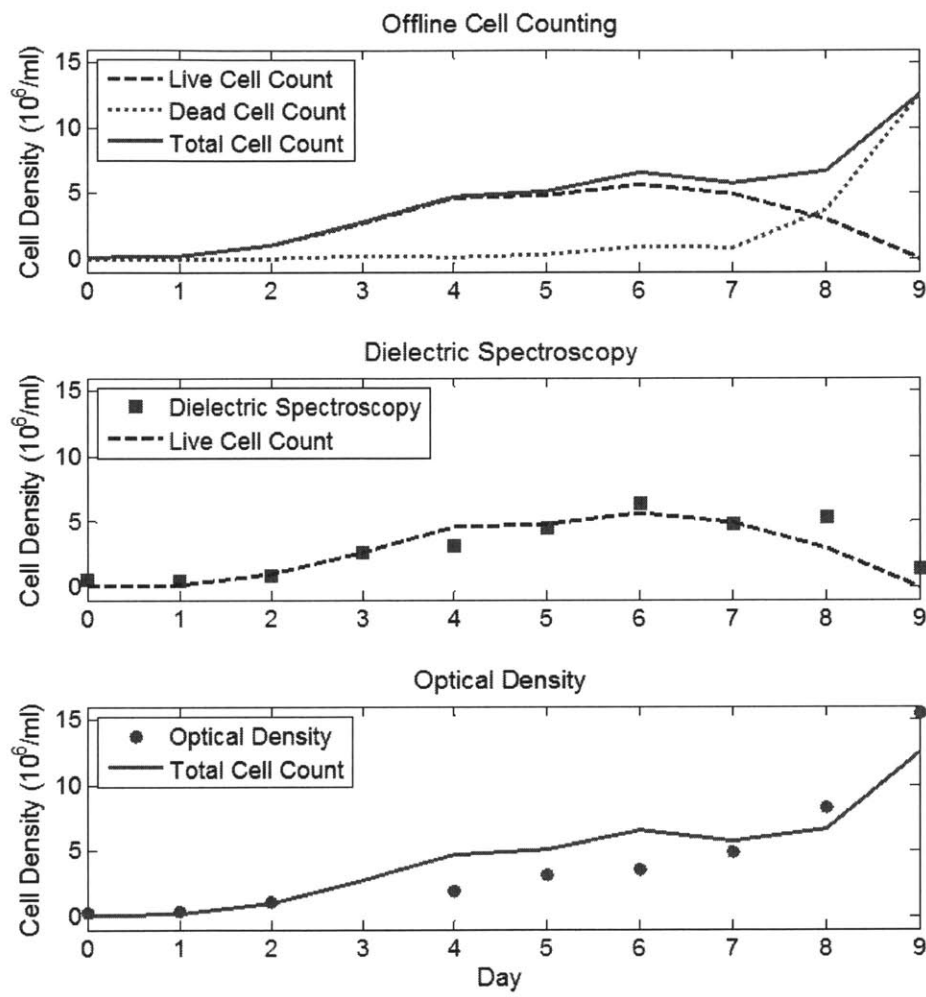


Figure 4-14: (a) Live, dead and total CHO cell densities counted under the microscope, (b) The results of the dielectric spectroscopy measurements compared with offline live cell counting, and (c) optical density measurements compared with off-line total cell counting for the daily samples taken from the shake flask CHO batch cultures

glucose in the medium, which is typical of a batch culture. Figure 4-14(b) shows the dielectric spectroscopy measurements of samples taken daily from the shake flask culture. The live cell density count is also plotted to show how well the dielectric spectroscopy measurements correlate to the live cell density. The correlation between dielectric spectroscopy measurements and live cell density has an R^2 value of 0.7328. Figure 4-14(c) shows the optical density measurement as a function of days. The optical density curve has no correlation with live cell density but follows the total cell density curve very well which is expected of a turbidity based measurements. These results demonstrates the effectiveness of the Large IDES dielectric spectroscopy electrodes as an online cell viability monitoring tool in a micro-environment. However, since the area of these electrodes are rather large \sim 1 inch \times 1 inch, a smaller footprint electrode is desirable for integration into the micro-bioreactor. The next experiment will be performed on the Small IDES electrodes with a different electrode polarization correction method.

4.8 Small IDES Electrode Experiments

In the previous section, the reasons for selecting a particular electrode geometry and material has been discussed, most importantly to minimize the effects of electrode polarization during dielectric spectroscopy measurements. Since electrode polarization cannot be removed completely by electrode design, analytical methods to correct for electrode polarization have also been explored and the CPE model based correction is the most practical correction method for this project since the correction can be performed *in situ*. For the validation of dielectric spectroscopy electrodes, Gold interdigitated electrodes with the dimensions of Small IDES as summarized in Table 4.2 will be used. A photograph of the electrodes and the connection to the LCR meter is shown in Figure 4-15. In order to perform an accurate measurement, first the cell constant of the interdigitated electrodes need to be experimentally determined. This is done in combination with the correction for the electric residuals of the electrodes described in the next section. After performing the electrode residual correction and

determining the cell constant of the electrodes, dielectric properties can now be obtained but the data still contains electrode polarization effects. The next section deals with the data analysis to remove electrode polarization effects by using the Nyquist Plot to extract out parameters of the CPE model. The experimental protocol for the biological validation is then described in the next section. Subsequently, a set of experiments determining when the electrical double layer (EDL) is stable enough to be described by the CPE model is described. The results are then discussed and concluded at the end of this chapter.

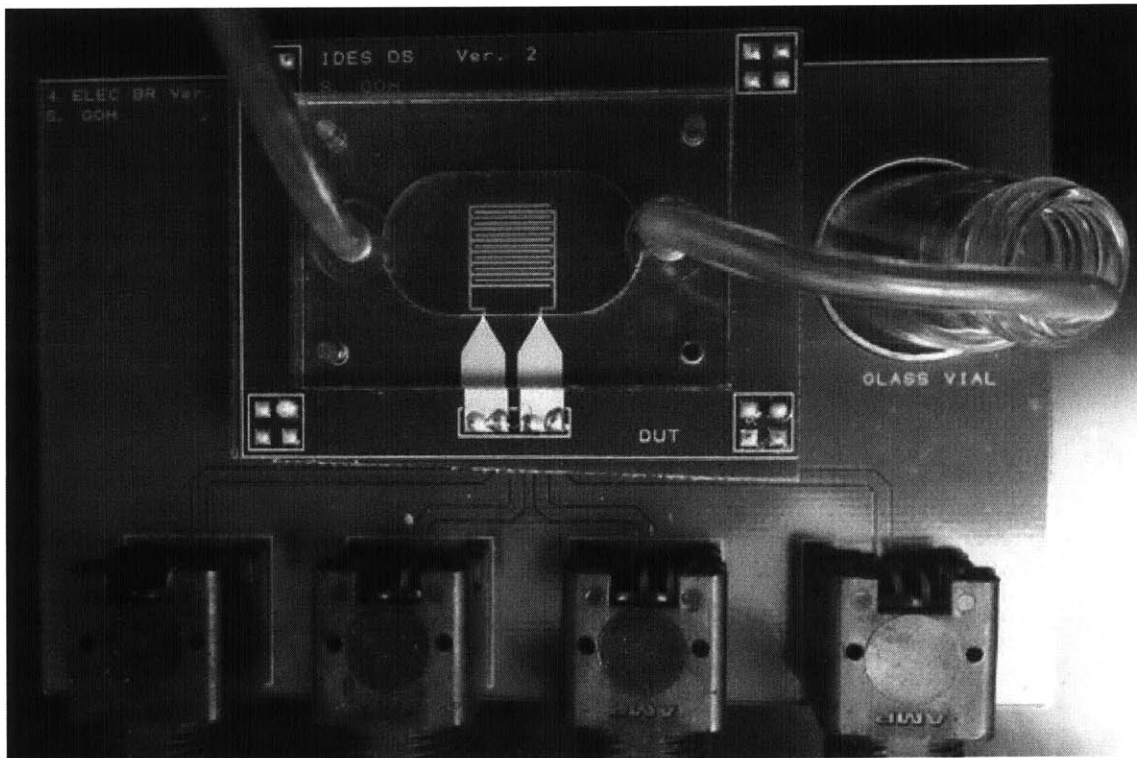


Figure 4-15: Photograph of Gold interdigitated DS electrodes on printed circuit board (PCB) with a polycarbonate measurement chamber, machined in the lab. A supporting PCB board is designed to convert the 4 point measurement of the LCR meter to the 2 point measurement required by the interdigitated electrodes with a holder for the glass vial.

4.8.1 Calibration

Cell Constant

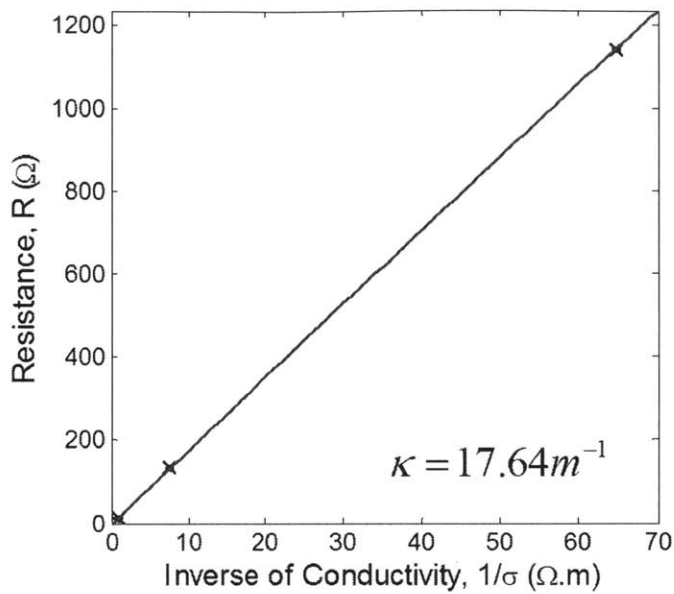
The results of the calibration with 1mM, 10mM and 100mM KCl solution is shown in Figure 4-16. The cell constant, κ , of the electrodes is measured to be 17.64m^{-1} , which is smaller than the theoretical value of 21.63m^{-1} . In the theoretical model, edge effects have been ignored. Hence, the cell constant calculated will be higher than the actual cell constant since the additional edge effects will result in a lower value of the cell constant, i.e. a higher value of capacitance measured. The cell constant calibration with resistance is performed at lower frequencies, from 75kHz to 5MHz, because at higher frequencies the resistance will be affected by residual inductances in the electrode system. After the cell constant is determined for the electrodes, the resistance and capacitance that is expected for air, DI water and KCl solutions of different molarities are now known and can be used to correct for electrode residuals.

Electrode Residuals

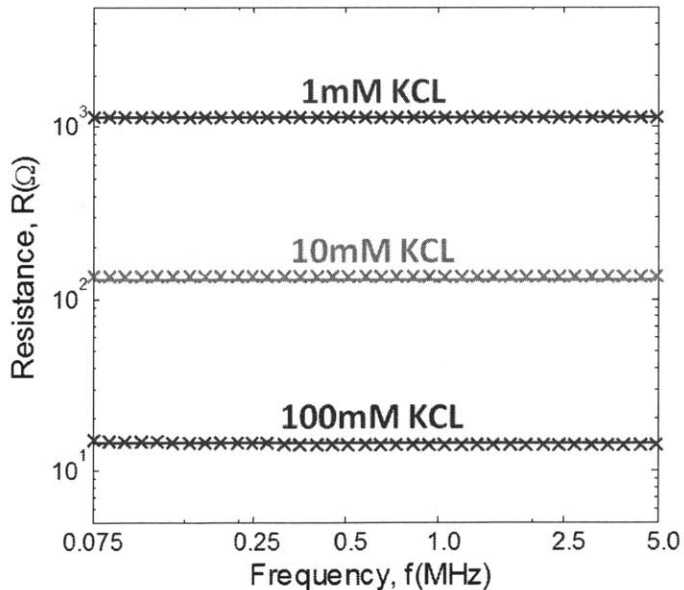
When the electrodes are used to measure the dielectric spectra of Air, DI water, 1mM, 10mM and 100mM KCl solutions without correcting for electrode residuals, the results are as shown in Figure 4-17(a). The capacitance spectra is converted to dielectric constant using the experimentally determined cell constant, $\kappa = 17.64\text{m}^{-1}$. For the residual correction this time around, instead of trying to find G_p and C_p exactly(Refer to Figure 4-10) the general admittance, $Y_P(w)$, is determined from the open correction measurement with air as the measurement sample. From Equation 4.9, we can calculate $Y_P(w)$ from the measured impedance, Z_{MEAS} and the actual impedance of air $Z_{SAMPLE}(w) = Z_{AIR}(w) = 1/(jwC_{AIR})$. Rearranging the equation gives the following relation:

$$Y_P(w) = \frac{1}{Z_{MEAS}(w)} - \frac{1}{Z_{AIR}(w)} \quad (4.11)$$

The series electrode residual electrode resistance, R_S , and inductance, L_S , is determined using the same method as the Large IDES experiments. From the 10mM and

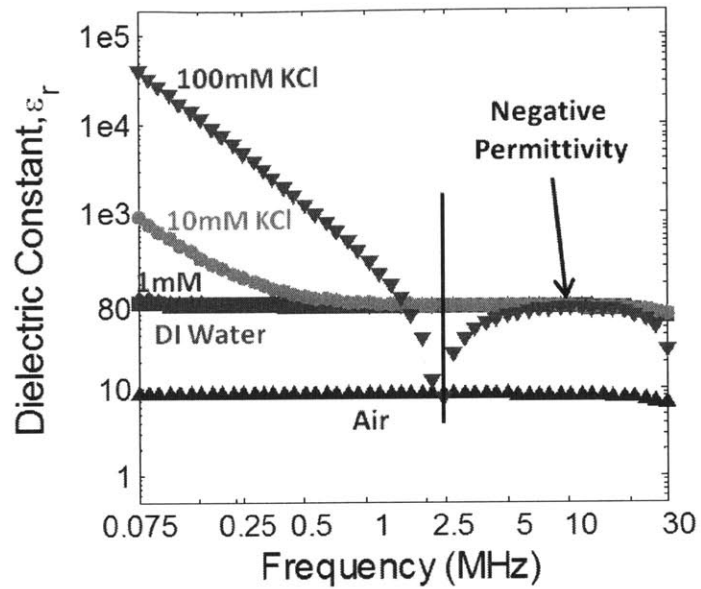


(a) The linear relationship between R and $1/\sigma$, data (\times) and fitting curve (-). The calibrated cell constant, κ , is 17.64 m^{-1} . The error bars in this plot are calculated from the standard deviation from the measurement over a frequency range between 75kHz to 5MHz. The error bars are smaller than the marker size in this plot.

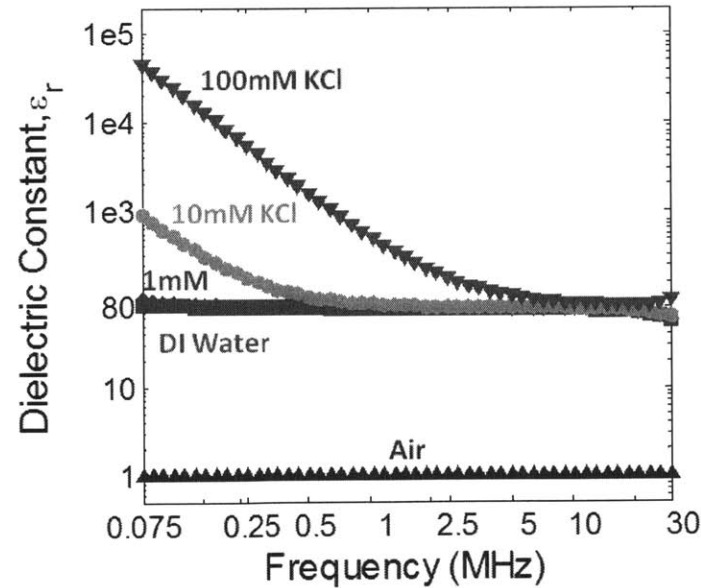


(b) Measurement data(\times) and fitting curve (-) using the calibrated value of the cell constant

Figure 4-16: Calibration of electrode cell constant with 1mM, 10mM and 100mM KCl solutions



(a) Uncorrected measurements: Log-log plot of the dielectric spectra of air(\blacktriangle), DI Water(\blacksquare), 1mM(\diamond), 10mM(\bullet), and 100mM(\blacktriangledown) KCL solutions without electrode residual corrections



(b) Corrected Measurements: Log-log plot of the dielectric spectra of air(\blacktriangle), DI Water(\blacksquare), 1mM(\diamond), 10mM(\bullet), and 100mM(\blacktriangledown) KCL solutions with electrode residual corrections

Figure 4-17: Log-log plot of dielectric spectra before and after electrode residuals correction

100mM KCl solution measurements, R_S is measured to be 0.85Ω and L_S is 1.5nH . After correcting for electrode residuals, the resulting dielectric spectra is shown in Figure 4-17(b). From the graph, the spectra of air is now correct at the dielectric constant of air at 1 and the spectra of DI water and the KCL solutions all tend to the dielectric constant of water. Also note the increase in the effects of electrode polarization for increasing concentrations of KCl, which is expected since a larger electrode polarization effect is expected for higher conductivity solutions.

4.8.2 Data Analysis

Section 4.5.2 describes a method for correcting the electrode polarization parasitics from the measurement spectra by using an empirical model known as the CPE Model, whose impedance is given by the following equation:

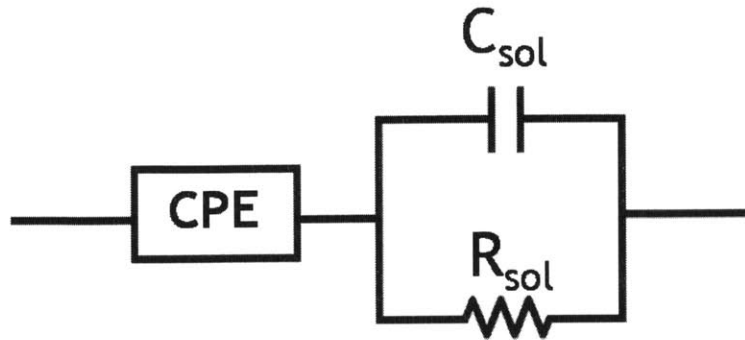
$$Z_{pol} = \frac{1}{Y_o(jw)^\alpha} \quad (4.12)$$

where Y_o and α are fitting parameters to fit the electrode polarization spectra at low frequencies. Extracting these parameters from a plot of capacitance and resistance versus frequency as illustrated in Figure 4-4 will be difficult. It is more useful to represent the data in another form, known as the Nyquist Plot, where the constant phase element (CPE) forms a straight line with a slope that depends on α .

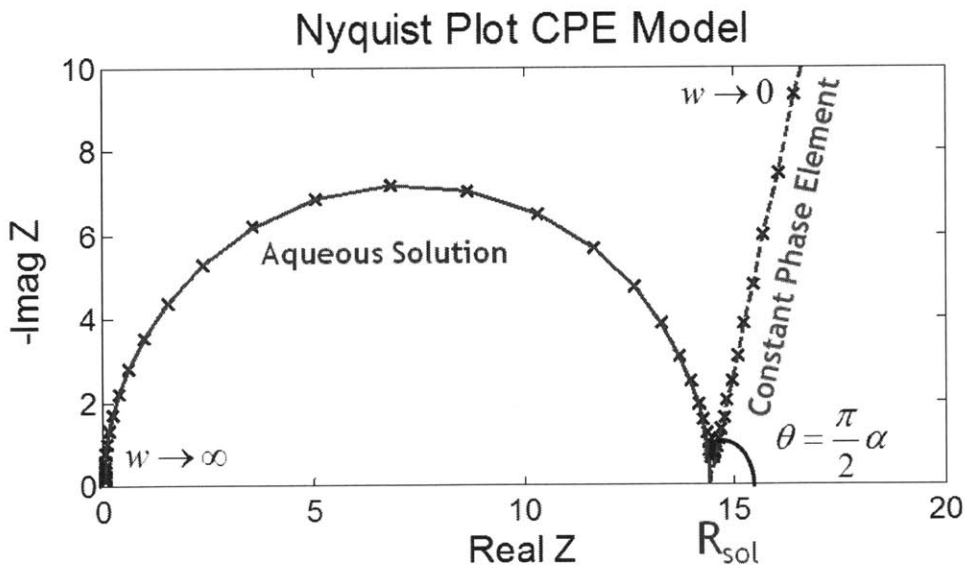
Nyquist Plots

The Nyquist Plot is a parametric plot of ω where the real part of a complex equation ($Re\{Z(w)\}$) is plotted on the X-axis and the negative of the imaginary part ($-Im\{Z(w)\}$) is plotted on the Y-axis. For simple systems like a resistor, which has an impedance ($Z = R$) that is independent of frequency, the Nyquist plot of a resistor, R , is just a dot on the X-axis with a value equal to R . For a capacitor, where $Z = (j\omega C)^{-1}$, the Nyquist plot is a line that starts from the origin ($\omega \rightarrow \infty$) that goes up straight to infinity ($\omega \rightarrow 0$).

The impedance for an aqueous medium with a CPE model for the electrode po-



(a) Equivalent Circuit Model for the CPE Model of Electrode Polarization in series with a parallel RC circuit representing the impedance of an aqueous solution, where R_{sol} is the resistance of the solution(a measure of conductivity) and C_{sol} is related to the permittivity of the solution, which is just the dielectric constant of water.



(b) Nyquist Plot for the CPE Model.

Figure 4-18: Equivalent Circuit and Nyquist Plot for the CPE Model in series with the parallel RC model of an aqueous solution. The parallel RC circuit is represented by a semicircle in the Nyquist plot approaching zero as $\omega \rightarrow \infty$. The Constant Phase Element (CPE) model is represented by a line with a slope at an angle $\theta = (\pi/2)\alpha$ that goes to infinity as $\omega \rightarrow 0$

larization is shown in Figure 4-18(a), where R_{sol} is a measure of the conductivity of the medium and C_{sol} is a measure of the medium permittivity, which is just the permittivity of water. The Nyquist representation of the equivalent circuit is shown in Figure 4-18(b). The parallel R-C circuit has an impedance of:

$$Z = \frac{R_{sol}}{1 + jwR_{sol}C_{sol}} \quad (4.13)$$

which is represented by a semicircle in a Nyquist plot, approaching R_{sol} as $\omega \rightarrow 0$, 0 as $\omega \rightarrow \infty$, and $R_{sol}(1 + j)$ for $\omega \sim 1/R_{sol}C_{sol}$. As for the CPE element, whose impedance is shown in Equation 4.12, the real and imaginary components are as follows:

$$Z_{pol} = \frac{1}{Y_0\omega^\alpha} (\cos(\pi\alpha/2) - j\sin(\pi\alpha/2)) \quad (4.14)$$

Hence, the slope of the Nyquist plot for the CPE model is given by $(\pi/2)\alpha$ and starting from the origin for $\omega \rightarrow \infty$ to infinity for $\omega \rightarrow 0$. The CPE model and the parallel RC model combined in series results in a Nyquist Plot that looks like Figure 4-18(b) where now the intersection between the two plots occurs at R_{sol} . The Nyquist plot has 2 immediate advantages: (1) the slope of the straight line gives the value of α and (2) the intersect of the straight line with the X-axis gives the value of R_{sol} .

4.8.3 Results

Stability of the Electrical Double Layer

During the preliminary set of measurements, it is observed that there were great variations in the measurements taken at different times, where only in some cases the CPE model fits the electrode polarization curve. The stability of the electrical double layer during measurements is then examined. First, the measurements on the first day were very different from subsequent days. Further examination showed that the electrodes need to be pre-conditioned before measurement by hydrating the electrodes for 24 hours before taking a measurement. The variations in the electrode polarization

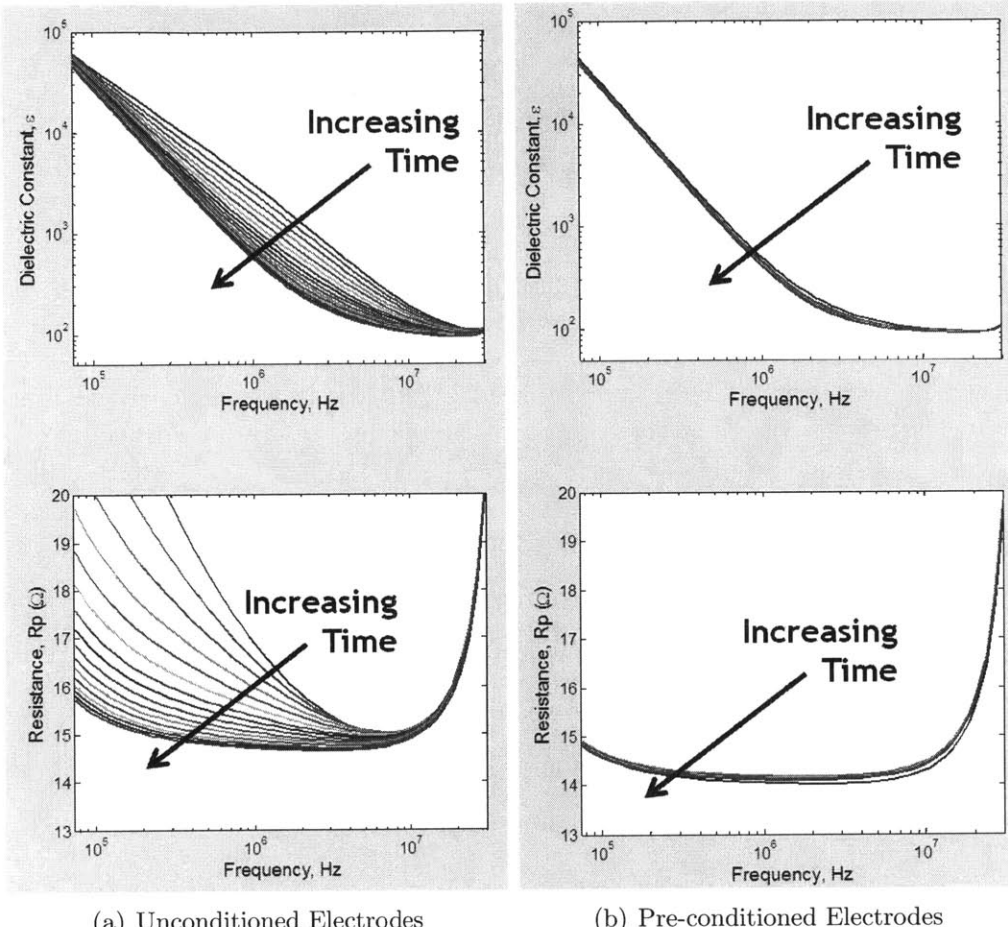


Figure 4-19: Fresh CD CHO medium without cells were measured every 5 minutes (a) with unconditioned electrodes and (b) with pre-conditioned (soaked in DI water for 24 hours prior to measurement) electrodes. The large variation in spectra for the unconditioned electrodes shows that the electrodes need to be hydrated overnight before performing any Dielectric Spectroscopy measurements to ensure the formation of a stable EDL.

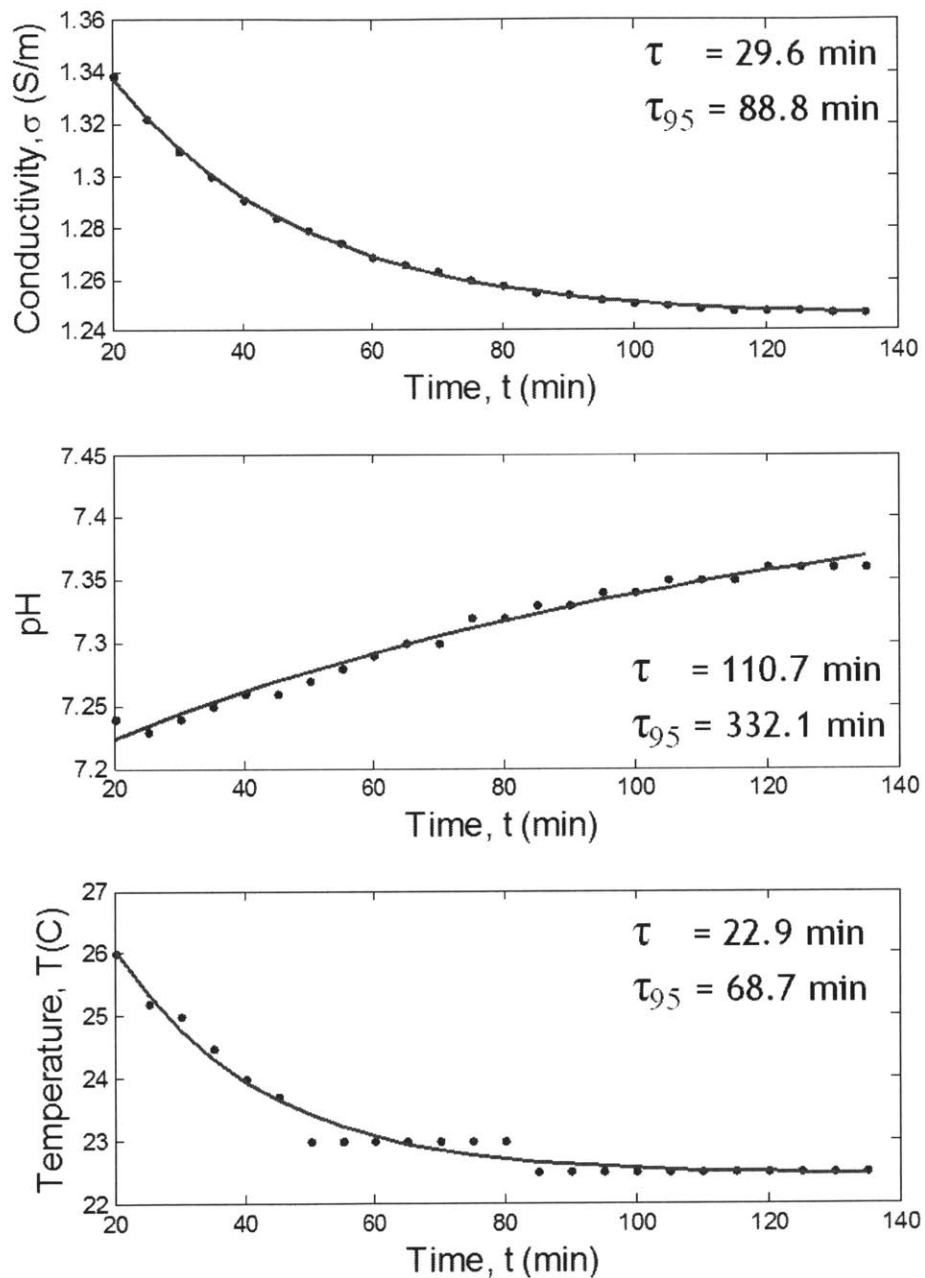


Figure 4-20: The graph shows the time it for the temperature, pH and conductivity to stabilize after removing the sample from the CO_2 incubator for dielectric spectroscopy measurements. Measurements performed in a beaker.

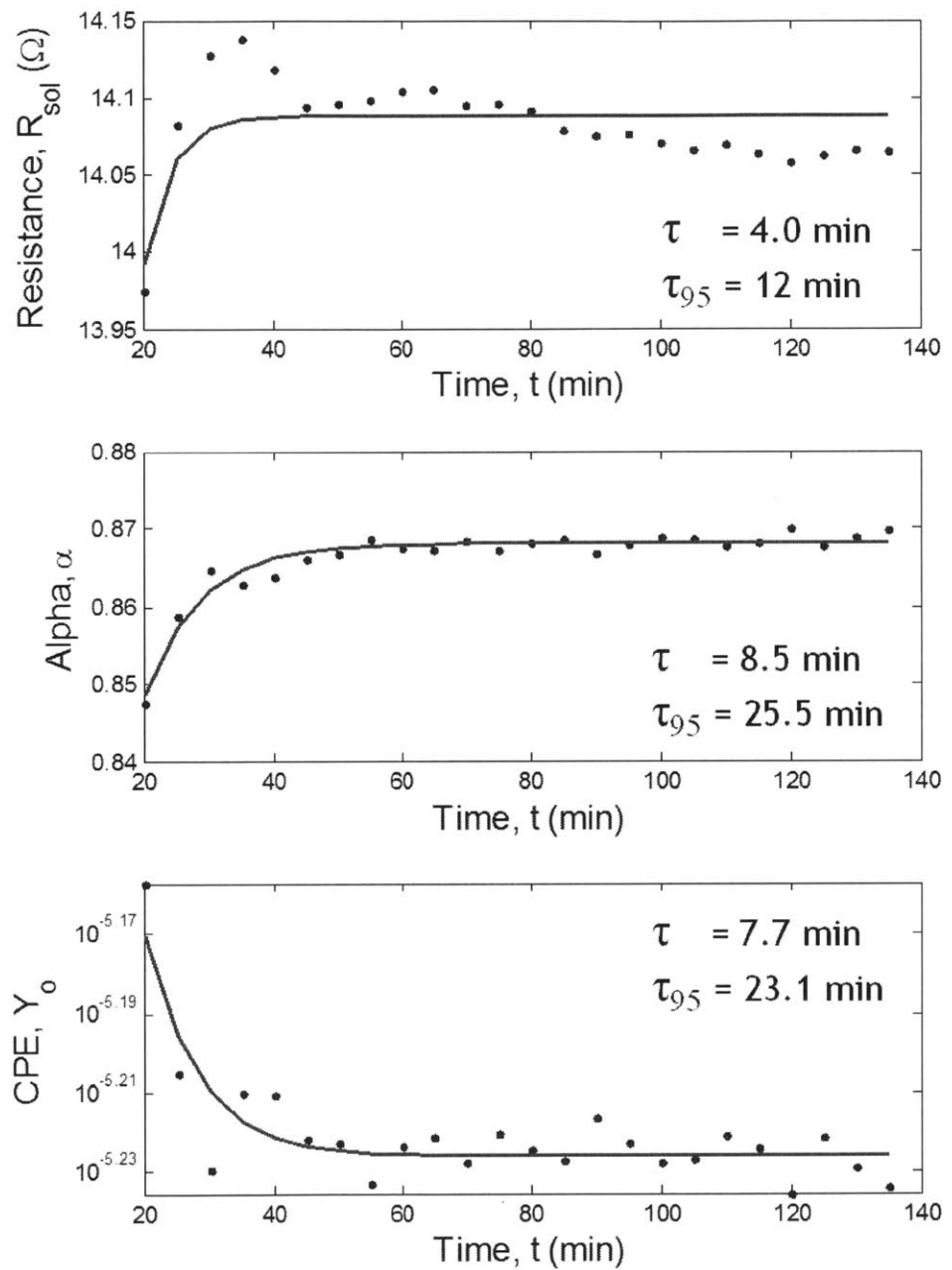


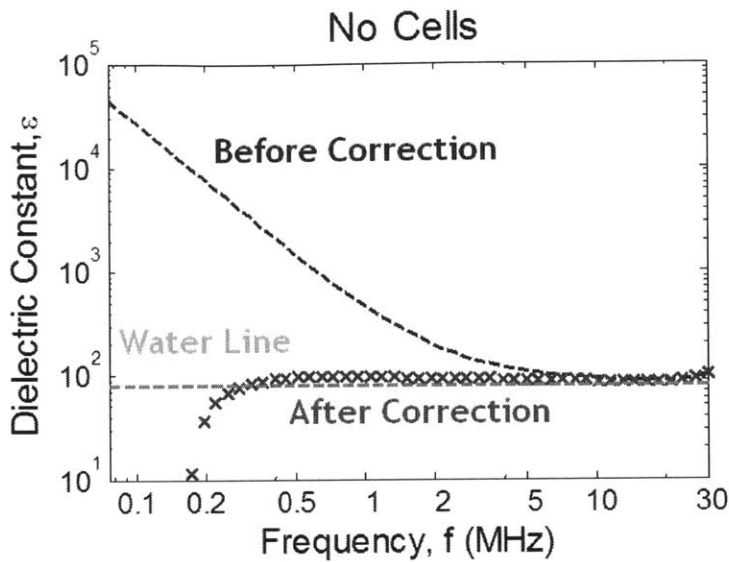
Figure 4-21: After inserting the measurement sample into the Dielectric Spectroscopy measurement chamber, the sample takes ~ 30 minutes to equilibrate.

curve for fresh CHO medium without cells is shown in Figure 4-19. Measurements were made every 5 minutes. As time increases, the curve converges into a single curve for the unconditioned electrodes, as shown in Figure 4-19(a). If the electrodes have been hydrated for 24 hours before measurement, the variations in the curve are no longer observed, results shown in Figure 4-19(b).

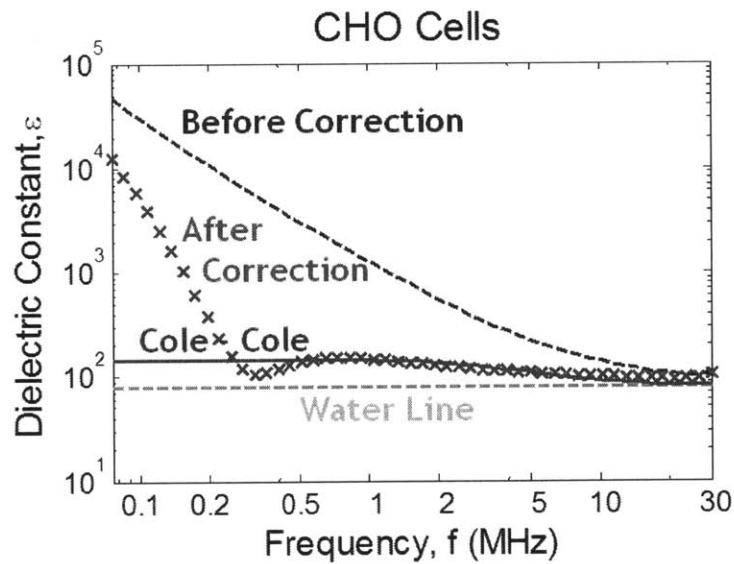
The second variation arises from the fact that the samples are removed from a 37°C 5% CO₂ incubator to the measurement setup which is at room temperature and atmospheric CO₂. Conductivity will be affected by temperature since the diffusivity and mobility of ions are temperature dependent. Moreover the differing CO₂ partial pressure in the air will affect the bicarbonate buffer in the medium and change the pH and conductivity of the medium. Since electrode polarization effects are dependent on the conductivity of the medium, having a stable conductivity is crucial to having a stable measurement curve. The results of how the sample conductivity, temperature and pH changes as a function of time is shown in Figure 4-20. This experiment is performed in a beaker and hence the temperature drop is related to the rate of temperature drop for that geometry. Repeating the same measurement in the measurement chamber, the temperature and conductivity stabilizes more rapidly because of the larger surface to volume ratio and within 30 minutes a stable CPE model can be obtained, results shown in Figure 4-21.

Validation of CPE Correction

To validate the CPE model, the model is applied to correct spectra for fresh CHO medium without cells and a CHO cell suspension. After obtaining the parameters, Y_o , α , and R_{sol} from the Nyquist plot, the parameters are inserted back into the equivalent circuit model and then the CPE component is subtracted out from the spectra to obtain the electrode polarization free spectra. The spectra before and after correction for the CHO medium without cells is shown in Figure 4-22(a). The water line is shown in both graphs to indicate the position of the permittivity of water. Without cells, the permittivity after correction for CHO medium should fall on the water line as shown in the right plot. However, at low frequencies the permitivity



(a) The spectra of CHO medium without cells



(b) The spectra of a CHO suspension

Figure 4-22: The CPE correction performed on (a) fresh CHO Medium without cells and (b) a CHO cell culture suspension. The water line is a line marking the dielectric constant of water. (a) For the fresh CHO medium, after CPE correction the spectra should fall on the water line since the permittivity of CHO medium should just be the permittivity of water. The spectra flattens out and falls on the water line as predicted. However, the CPE model only holds for a particular frequency range and hence at very low frequencies, the permittivity drops below the water line. (b) After CPE correction, the dispersion of the live cells are revealed and shown in the figure on the right. A Cole-Cole model is then fitted to the dispersion curve to obtain the $\Delta\epsilon$ that is linearly related to the viable cell density in the culture.

drops off because the CPE model is only valid for a limited frequency range. Since this range is in the relevant range for the β -dispersion, this correction should be able to elucidate the dispersion behavior that is necessary for the dielectric spectroscopy measurements.

The before and after correction spectra of the measurements with CHO cells are shown in Figure 4-22(b). The spectra before correction looks almost similar to that of the CHO medium without cells but after correction, there is a dispersion that is due to the presence of live cells in the medium above the water line. This dispersion fits the Cole-Cole Model (Equation 4.2) and the value of $\Delta\epsilon = (\epsilon_s - \epsilon_\infty)$ can be obtained from the fit. Note that the α in this equation is unrelated to the α in the CPE model. Recall that $\Delta\epsilon$ is related to the live cell density according to Equation 4.3.

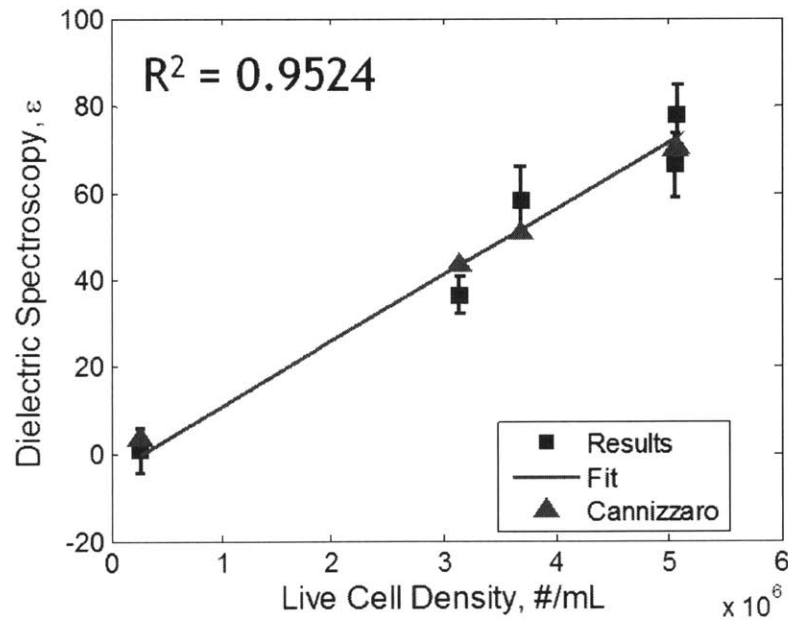


Figure 4-23: Dielectric Spectroscopy validation with live cell density. The author's results are shown in blue squares (\square). An R^2 value of 0.9524 is obtained for the fit. Values from literature, dielectric spectroscopy measured on CHO cells using large commercial Aber Probes is shown as red triangles (\triangle). The results match quantitatively to literature values.

After performing the correction on all the measurement spectra, a linear relationship between $\Delta\epsilon$ and live cell density is obtained, shown in Figure 4-23. The linear

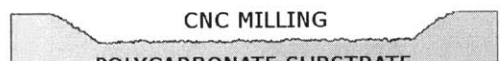
fit has an R^2 value of 0.9524. Cannizzaro et al. performed dielectric spectroscopy measurements on CHO cells using the commercial Aber Probe in a large bioreactor. The results from that paper are also plotted on the same graph. Comparing our results to theirs, the dielectric spectroscopy measured using the gold interdigitated electrodes matches quantitatively with dielectric spectroscopy measurements on large systems.

4.9 Fabrication of Platinum Electrodes on Polycarbonate

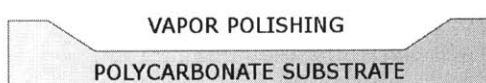
The interdigitated electrodes are fabricated on polycarbonate sheets by sputtering platinum (Pt) through a shadow mask as shown in Figure 4-24. First, a growth well is patterned out of a flat sheet of polycarbonate using a CNC milling machine. After CNC machining, the machined surfaces are rough and optically matte. To obtain optically clear surfaces, the polycarbonate sheet is vapor polished with Methylene Chloride, a solvent of polycarbonate, using the method described in the paper by our group member, Kevin Lee.[38] Since the features of our growth chamber in a microfluidic device is typically much deeper than etched trenches on a silicon wafer, conventional methods of using photoresist as a mask for the deposition of metal cannot be employed since it would be challenging to spin a uniform layer of photoresist on surfaces with deep trenches. Fortunately, stainless steel shadow masks patterned using lasers have a high enough resolution for our interdigitated electrodes. Since metal sheet masks are supported from the sides and not by the substrate like photoresists, an interdigitated pattern requires two shadow masks, one for the horizontal lines and a second one for the vertical lines. To hold the flat metal mask in place, a polycarbonate mask holder is machined using CNC machining. The metal deposition is performed using an AJA International Orion 5 sputtering machine. A titanium (Ti) layer is sputtered first as an adhesion layer at slow deposition rate of 0.5 /sec till a thickness of 10nm is achieved. Following that, a 150nm thick layer of Platinum



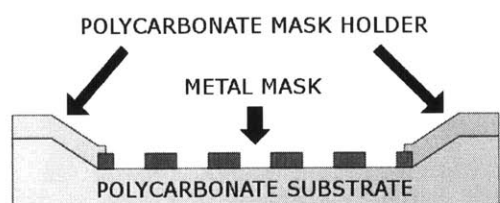
(a) Flat polycarbonate sheet



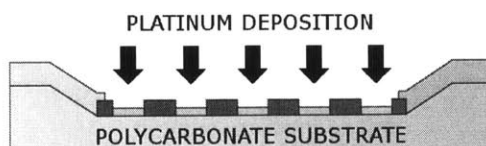
(b) CNC Milling of growth well chamber



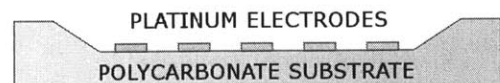
(c) Vapor polishing to obtain optically clear surfaces



(d) Laser patterned metal mask held by polycarbonate mask holders are used as shadow masks



(e) Platinum metal is sputtered onto the polycarbonate sheet



(f) After removing the mask, platinum interdigitated electrodes are left

Figure 4-24: Step by step description of the process of patterning platinum interdigitated electrodes on a polycarbonate substrate via shadow masking in a sputtering machine.

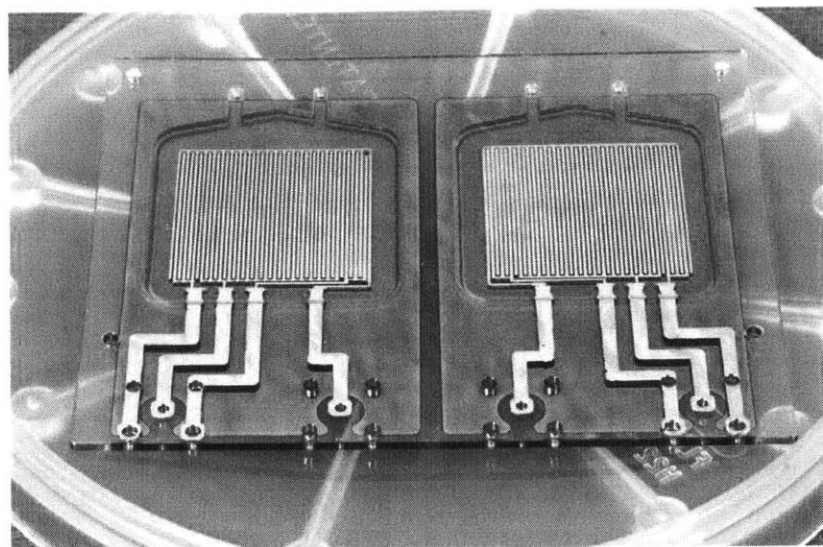


Figure 4-25: Actual picture of platinum interdigitated electrodes (Large IDES) sputtered on polycarbonate substrate. Polycarbonate substrate remains flat after deposition

(Pt) is deposited at a rate of 1 /sec. The deposition step is repeated for the second mask. The slow deposition rate is important to prevent the polycarbonate sheet heating up and deforming from the energy transferred by the sputtered ions. The final polycarbonate substrate shown in Figure 4-25 for Large IDES remains flat and shows no deformation after deposition.

The same deposition method is utilized for depositing the Small IDES structure on polycarbonate. A photograph of the two types of metal stencils, thin (0.002 in = 0.051 mm thick) and thick (0.015 in = 0.381 mm thick) is shown in Figure 4-26. A polycarbonate (PC) stencil is also used to clamp the stencils down for both the thin and thick metal stencil. The sputtered electrodes for the small IDES structure is shown in Figure 4-27. From Table 4.3, the thicker metal stencils gave more consistent results when the resistance across the two electrodes are measured. The thin electrodes are too flimsy and may not be able to separate the two electrodes completely even after being clamped down by the polycarbonate stencil.

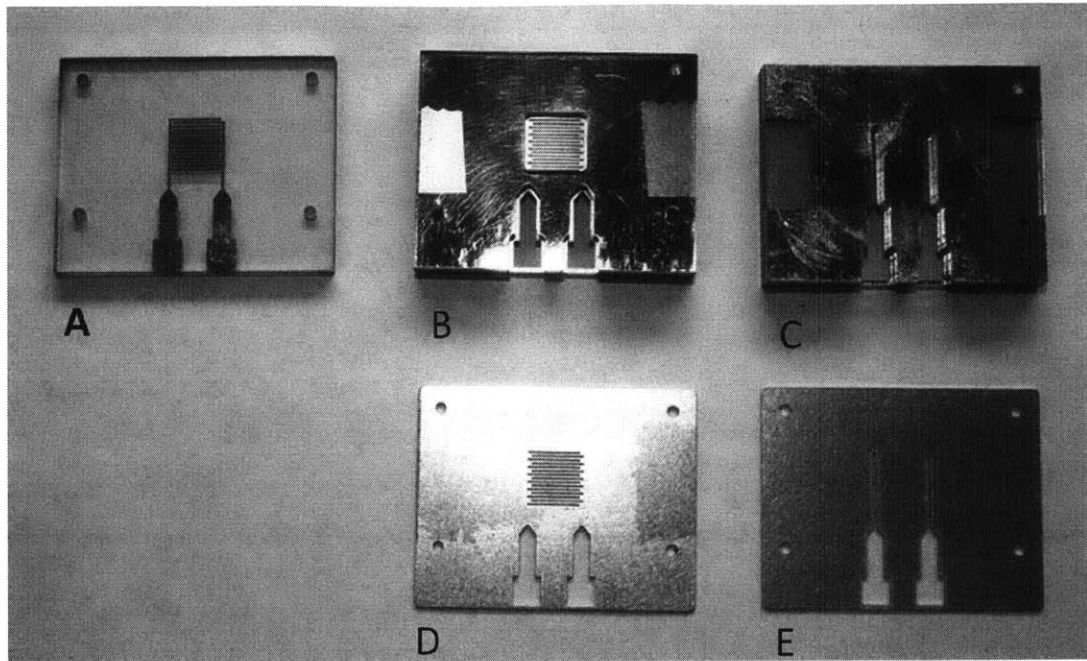


Figure 4-26: Photograph of the stencils that is used as a mask for sputtering Platinum electrodes (Small IDES). (A) The final sputtered electrode, (B) Polycarbonate (PC) stencil + thin metal stencil (0.002 in = 0.051 mm thick) for the horizontal lines, (C) Polycarbonate (PC) stencil + thin metal stencil (0.002 in = 0.051 mm thick) for the vertical lines, (D) Thick metal stencil (0.015 in = 0.381 mm thick) for the horizontal lines (used with PC stencils to clamp the stencil onto the substrate) and (E) Thick metal stencil (0.015 in = 0.381 mm thick) for the vertical lines (used with PC stencils to clamp the stencil onto the substrate)

Table 4.3: Resistance between Platinum electrodes (Small IDES) sputtered on Platinum for using stencils of different thickness

No	Stencil	Material	Resistance
1	Thin	150nm Pt/10nm Ti	3 MΩ
2	Thin	150nm Pt/10nm Ti	6 MΩ
3	Thin	150nm Pt/10nm Ti	25 MΩ
4	Thin	150nm Pt/10nm Ti	Overload
5	Thick	150nm Pt/10nm Ti	5 MΩ
6	Thick	150nm Pt/10nm Ti	Overload
7	Thick	150nm Pt/10nm Ti	Overload

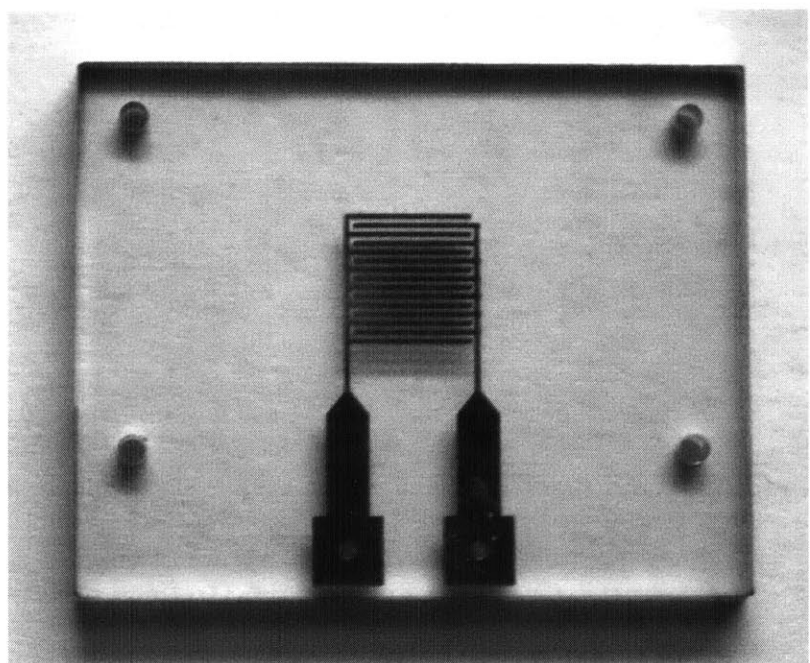


Figure 4-27: Actual picture of platinum interdigitated electrodes (Small IDES) sputtered on polycarbonate substrate. Polycarbonate substrate remains flat after deposition

4.10 Conclusions

The Small IDES electrodes with the CPE correction method resulted in results that is quantitatively comparable to experiments on CHO cells found in literature. The results shows that the author has successfully miniaturized a dielectric spectroscopy probe for micro-bioreactors for high conductivity CHO medium with a correction method that can be applied *in situ* for Gold interdigitated electrodes. The fact that the permittivity matches large scale dielectric spectroscopy measurements on the same type of cells, CHO, means that the CPE correction is successful in removing all traces of the parasitic electrode polarization. A shadow mask fabrication process has also been developed to deposit Platinum on polycarbonate substrates. Platinum is sputtered onto polycarbonate at a very slow deposition rate to prevent overheating of the thermoplastic which may cause the plastic to deform. The sputtered metal passes the electrical tests but fails the peel test. Further experiments to improve on the adhesion of Platinum electrodes on polycarbonate will need to be performed. Since gold electrodes have been shown to work for dielectric spectroscopy measurements for cell culture media with high conductivity, the next step would include developing a fabrication process to deposit Gold electrodes on polycarbonate substrates.

Chapter 5

Conclusions and Future Work

The objective of this thesis is to design a micro-bioreactor for Chinese Hamster Ovary(CHO) cell culture. These CHO cells are used in biopharmaceutical industries to produce recombinant monoclonal antibodies to be injected into human patients as therapies for cancer, organ transplant rejection, HIV and etc. This project is carried out in close collaboration with the project sponsor, Sanofi, Germany, a biopharmaceutical company with recombinant CHO cells (r-cho) in their production line. Working closely with the potential end users of the technology being developed, accelerates the process of narrowing in on the specifications and requirements of the design of the micro-bioreactor. In our discussions, there were also some requirements, like compatibility with the industry's current offline analytical tools, that weren't considered initially in the design. It turns out to be an important criteria for the adoption and integration of this technology in the company's process flow without incurring large changes in their supporting infrastructure. Having a definite set of requirements for the design of the micro-bioreactor has the advantage that it reduces the uncertainty of design goals. Yet, this also means that the micro-bioreactor design has a more stringent set of requirements to meet and not all of the physical requirements are completely independent of each other, which adds to the complexity of the problem.

In order for the RECA Micro-bioreactor to be a suitable platform as a high throughput small scale model of industrial bioreactors for CHO cell culture, it must

first be able to culture CHO cells. Since CHO cells are physiologically very different from bacteria or yeast cells, one of the challenges is that the micro-bioreactor must be able to deliver all the necessary nutrients to the CHO cells with a mixing rate that does not cause cell death either through apoptosis or necrosis. On top of that, to be an exact small scale model of large bioreactors, it is not sufficient that the micro-bioreactor is able to culture CHO cells but it has to culture CHO cells in the exact the same way that the larger bioreactors culture CHO cells. In other words, all the physical characteristics of the micro-bioreactor must match those of large bioreactors.

In designing the RECA Micro-bioreactor, since the gas transfer rate and shear stress are both functions of the mixing rate, it is an important design strategy to try to decouple these effects to be able to control each parameter independently. The shear stress is decoupled from the mixing rate by making the air resistance lines the limiting factor that determines the deflection time of the membrane. The flow resistance of water through the channels between the growth chambers should have minimal effect on the deflection time and hence can be optimized to match the maximum shear stress seen in large bioreactors without affecting the mixing time. Secondly, from the theoretical estimates of the gas transfer rates with no mixing, pure diffusion mechanism of the gas for both oxygen and CO₂ through the PDMS membrane and water has the k_{La} that matches sufficiently well with large bioreactors. A rational design strategy would be to reduce the mixing rate to be slow enough as to not increase the mobility of the gas species in the culture medium and yet generate a fast enough mixing to meet the mixing times of larger bioreactors. From Table 3.5, the design of the RECA Micro-bioreactor in this thesis have achieved the physical parameters that matches the physical parameters of the large bioreactors.

Besides having equivalent physical environment for the cells, the functionality of the micro-bioreactor must also include the same level of control and monitoring of physical and chemical parameters in the growth chamber as bench top bioreactors. In the RECA Micro-bioreactor, temperature, pH, dissolved oxygen and carbon dioxide levels are monitored in real-time, similar to bench top bioreactors. The new CO₂ sensor has been calibrated and optimized to perform at the highest sensitivity in the

range of interest. In addition, these parameters are also controlled by modulating the current of the heater coil (temperature), changing the switching rate of the gas control valves to independently control the partial pressures of oxygen and CO₂ in the headspace, and automated base additions for pH control. The design of the RECA Micro-bioreactor has already incorporated all these control mechanisms. The only unvalidated control mechanism is the pH control using automated gas switching and automated liquid additions, which will be part of a future work for this project due to time constraints. This future work will be carried out by the author of this thesis.

In distinction to the bench top bioreactor, the micro-bioreactor, having a very different geometrical form and mixing mechanism, can accommodate other sensors that are not typically present in larger bioreactors. An optical density(OD) sensor can track cell growth in real time, is typically not present in large bioreactors because the presence of bubbles in large bioreactors interferes with OD measurements. The larger bioreactors, having a low surface to volume ratio, requires sparging of gasses into the growth chamber to provide sufficient gas transfer rate($k_{L}a$) to provide oxygen and CO₂ to the cells. This problem is intrinsically non-existent to micro-bioreactors with their large surface to volume ratio. Even so, OD sensors are rarely used for mammalian cell cultures, more commonly utilized in bacteria or yeast cultures. The larger size and scattering cross section of the mammalian cells for visible wavelengths limits the range of measurement to low cell density measurements ($< 8 \times 10^6$ cells/mL). In order to circumvent this issue, the pathlength of the OD sensor in the RECA Micro-bioreactor is reduced to increase the range to $> 20 \times 10^6$ cells/mL and is linear for 2 orders of magnitude of absorbance. Since the maximum cell density of CHO cell cultures is typically less than 30×10^6 cells/mL, the OD sensor in the RECA Micro-bioreactor is able to cover most of the dynamic range needed for the CHO cell culture. On the other hand, the high surface to volume ratio of the micro-bioreactor brings the issue of evaporation into the spotlight, typically a minor issue in large bioreactors. An evaporation control strategy is very important for the RECA Micro-bioreactor because CHO cells are very sensitive to osmolarity changes. The evaporation rate is measured to be $4.7 \pm 0.2 \mu\text{L}/\text{hr}$, expected to decrease the volume by 75% at the end

of a 14 day culture. An open loop evaporation compensation strategy by periodic injections of sterile water has been designed in the RECA Micro-bioreactor and will be validated in a future experiment by the author of this thesis.

After the completion of the last two validation steps: (1) pH and (2) evaporation control, the RECA Micro-bioreactor will be biologically validated by incubating r-CHO cells from Sanofi into the growth chamber and running a 14 day culture experiment. A parallel shake flask culture for the same r-CHO cells will be performed in the CO₂ incubator as a baseline comparison to the performance of the RECA Micro-bioreactor. Samples will be removed periodically from both the RECA Micro-bioreactor to measure CHO cell densities so that a comparison between the growth rate can be made. At the end of the experiments, the supernatant from both cultures will be frozen at -80°C and then shipped to Sanofi, Germany to compare the end point product titers. This is a future experiment that will be performed by the author of this thesis.

The final part of the thesis is to develop a new viability sensor for the micro-bioreactor, that combined with the OD sensor, confers a new functionality to the RECA Micro-bioreactor. Dielectric spectroscopy(DS) is the recommended method for viability sensing because it is label-free and scalable to small dimensions. In this thesis, two types of miniaturized dielectric spectroscopy electrodes, large(Large IDES) and small(Small IDES) gold interdigitated electrodes are validated against a shake flask CHO culture without any modifications to the sample to test out the performance of the electrodes. Two different data analysis method are employed, the subtraction method and the CPE correction method to remove the parasitic effects of electrode polarization. From a comparison of the results, the CPE correction proves to be a better correction method for this application because the correction can be performed from only the measurement spectra without the need of other external calibration spectra. The final results of the Small IDES compares quantitatively with literature values of dielectric spectroscopy experiments perform on CHO cells using large commercial DS probes. Fabrication of platinum electrodes on polycarbonate sheets has been developed in this thesis with the intention of eventually integrating

the electrodes into the RECA Micro-bioreactor. In the future, it would be desirable to integrate the newly designed and biologically validated DS electrodes in the RECA Micro-bioreactor. This will be a future work which at present is unscheduled and will be performed by the author of this thesis if time, money and opportunity present itself.

Appendix A

Shear FDTD Matlab Code

```
% Clear everything
clear all;
close all;
clc;

% Constants
eta_w = 0.6917*10^-3; % at 37C
R = 8.314;
Patm = 101325;

% Conversions
psi2pa = 6894.75729;
inch2m = 25.4*1e-3;
C2K = 273.15;
mL2m3 = 1e-6;

% Inputs
Rair = 1.25e10;
```

```

% Parameters
Phi = 3*psi2pa + Patm;
Plo = 0*psi2pa + Patm;
z = 0.085*inch2m;      % Mixer Chamber
a = 0.338*inch2m;      % Mixer Chamber
h = 70e-6;              % PDMS Membrane Thickness
E = 1.84e6;
v = 0.5;
T = 37 + C2K;
hw = 0.085*inch2m;      % Water Channels
Lw = 0.09375*inch2m;    % Water Channels
ww = 0.0625*inch2m;    % Water Channels
Vcap = 7.5*mL2m3;       % Max is 17.5mL, assume 10mL water
rmax = 0.2667*inch2m;   % Bottom Radius of the chamber

% Calculated Parameters
D = E*h^3/(12*(1-v^2));
Rw = 12*eta_w*Lw/(ww*hw^3);
Rw = Rw/3;               % 3 channels
Po = 64*D*z/a^4;
Vss = pi*a^2*z;
Pmem_max = Po/(1-(rmax/a)^2);
Vmax = 2*Vss;
Vmin = 0;

% FDTD Specificitions
N = 1e7;                 % Number of Time Points
tcy = 7;
tmax = 3*tcy;             % Maximum time (seconds)
dt = tmax/N;              % Time Step

```

```

% Data storage
t = 0:dt:tmax;
P = zeros(2,N+1);
V = zeros(2,N+1);
n = zeros(2,N+1);
Pmem = zeros(2,N+1);
tau = zeros(1,N+1);

% Initial Values
P(1,1) = Plo;
P(2,1) = Phi;
V(1,1) = 0;
V(2,1) = 2*Vss;
n(1,1) = P(1,1).*(V(1,1)+Vcap)/(R*T);
n(2,1) = P(2,1).*(V(2,1)+Vcap)/(R*T);
tau(1) = 0;

for ii = 1:2
    if P(ii,1)<Po
        Pmem(ii,1) = 3*Po*(V(ii,1)-Vss)/Vss;
    else
        Pmem(ii,1) = (4/9)*Po*Vss^2/((2*Vss-V(ii,1)).^2);
    end
    if Pmem(ii,1)<-Pmem_max
        Pmem(ii,1)=-Pmem_max;
    end
    if Pmem(ii,1)>Pmem_max
        Pmem(ii,1)=Pmem_max;
    end
end

```

```

    end

%      Pmem(ii,1)=0;

end

% FDTD Loop
for jj=2:(N+1)

    if mod(floor(jj*dt/tcy),2)==0
        Pin=Phi;
        Pout=Plo;
    else
        Pin=Plo;
        Pout=Phi;
    end

    n(1,jj)=n(1,jj-1)+dt*((Pin-P(1,jj-1)).*P(1,jj-1)/(Rair*R*T));
    n(2,jj)=n(2,jj-1)+dt*((Pout-P(2,jj-1)).*P(2,jj-1)/(Rair*R*T));
    V(1,jj)=V(1,jj-1)+dt*(P(1,jj-1)-Pmem(1,jj-1)-P(2,jj-1)+...
        Pmem(2,jj-1))/Rw;
    V(2,jj)=V(2,jj-1)-dt*(P(1,jj-1)-Pmem(1,jj-1)-P(2,jj-1)+...
        Pmem(2,jj-1))/Rw;

% Update Parameters
P(1,jj)=n(1,jj)*R*T./(V(1,jj)+Vcap);
P(2,jj)=n(2,jj)*R*T./(V(2,jj)+Vcap);

for ii = 1:2

    if P(ii,jj)<Po
        Pmem(ii,jj) = 3*Po*(V(ii,jj)-Vss)/Vss;
    else
        Pmem(ii,jj) = (4/9)*Po*Vss^2/((2*Vss-V(ii,jj)).^2);
    end

    if Pmem(ii,jj)<-Pmem_max

```

```

Pmem(ii,jj)=-Pmem_max;
end

if Pmem(ii,jj)>Pmem_max
    Pmem(ii,jj)=Pmem_max;
end

if V(ii,jj)>Vmax
    V(ii,jj)=Vmax;
end

if V(ii,jj)<Vmin
    V(ii,jj)=Vmin;
end

end

% Shear Calculation
tau(jj)=6*eta_w/(ww*hw^2)*(V(1,jj)-V(1,jj-1))/dt;
end

% Graph Properties
lw = 2;           % Linewidth

% Plot Shear as a function of Time
figure(1);
set(1,'Position',[689 674 560 420]);
plot(t(1:N),tau(1:N),'-','LineWidth',lw);
xlabel('Time, t(s)', 'FontSize',14);
ylabel('Shear, \tau (Pa)', 'FontSize',14);
grid on;
axis([0 tmax -0.2 0.2]);

```

```

% Plot Pressure 1 and Preesure 2 as a function of Time
figure(2);
set(2,'Position',[1298 677 560 420]);
plot(t(1:N),(P(1,1:N)-Patm)./psi2pa,'-',t(1:N),(P(2,1:N)-Patm)./psi2pa,'-', 'LineWidth'
 xlabel('Time, t(s)', 'FontSize',14);
 ylabel('Pressure, P (psi)', 'FontSize',14);
grid on;
axis([0 tmax 0 3]);

% Plot Volume 1 and Volume 2 as a function of Time
figure(3);
set(3,'Position',[85 676 560 420]);
plot(t(1:N),V(1,1:N)/Vss,'-',t(1:N),V(2,1:N)/Vss,'-', 'LineWidth',lw);
 xlabel('Time, t(s)', 'FontSize',14);
 ylabel('Volume, V/Vss', 'FontSize',14);
axis([0 tmax -0.1 2.1]);
grid on;

```

Appendix B

The Debye Equations

The Debye equations were originally derived for polar molecules, but their general form can be used for any substance whose response to a constant external field exponentially approach equilibrium with a single relaxation time.[21] Conversely, if the external field is applied and then removed suddenly, the system's response will slowly decay to zero with the same relaxation time. Assume the decay function to be $\lambda(t)$ and τ is the relaxation time.

$$\lambda(t) \propto e^{-t/\tau} \quad (\text{B.1})$$

From electric response of linear materials, the electric displacement, D , is related to the electric field, E , by a linear dielectric constant, ϵ . If we examine the static and high frequency limit, we will find the following two relations where ϵ_s refers to the static dielectric constant and ϵ_∞ refers to the optical dielectric constant of the substance.

Static Limit:

$$\lim_{\omega \rightarrow 0} D = \epsilon_s \epsilon_0 E \quad (\text{B.2})$$

High Frequency Limit:

$$\lim_{\omega \rightarrow \infty} D = \epsilon_\infty \epsilon_0 E \quad (\text{B.3})$$

The optical dielectric constant, ϵ_∞ , is the instantaneous response of the substance

to the applied field, and the static dielectric constant, ϵ_s , is a sum of both the instantaneous and time dependent response of the substance to the applied field when a constant field is applied. Assume now that a time dependent field, $E(t)$, is applied, the time dependent electric displacement, $D(t)$, will be related to the electric field by the following equation. Note that the response is linear so the principle of superposition can be applied.

$$D(t) = \epsilon_\infty \epsilon_o E(t) + \epsilon_o \int_{-\infty}^t E(t') \lambda(t - t') dt' \quad (\text{B.4})$$

Converting the integral equation B.4 into a differential equation and making use of the relation:

$$\frac{d\lambda(t)}{dt} = -\frac{1}{\tau} \lambda(t) \quad (\text{B.5})$$

we arrive at the following differential equation after multiplication with τ .

$$\tau \frac{dD(t)}{dt} = \epsilon_\infty \epsilon_o \tau \frac{dE(t)}{dt} + \epsilon_o \tau \lambda(0) E(t) - \epsilon_o \int_{-\infty}^t E(t') \lambda(t - t') dt' \quad (\text{B.6})$$

If equation B.4 and B.6 are summed together, a simple differential equation results.

$$\tau \frac{d}{dt} (D - \epsilon_\infty \epsilon_o E) + (D - \epsilon_\infty \epsilon_o E) = \epsilon_o \tau \lambda(0) E \quad (\text{B.7})$$

To find the constant $\lambda(0)$, we examine the static case, where D and E are related by equation B.2 and the following time derivative goes to zero.

$$\frac{d}{dt} (D - \epsilon_\infty \epsilon_o E) = 0 \quad (\text{B.8})$$

We will obtain the following result for $\lambda(0)$ from applying the static limit to equation B.7.

$$\lambda(0) = \frac{\epsilon_s - \epsilon_\infty}{\tau} \quad (\text{B.9})$$

Inserting this result back into equations B.7 and B.1, we get a differential equation

relating $D(t)$ to $E(t)$ and the full form of the decay function.

$$\tau \frac{d}{dt}(D - \epsilon_\infty \epsilon_o E) + (D - \epsilon_\infty \epsilon_o E) = (\epsilon_s - \epsilon_\infty) \epsilon_o E \quad (\text{B.10})$$

$$\lambda(t) = \frac{\epsilon_s - \epsilon_\infty}{\tau} e^{-t/\tau} \quad (\text{B.11})$$

For the case of a sinusoidally varying applied electric field, $E(t) \propto e^{-i\omega t}$, we will obtain the frequency dependent complex dielectric constant, $\epsilon^*(\omega)$, of the substance, where we have assumed $D = \epsilon^*(\omega)E$. Since now the time derivatives can be summarized as: $d/dt \rightarrow -i\omega$, applying this to the differential equation B.10 we get the complex dielectric constant, $\epsilon^*(\omega)$.

$$\epsilon^*(\omega) = \epsilon_\infty + \frac{\epsilon_s - \epsilon_\infty}{1 - i\omega\tau} \quad (\text{B.12})$$

Separating the real and imaginary parts of the complex dielectric constant, $\epsilon^*(\omega)$, we get the Debye equations.

$$\epsilon_R(\omega) = \epsilon_\infty + \frac{\epsilon_s - \epsilon_\infty}{1 + \omega^2\tau^2} \quad (\text{B.13})$$

$$\epsilon_I(\omega) = \frac{(\epsilon_s - \epsilon_\infty)\omega\tau}{1 + \omega^2\tau^2} \quad (\text{B.14})$$

It is useful to examine the results in the engineering formulation when reading engineering publications where most results of dielectric spectroscopy are published. Converting to engineering formulations, where the external electric field is defined as $E(t) \propto e^{+j\omega t}$ and the complex dielectric constant is defined as $\epsilon^*(\omega) = \epsilon' - j\epsilon''$, we get the following equation for the complex dielectric constant.

$$\epsilon^*(\omega) = \epsilon_\infty + \frac{\epsilon_s - \epsilon_\infty}{1 + j\omega\tau} \quad (\text{B.15})$$

The Debye equations remain the same in the engineering formulation as the physics formulation because of the switch in sign for the definition of the imaginary part of

$$(B.17) \quad \frac{1 + \omega_{2T}^2}{\epsilon_s - \epsilon_\infty(\omega_T)} = (\omega)_n e$$

$$(B.16) \quad \frac{1 + \omega_{2T}^2}{\epsilon_s - \epsilon_\infty} + \infty e = (\omega)_r e$$

$$\cdot (\omega)_* e$$

Appendix C

CHO Shake Flask Culture Protocols

C.1 Seed Train Protocol for Invitrogen CHO-S Free-style Cells

Preparation of Laminar Flow Hood

1. After starting the LFH wait for some time (approx. 20 minutes) to stabilize the flow (common practice for our LFH). Disinfect the Laminar Flow Hood
2. Disinfect gloves. Make sure gloves go over the lab coat sleeves. Purchase Long Sleeve Gloves.
3. Spray anything that goes in
4. When spraying shake flasks, make sure to cover vent top with gloved hands first before spraying
5. Spray the laminar flow hood after using and clean it

Thawing of Cells

Day 1

1. Fill Mr Frosty with IPA to the correct level without the rack. Replace the rack and then store Mr. Frosty in -80°C fridge overnight (approx. 24 h before thawing, minimum 2h before thawing).
2. Make 50mL of fresh medium:
 - (a) CD CHO Medium (1X) – 47.5mL (Invitrogen)
 - (b) GlutaMAX – 2mL
 - (c) HT Supplement – 0.5mL
3. Transfer 50mL of medium into 125mL (max working volume = 2/5 of flask volume) vented flat-bottom shake flasks and store in the incubator (our incubator parameters: 37°C, 5% CO₂-concentration, 80% humidity from water pan,125rpm) overnight (for sterile test and equilibrating)

Day 2

1. Prepare a water bath at 37°C. Place a timer next to the water bath.
2. Prepare Laminar Flow Hood for use and place a clean beaker inside for removal of excess medium.
3. Bring Mr Frosty to the liquid nitrogen tank and remove a cryovial from the tank and place it in Mr Frosty for transport
4. Place cryovial in float and soak it in the water bath for 3 mins
5. Remove 1mL (removed volume depends on the volume of cryoconserved cell suspension into the vial and the initial cell density) of medium from the new shake flasks inside the laminar flow hood.

6. When the alarm rings, check if there are any ice crystals inside the vials, if there is, put the vial back in the water bath for another 1 min (Max)
7. Spray the vial with 70% ethanol before placing it in the Hood
8. Slowly pipette up 1mL using a 1mL pipette only in a single direction. The cells are very frail so pipette down slowly into the shake flasks
9. Put the shake flask in incubator for approx. 2 mins to mix it further
10. Take out 500 μ L sample for cell counting.

Day 3

1. Take out 500 μ L sample for cell counting.

Day 4

1. Put a new shake flask with fresh medium in incubator overnight (follow Step 2-3 on Day 2)
2. Take out 500 μ L sample for cell counting.

Day 5

1. Take out 500 μ L sample for cell counting.
2. Do not subculture if cell density is below 8×10^5 cells/mL. Definitely subculture if by the next doubling the cell density will exceed 3×10^6 cells/mL.
3. Subculture Protocol:
 - (a) After counting cells, calculate the volume, V_T , needed for the passage so that the incubated cell density is 2×10^5 cells/mL
 - (b) Placed a clean empty beaker in the LF for transfer of excess medium.
 - (c) Transfer V_T of medium from the new shake flask out and then transfer V_T of cell culture from the old shake flask.

- (d) After transfer, (make sure, the cell suspension is homogeneous - shake manually or for a short time in incubator) remove 500 μ L from the new shake flask for cell counting.
- (e) Return shake flasks to the incubator

Freezing of Cells

Day 1

1. Fill Mr Frosty with IPA to the correct level without the rack. Replace the rack and then store Mr. Frosty in 4°C fridge overnight

Day 2

1. Remove 500 μ L for cell counting
2. Subculture and freeze cryovials if cell density is 1×10^6 cells/mL
3. Prepare water bath at 37°C
4. Defrost DMSO in a rack in the water bath
5. For a final volume of 10mL, prepare the following stock of the cell freezing medium:
 - (a) 4.63mL CD CHO (= 46.25% of total volume)
 - (b) 0.75mL DMSO (= 7.5% of total volume)
6. Return DMSO to the 4°C fridge.
7. After counting cells, calculate volume, V_F , of suspension containing 1×10^7 cells.
8. Assume that we are freezing 8 vials, remove $5 \times V_F$ volume of cell suspension from the flask and place inside a centrifuge tube. Repeat this for the second centrifuge tube.

9. Centrifuge the tubes at the following time and centrifugal force:
 - (a) 210 g
 - (b) 5 minutes
 - (c) Radius = 16cm (for our centrifuge)
 - (d) 6K RPM (for our centrifuge)
10. After centrifuging, remove excess supernatant till the remaining medium volume is 2.31mL for each tube. (Remove $5 \times V_F - 2.31\text{mL}$)
11. Resuspend the cells gently using the pipette. Make sure to pipette the pellet to break it into small pieces.
12. Transfer 2.69mL of the stock solution of prepared freezing medium into the tube and mix it gently
13. Label the 8 cryo vials with the following:
 - (a) Cell Line
 - (b) Date
 - (c) Vial #
 - (d) Initials
14. Use a 1mL pipette to transfer the cells from each centrifuge tube to the 8 cryo vials.
15. Transfer all 8 cryovials into Mr. Frosty
16. Store Mr Frosty in a -80°C fridge for 2 hours
17. After 2 hours, Transfer the flasks to the gas phase of the Liquid Nitrogen tank (Maximum 2 days waiting time)

Regular Passage Schedule

Monday

1. Make 50mL of fresh medium:
 - (a) CD CHO Medium (1X) – 47.5mL (Invitrogen)
 - (b) GlutaMAX – 2mL
 - (c) HT Supplement – 0.5mL
2. Transfer 50mL of medium into 125mL Shake Flasks (max working volume = 2/5 of flask volume) vented flat-bottom shake flasks and store in the incubator (our incubator parameters: 37°C, 5% CO₂-concentration, 80% humidity from water pan, 125rpm) overnight (for sterile test and equilibrating)
3. Change the Milli-Q water in the water pan.

Tuesday

1. Remove 500μL from the old shake flasks for cell counting and return shake flask to incubator immediately
2. After counting cells, calculate the volume, V_T, needed for the passage so that the incubated cell density is 2×10^5 cells/mL.
3. Transfer V_T of medium from the new shake flask out into a sterile centrifuge tube and then transfer in V_T of cell culture from the old shake flask.
4. After transfer, remove 500μL from the new shake flask for cell counting. Return both shake flasks to the incubator.

Thursday

1. Make 50mL of fresh medium:
 - (a) CD CHO Medium (1X) – 47.5mL (Invitrogen)

- (b) GlutaMAX – 2mL
 - (c) HT Supplement – 0.5mL
2. Transfer 50mL of medium into 125mL Shake Flasks and store in the incubator overnight.

Friday

1. Remove $500\mu\text{L}$ from the old shake flasks for cell counting and return shake flask to incubator immediately
2. After counting cells, calculate the volume, V_T , needed for the passage so that the incubated cell density is 2×10^5 cells/mL.
3. Transfer V_T of medium from the new shake flask out into a sterile centrifuge tube and then transfer in V_T of cell culture from the old shake flask.
4. After transfer, remove $500\mu\text{L}$ from the new shake flask for cell counting. Return both shake flasks to the incubator.

C.2 Growth Profiles of CHO Shake Flask Cultures

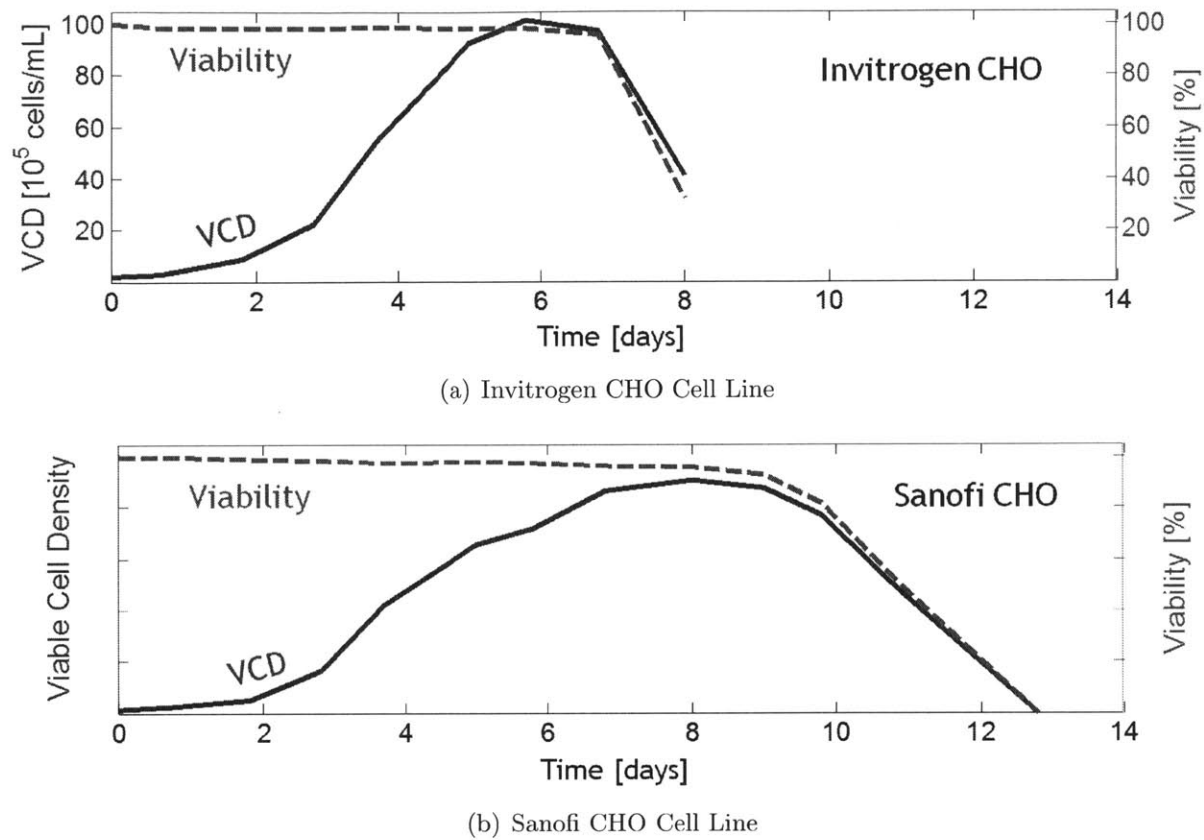


Figure C-1: Growth curve for the (a) Invitrogen and (b) Sanofi CHO cell lines. The Sanofi cell line has a longer stationary phase than the Invitrogen cell line because it has been optimized for production.

Bibliography

- [1] Christoph Alexander and Johannes Von Bültzingslöwen. *Development of Optical Sensors (" Optodes ") for Carbon Dioxide and their Application to Modified Atmosphere Packaging (MAP)*. PhD thesis, Regensburgh University, 2003.
- [2] Rachel Bareither and David Pollard. A review of advanced small-scale parallel bioreactor technology for accelerated process development: current state and future need. *Biotechnology progress*, 27(1):2–14, 2011.
- [3] L M Barnes, C M Bentley, and a J Dickson. Characterization of the stability of recombinant protein production in the GS-NS0 expression system. *Biotechnology and bioengineering*, 73(4):261–70, May 2001.
- [4] P Ben Ishai, Z Sobol, J D Nickels, a L Agapov, and a P Sokolov. An assessment of comparative methods for approaching electrode polarization in dielectric permittivity measurements. *The Review of scientific instruments*, 83(8):083118, August 2012.
- [5] J. C. Bernengo and M. Hanss. Four-electrode, very-low-frequency impedance comparator for ionic solutions. *Review of Scientific Instruments*, 47(4):505, 1976.
- [6] F Bordi. Reduction of the contribution of electrode polarization effects in the radiowave dielectric measurements of highly conductive biological cell suspensions. *Bioelectrochemistry*, 54(1):53–61, August 2001.
- [7] M C Borys, D I Linzer, and E T Papoutsakis. Ammonia affects the glycosylation patterns of recombinant mouse placental lactogen-I by chinese hamster ovary

- cells in a pH-dependent manner. *Biotechnology and bioengineering*, 43(6):505–14, March 1994.
- [8] Ole Henrik Brekke and Inger Sandlie. Therapeutic antibodies for human diseases at the dawn of the twenty-first century. *Nature reviews. Drug discovery*, 2(1):52–62, January 2003.
- [9] a Buchenauer, M C Hofmann, M Funke, J Büchs, W Mokwa, and U Schnakenberg. Micro-bioreactors for fed-batch fermentations with integrated online monitoring and microfluidic devices. *Biosensors & bioelectronics*, 24(5):1411–6, January 2009.
- [10] Conor S. Burke, Adam Markey, Robert I. Nooney, Patrick Byrne, and Colette McDonagh. Development of an optical sensor probe for the detection of dissolved carbon dioxide. *Sensors and Actuators B: Chemical*, 119(1):288–294, November 2006.
- [11] Aaron Chen, Rajesh Chitta, David Chang, and Ashraf Amanullah. Twenty-four well plate miniature bioreactor system as a scale-down model for cell culture process development. *Biotechnology and bioengineering*, 102(1):148–60, January 2009.
- [12] Kenneth Cole and Robert Cole. Dispersion and Absorption in Dielectrics : I. Alternating Current Characteristics. *Journal of Chemical Physics*, 9:341–351, 1941.
- [13] Roger Collier. Drug development cost estimates hard to swallow. *CMAJ : Canadian Medical Association journal = journal de l'Association medicale canadienne*, 180(3):279–80, February 2009.
- [14] C L Davey, G H Markx, D B Kell, and United Kingdom. Substitution and spreadsheet methods for analyzing dielectric spectra of biological systems. *European Biophysics Journal*, 18:255–265, 1990.

- [15] Vivian M DeZengotita, Albert E Schmelzer, and William M Miller. Characterization of Hybridoma Cell Responses to Elevated pCO₂ and Osmolality : Intracellular pH , Cell Size , Apoptosis , and Metabolism. *Biotechnology*, 77(4):369–380, 2002.
- [16] Michael Dickson and Jean Paul Gagnon. The Cost of New Drug Discovery and Development. *Discovery Medicin*, 4:172–179, 2009.
- [17] W S Dodds, L F Stutzman, and B J Sollami. Carbon Dioxide Solubility in Water. *Journal of Chemical and Engineering Data*, 1(1):92–95, 1956.
- [18] Everett Douglas. Solubilities of Oxygen , Argon , and Nitrogen in Distilled Water. *The Journal of Physical Chemistry*, 68(1):169–174, 1964.
- [19] William P Eaton, Fernando Bitsie, James H Smith, and David W Plummer. A New Analytical Solution for Diaphragm Deflection and its Application to a Surface-Micromachined Pressure Sensor. In *Technical Proceedings of the 1999 International Conference on Modelling and Simulations of Microsystems*, pages 640–643, 1999.
- [20] Xu Fei. A Solution for Measuring the Dielectric Spectroscopy of Conductive Aqueous. In *IEEE Conference on Electronic & Mechanical Engineering and Information Technology*, pages 4868–4870, Harbin, Heilongjiang, 2011.
- [21] H Frohlich. *Theory of Dielectrics : Dielectric Constant and Dielectric Loss*. Oxford University Press, London, 2nd edition, 1958.
- [22] Ruben Godoy-Silva, Jeffrey J Chalmers, Susan a Casnocha, Laura a Bass, and Ningning Ma. Physiological responses of CHO cells to repetitive hydrodynamic stress. *Biotechnology and bioengineering*, 103(6):1103–17, August 2009.
- [23] R Gomez, R Bashir, A Sarikaya, and M.R. Ladisch. Microfluidic Biochip for Impedance Spectroscopy of Biological Species. *Biomedical microdevices*, 3(3):201–209, 2001.

- [24] Atul Gupta and Govind Rao. A study of oxygen transfer in shake flasks using a non-invasive oxygen sensor. *Biotechnology and bioengineering*, 84(3):351–8, November 2003.
- [25] Michael A Hanson, Xudong Ge, Yordan Kostov, Kurt A Brorson, Antonio R Moreira, and Govind Rao. Comparisons of Optical pH and Dissolved Oxygen Sensors With Traditional Electrochemical Probes During Mammalian Cell Culture. *Biotechnology*, 97(4):833–841, 2007.
- [26] Christine M Harris, Robert W Todd, Stephen J Bungard, Robert W Lovitt, Gareth Morris, and Douglas B Keli. Dielectric permittivity of microbial suspensions at radio frequencies : a novel method for the real-time estimation of microbial biomass. *Enzyme and Microbial Technology*, 9:181–186, 1987.
- [27] R. Hayakawa, H. Kanda, M. Sakamoto, and Y. Wada. New apparatus for measuring the complex dielectric constant of a highly conductive material. *Japanese Journal of Applied Physics*, 14(12):2039–2052, 1975.
- [28] Guang S. He, Hai-Yan Qin, and Qingdong Zheng. Rayleigh, Mie, and Tyndall scatterings of polystyrene microspheres in water: Wavelength, size, and angle dependences. *Journal of Applied Physics*, 105(2):023110, 2009.
- [29] C Huber, I Klimant, C Krause, T Werner, T Mayr, and O S Wolfbeis. Optical sensor for seawater salinity. *Fresenius' journal of analytical chemistry*, 368(2-3):196–202, 2000.
- [30] Ciprian Iliescu, Daniel P. Poenaru, Mihaela Carp, and Felicia C. Loe. A microfluidic device for impedance spectroscopy analysis of biological samples. *Sensors and Actuators B: Chemical*, 123(1):168–176, April 2007.
- [31] Kevin Isett, Hugh George, Wayne Herber, and Ashraf Amanullah. Twenty-Four-Well Plate Miniature Bioreactor High-Throughput System : Assessment for Microbial Cultivations. *Biotechnology*, 98(5):1017–1028, 2007.

- [32] Andrew Jack. Balancing Big Pharma's books. *BMJ*, 336(7641):418–419, February 2008.
- [33] Julian T Keane, David Ryan, and Peter P Gray. Effect of shear stress on expression of a recombinant protein by Chinese hamster ovary cells. *Biotechnology and bioengineering*, 81(2):211–20, January 2003.
- [34] Haley R Kermis, Yordan Kostov, Peter Harms, and Govind Rao. Dual excitation ratiometric fluorescent pH sensor for noninvasive bioprocess monitoring: development and application. *Biotechnology progress*, 18(5):1047–53, 2002.
- [35] Bhargavi Kondragunta, Jessica L Drew, Kurt a Brorson, Antonio R Moreira, and Govind Rao. Advances in clone selection using high-throughput bioreactors. *Biotechnology progress*, 26(4):1095–103, 2010.
- [36] J. R. Lakowicz. *Principles of Fluorescence Spectroscopy*. Plenum Press, New York/London, 2nd editio edition, 1999.
- [37] Harry Lee. *Integrated microbioreactor arrays for high-throughput experimentation*. PhD thesis, Massachusetts Institute of Technology, 2006.
- [38] Kevin S Lee, Paolo Boccazzi, Anthony J Sinskey, and Rajeev J Ram. Microfluidic chemostat and turbidostat with flow rate, oxygen, and temperature control for dynamic continuous culture. *Lab on a chip*, 11(10):1730–9, May 2011.
- [39] Kevin S Lee and Rajeev J Ram. Plastic PDMS bonding for high pressure hydrolytically stable active microfluidics. *Lab on a chip*, 9:1618–1624, 2009.
- [40] Kevin Shao-kwan Lee. *Microscale Controlled Continuous Cell Culture*. PhD thesis, Massachusetts Institute of Technology, 2011.
- [41] Rachel Legmann, H Brett Schreyer, Rodney G Combs, Ellen L McCormick, a Peter Russo, and Seth T Rodgers. A predictive high-throughput scale-down model of monoclonal antibody production in CHO cells. *Biotechnology and bioengineering*, 104(6):1107–20, December 2009.

- [42] By Feng Li, J O E X Zhou, Xiaoming Yang, and Brian Lee. Current Therapeutic Antibody Production and Process Optimization. *Bioprocessing Journal*, (October):1–8, 2005.
- [43] Andy A Lin, Roy Kimura, and William M Miller. Production of tPA in Recombinant CHO Cells Under Oxygen-Limited Conditions. *Biotechnology and bioengineering*, 42:339–350, 1993.
- [44] Vaclav Linek, P Benes, and Vaclav Vacek. Measurement of Aeration Capacity of Fermenters. *Chemical Engineering Technology*, 12:213–217, 1989.
- [45] Xin Lu, Ian Manners, and Mitchell a. Winnik. Polymer/Silica Composite Films as Luminescent Oxygen Sensors. *Macromolecules*, 34(6):1917–1927, March 2001.
- [46] I H Madshus. Regulation of intracellular pH in eukaryotic cells. *The Biochemical journal*, 250(1):1–8, February 1988.
- [47] D Malleo, J T Nevill, a van Ooyen, U Schnakenberg, L P Lee, and H Morgan. Note: Characterization of electrode materials for dielectric spectroscopy. *The Review of scientific instruments*, 81(1):016104, January 2010.
- [48] Maria D. Marazuela, Maria C. Moreno-Bondi, and Guillermo Orellana. Luminescence Lifetime Quenching of a Ruthenium(II) Polypyridyl Dye for Optical Sensing of Carbon Dioxide. *Applied Spectroscopy*, 52(10):1314–1320, October 1998.
- [49] James E. (University of Cincinnati) Mark, editor. *POLYMER DATA HANDBOOK*. Oxford University Press, New York, 2 edition, 1999.
- [50] A F Mazarei and O C Sandall. Diffusion Coefficients for Helium, Hydrogen and Carbon Dioxide in Water at 25C. *AIChE Journal*, 26(1):154–157, 2004.
- [51] Brian. a. Mazzeo and Andrew J. Flewitt. Two- and four-electrode, wide-bandwidth, dielectric spectrometer for conductive liquids: Theory, limitations, and experiment. *Journal of Applied Physics*, 102(10):104106, 2007.

- [52] Barbara Menz, Robert Knerr, Achim G  pferich, and Claudia Steinem. Impedance and QCM analysis of the protein resistance of self-assembled PEGylated alkanethiol layers on gold. *Biomaterials*, 26(20):4237–43, July 2005.
- [53] Andrew Mills, Qing Chang, and Milton Keynes. Fluorescence Plastic Thin-film Sensor for Carbon Dioxide. *Analyst*, 118(July):839–843, 1993.
- [54] Beat Muller and Peter C Hauser. Fluorescence Optical Sensor for Low Concentrations of Dissolved Carbon Dioxide. *Analyst*, 121(March):339–343, 1996.
- [55] D Myers. Dielectric spectroscopy of colloidal suspensions I. The dielectric spectrometer. *Journal of Colloid and Interface Science*, 131(2):448–460, September 1989.
- [56] L Nyikos and T Pajkossy. Fractal dimension and fractional power frequency-dependent impedance of blocking electrodes. *Electrochimica Acta*, 30(11):1533–1540, November 1985.
- [57] W Olthuis, W Streekstra, and P Bergveld. Theoretical and experimental determination of cell constants of planar-interdigitated electrolyte conductivity sensors. *Sensors and Actuators B: Chemical*, 24-25(1-3):252–256, March 1995.
- [58] Sadettin S. Ozturk and Bernhard Palsson. Growth, Metabolic, and Antibody Production Kinetics of Hybridoma Cell Culture: 2. Effects of Serum Concentration, Dissolved Oxygen Concentration, and Medium pH in a Batch Reactor. *Biotechnology Progress*, 7(6):481–494, 1991.
- [59] Jin Hwan Park, Sang Yup Lee, Tae Yong Kim, and Hyun Uk Kim. Application of systems biology for bioprocess development. *Trends in biotechnology*, 26(8):404–12, August 2008.
- [60] H. Pauly and H.P. Schwan. Uber die Impedanz einer Suspension von kugelformigen Teilchen mit einer Schale. *Z. Naturforsch*, 14b:125–131, 1959.

- [61] Alex K Pavlou. Marketspace: The immunotherapies markets, 20032008. *Journal of Commercial Biotechnology*, 10(3):273–278, March 2004.
- [62] Janice Reichert and Alex Pavlou. Monoclonal antibodies market. *Nature reviews. Drug discovery*, 3(5):383–4, May 2004.
- [63] Janice M Reichert, Clark J Rosensweig, Laura B Faden, and Matthew C Dewitz. Monoclonal antibody successes in the clinic. *Nature biotechnology*, 23(9):1073–8, September 2005.
- [64] Janice M Reichert and Viiia E Valge-archer. Development trends for monoclonal antibody cancer therapeutics. *Nature Reviews Drug Discovery*, 6(May):349–356, 2007.
- [65] Hugo Sanabria and John Miller. Relaxation processes due to the electrode-electrolyte interface in ionic solutions. *Physical Review E*, 74(5):051505, November 2006.
- [66] Daniel Schäpper, Muhd Nazrul, Hisham Zainal, Nicolas Szita, Anna Eliasson Lantz, and Krist V Gernaey. Application of microbioreactors in fermentation process development : a review. *Analytical and Bioanalytical Chemistry*, pages 679–695, 2009.
- [67] H. P. Schwan. Alternating current electrode polarization. *Biophysik*, 3(2):181–201, June 1966.
- [68] Herman P. Schwan. Four-Electrode Null Techniques for Impedance Measurement with High Resolution. *Review of Scientific Instruments*, 39(4):481, 1968.
- [69] J Antonio Serrato, Laura a Palomares, Angélica Meneses-Acosta, and Octavio T Ramírez. Heterogeneous conditions in dissolved oxygen affect N-glycosylation but not productivity of a monoclonal antibody in hybridoma cultures. *Biotechnology and bioengineering*, 88(2):176–88, October 2004.

- [70] C E St-Denis and C J D Fell. Diffusivity of Oxygen in Water. *The Canadian Journal of Chemical Engineering*, 49(6):885, 1971.
- [71] Bernard Thorens and Pierre Vassalli. Chloroquine and ammonium chloride prevent terminal glycosylation of immunoglobulins in plasma cells without affecting secretion. *Nature*, 321(5):618–620, 1986.
- [72] Mónica Tirado and Constantino Grosse. Conductivity dependence of the polarization impedance spectra of platinum black electrodes in contact with aqueous NaCl electrolyte solutions. *Colloids and Surfaces A: Physicochemical and Engineering Aspects*, 222(1-3):293–299, July 2003.
- [73] Kimberly F Webb and Amyn S Teja. Solubility and diffusion of carbon dioxide in polymers. *Fluid Phase Equilibria*, 158-160:1029–1034, June 1999.
- [74] D Weuster-Botz, J Altenbach-Rehm, and M Arnold. Parallel substrate feeding and pH-control in shaking-flasks. *Biochemical engineering journal*, 7(2):163–170, March 2001.
- [75] Christoph Wittmann, Hyung Min Kim, Gernot John, and Elmar Heinzle. Characterization and application of an optical sensor for quantification of dissolved O₂ in shake-flasks. *Biotechnology letters*, 25(5):377–80, March 2003.
- [76] P Wu, S S Ozturk, J D Blackie, J C Thrift, C Figueroa, and D Naveh. Evaluation and applications of optical cell density probes in mammalian cell bioreactors. *Biotechnology and bioengineering*, 45(6):495–502, March 1995.
- [77] Gilwon Yoon. Dielectric properties of glucose in bulk aqueous solutions: Influence of electrode polarization and modeling. *Biosensors & bioelectronics*, 26(5):2347–53, January 2011.
- [78] Zhiyu Zhang, Nicolas Szita, Paolo Boccazzì, Anthony J Sinskey, and Klavs F Jensen. A Well-Mixed , Polymer-Based Microbioreactor With Integrated Optical Measurements. *Biotechnology and bioengineering*, 93(2):287–296, 2005.